MASTER THESIS
JOINT NORDIC MASTER IN MARINE ECOSYSTEMS AND CLIMATE

Estimating fin whale distribution from ambient noise spectra using Bayesian inversion

1ST JUNE, 2015

University Supervisor:
Prof. Dr. Corinna Schrum
First External Supervisor:
Dr. Hanne Sagen
Second External Supervisor:
Prof. Dr. Halvor Hobæk

Author:
Sebastian Menze

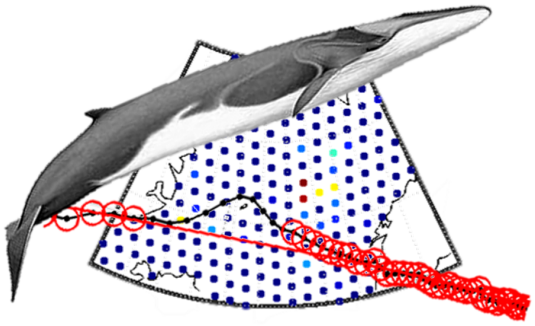

UNIVERSITY OF BERGEN, UNIVERSITY OF ICELAND, UNIVERSITY OF AARHUS,
UNIVERSITY OF THE FAROE ISLANDS

"One man's noise is another man's signal."
Edward W Ng (1990) Lost on Earth: Wealth of Data Found in Space, New York Times

"Essentially, all models are wrong, but some are useful."
Box, G. E. P., and Draper, N. R. (1987) Empirical Model Building and Response Surfaces,John Wiley & Sons, New York, NY.

"Far better an approximate answer to the right question, which is often vague, than an exact answer to the wrong question, which can always be made precise."
John Tukey (1962) The future of data analysis. Annals of Mathematical Statistics 33 (1)

THIS THESIS WAS WRITTEN IN COOPERATION WITH THE NANSEN ENVIRONMENTAL AND REMOTE SENSING CENTER

Abstract:

Passive acoustic monitoring is increasingly used to study the distribution and migration of marine mammals. Marine mammal vocalizations are transient sounds, but the combined sound energy of a population continuously repeating a vocalization, adds up to a quasi-continuous chorus. Marine mammal choruses can be identified as peaks in ocean ambient noise spectra. In the North Atlantic, the fin whale chorus is commonly observed as peak at 20 Hz. This thesis proposes a method to estimate the distribution of vocalizing fin whales based on a set of fin whale chorus recordings. This is an extremely under-determined inverse problem. The method is based on Bayesian inverse theory and uses simulated annealing to estimate the most likely distribution of sound sources (vocalizing whales) on a geodesic grid. This includes calculating a transmission loss matrix connecting all grid nodes and recorders, using an arbitrary sound propagation model. Two models were successfully implemented: geometrical spreading and the ray trace model BELLHOP. The inversion method was tested under different scenarios. The results indicated that an imprecise transmission loss matrix is tolerated by the inversion method. The accuracy of the method depended mainly on the number and distribution of recorders. For the Norwegian sea, simulations showed that fin whale chorus inversion is possible using as few as 12 recorders between Iceland and Svalbard. An inversion based on data from published fin whale chorus observations indicated realistic winter distribution patterns. Existing methods to study marine mammal distribution are often confined to the summer months and a limited area. Future application of the proposed method admits automatic year-round monitoring of marine mammal distribution on a basin-wide scale.

Contents

1. Introduction

Recording and analyzing underwater sound is termed passive acoustic monitoring (PAM) in the scientific literature (Au and Hastings, 2008). The term passive distinguishes the method from active acoustic monitoring, where sound signals are emitted actively (examples are sonars or current measurement devices). Passive acoustic monitoring requires an array of sound receivers (hydrophones) that are either moored to the sea floor, towed behind a vessel or drifting freely. This thesis describes a new approach to analyze underwater sound recordings, based on inverse theory.

Underwater sound recordings contain signals from many different sources, ranging from breaking waves to marine mammals. The recorded sound signals can be divided into transient signals and a continuous acoustic background signal, the ambient noise. In the ocean, most ambient noise stems from motion at the sea surface, such as wave breaking and oscillating bubble clouds (Carey and Evans, 2011). Increasingly though, human generated sound from marine traffic and seismic surveys dominates ambient noise between 25 and 200 Hz (Andrew et al., 2011, Frisk, 2012). Vocalizing marine mammals are also a source of ambient noise. The combined sound of a population repeating the same vocalization many times, adds up to a constant marine mammal chorus, that can be identified as distinct peak in ambient noise spectra. These underwater choruses can be seen as oceanic analogue to the dawn chorus of birds and insects on land. The analysis of marine mammal choruses revealed extensive spatial as well as inter- and intra-annual variation (Burtenshaw et al., 2004, Nieukirk et al., 2012, Menze, 2012).

The majority of PAM studies focus on the analysis of transient sounds from individual animals (Au and Hastings, 2008, Van Parijs et al., 2009, Mellinger et al., 2007). This thesis presents a different approach: Instead of determining the position of individual animals based on their transient vocalizations, the proposed method estimates the distribution of all vocalizing animals based on the chorus they produce. This is a highly underdetermined inverse problem: the number of possible whale locations is much higher than the number of available recorders. In addition, the source levels and call rates vary between animals and seasons. To include these uncertainties into the distribution estimates, a numerical technique based on Bayesian inverse theory will be presented.

The method is developed for the chorus of North Atlantic fin whales (*Balaenoptera physalus*, Figure 1), but can be applied to other marine mammal choruses as well. Fin whales are a highly migratory species, and little is known about their migration patterns and winter distribution (Víkingsson et al., 2013). Marine mammal distribution is traditionally studied visually, using observers on ships and aircrafts (Marques, 2009, Thomas et al., 2006). These surveys require considerable ship-time and personnel and are difficult to perform year-round (especially in darkness or sea ice). The inversion method described in this thesis can estimate the distribution of vocalizing fin whales year-round and on a basin scale. Thereby, the proposed method could close knowledge gaps in fin whale migration other methods cannot answer.

Figure 1: Fin whale surfacing near Svalbard in June 2012

The objectives of this thesis are summarized in the following research questions:

- Can we estimate the distribution of vocalizing animals from a set of chorus (their combined vocalizations) recordings?
- What are the capabilities and limitations of this method?
- How could it be implemented?

2. Marine mammals

The new method can be applied to all marine mammal species that produce a chorus. Thus this section first introduces marine mammal distribution and acoustics in general and then focuses on fin whales. The term marine mammals includes cetaceans (toothed and baleen whales), seals, manatees and even polar bears (Perrin et al., 2009). Of these, only some baleen whale and seal species produce a marine mammal chorus. A chorus is only produced once a vocalization is repeated often enough, by enough animals and at a low enough frequency (due the reduced absorption of low frequency sound waves in seawater). A marine mammal chorus is a quasi-continuous signal, rendering it impossible to distinguish the vocalizations of individual animals. Table 1 summarizes the marine mammal species of which choruses have been observed and lists the respective references.

Table 1: Observed marine mammal choruses

Species	Frequency range	Region	References
Fin whales (*Balaenoptera physalus*)	18 - 30 Hz	North Atlantic	Simon et al. (2010), Nieukirk et al. (2012), Klinck and Nieukirk (2012)
Fin whales (*Balaenoptera physalus*)	18 - 30 Hz and 85 - 105 Hz	Southern Ocean	Širović et al. (2004), Gedamke et al. (2007), Menze (2012), Dziak et al. (2015)
Blue whales (*Balaenoptera musculus*)	15 - 25 Hz	North Pacific	Curtis et al. (1999), Burtenshaw et al. (2004)
Blue whales (*Balaenoptera musculus*)	18 - 30 Hz and 26 - 27 Hz	Southern Ocean	Širović et al. (2004), Gedamke et al. (2007), Gavrilov et al. (2012), Menze (2012), Dziak et al. (2015)
Pygmy blue whales (*Balaenoptera musculus brevicauda*)	65 - 75 Hz	Southern Ocean	Gedamke et al. (2007)
Antarctic minke whales (*Balaenoptera bonaerensis*)	100 - 300 Hz	Southern Ocean	Menze (2012)
Leopard seals (*Hydrurga leptonyx*)	320 - 350 Hz	Southern Ocean	Menze (2012)

In the ocean it is mainly baleen whales that produce a chorus. They are known for their extreme body sizes and belong to the top predators of most marine ecosystems (Perrin et al., 2009). Baleen whales have been exploited extensively in the last centuries, leaving several species close to extinction (Cressey, 2015). To ensure sustainable management of marine mammal populations it is necessary to know each species population structure. Because baleen whales are highly mobile, it has been difficult to distinguish between different stocks (Delarue et al., 2009, Castellote et al., 2004). Knowledge of migration patterns and the variability of baleen whale distribution can improve their management.

2.1. Distribution and migration

Baleen whales (Mysticeti) are known for their large scale migrations, that are commonly described as annual movement between high latitude feeding and low latitude breeding grounds (Perrin et al., 2009). The reasons for these large scale migrations are subject to speculation. Possible reasons range from the physiological effects of water temperature on calves to sea ice avoidance, inherited behavior or the avoidance of predation from killer whales (Corkeron and Connor, 1999)

The exact distribution and migration patterns depend on each species' ecological niche. Baleen whales are most commonly observed in mid and high latitude waters, where they feed on aggregations of zooplankton or small fish. Baleen whale feeding is only efficient when the prey density is high enough (Goldbogen et al., 2011, 2007). In high latitude ecosystems, the spring or summer bloom of phytoplankton is followed by a respective increase in zooplankton biomass (Mann and Lazier, 2013). Utilizing these seasonal peaks in prey availability is likely one of the major drivers of baleen whale migration and distribution. Their physiology allows them store large amount of energy as blubber, which also serves as insulation. This feature allows them to migrate over thousands of kilometers and renders the allocation of dense prey aggregations in their vast habitat a key element of their life history. For several baleen whales species it has been documented, that oceanic fronts or shelf slopes affect their distribution (Mauritzen et al., 2004, Ingram et al., 2007, Joiris et al., 2014). This is likely due to the increased productivity associated with frontal structures or upwelling along shelf or sea ice edges (Falk-Petersen et al., 2015).

Most studies on marine mammal distribution and behavior are based on visual surveys, either from the coast or using shipboard and aerial observers. Distance sampling using line transects provides statistically sound means to determine animal abundance in a predefined area (Marques, 2009). However, these methods have a low temporal resolution since surveys are performed over a period of weeks or months. Due to the amount of ship-time and personnel required to observe the entire North Atlantic, these surveys are usually held every few years and provide little information on the migration patterns and intra-annual variation in marine mammal distribution.

With the rise of satellite technologies, tagging studies are increasingly used to investigate migration routes. A recent study about right whales by Mate et al. (2015) documented the longest migration routes measured for any mammal so far (22511 km from Sakhalin Island to the Mexican coast). Tagging studies have proven useful to determine the behavior and migration patters of individual animals. They provide accurate informa-

tion on an animals movement, but have the disadvantage of high cost, short sampling period (in the order of months) and very limited sample size. To study the migration of an entire population, it seem more feasible to combine visual and acoustic methods. The next section will introduce how passive acoustic monitoring is used to study marine mammals.

2.2. Bioacoustics

Marine mammals utilize sound for foraging, orientation and communication. While toothed whales evolved high frequency vocalizations such as clicks and whistles, most baleen whales emit pulsed sounds between 10 to 1000 Hz (Au and Hastings, 2008). Seals have been observed to emit a wide variety of sounds often described as grunts and moans between roughly 100 and 10000 Hz (Van Opzeeland, 2010). Toothed whales utilize specialized airs sacs and lips to produce clicks and whistles, whereas the sound production mechanisms of baleen whales remains largely unknown (Au and Hastings, 2008).

Due to the low frequency of baleen whale vocalizations, their communication range is very large (hundreds of kilometers) compared to toothed whales. Whether baleen whales utilize these long transmission paths is seldom know. Due to their low frequency, it is unlikely that baleen whale use their vocalizations for echolocation. Humpback whales are known for their extensive acoustic repertoire, that are mainly thought of as male breeding display but may also serve other functions (Herman et al., 2013). Blue whales exhibit a far less diverse repertoire, that consists of breeding and feeding calls (Oleson and Calambokidis, 2007). Blue and fin whales usually emit their calls in pulse trains, repeating a single call type over hours (Sirović et al., 2007). Fin whale vocalizations will be discussed in the following section. Payne and Webb (1971) discuss the possibility that the monotonous calls of blue and fin whales act as long distance ranging signals, to lure possible mates to prey aggregations. Compared to the complex communication or echolocation found in other species, blue and fin whales likely use sound simply to find and attract mating partners in their vast habitat.

Baleen whale vocalizations are commonly recorded using moored or towed hydrophones. Moored autonomous recorders are increasingly used to record the underwater soundscape and marine mammal vocalizations over periods of years (Rettig et al., 2013). After recovering the moorings, the recordings are manually or automatically scanned for vocalizations (Towsey et al., 2013). From the detected vocalizations one can determine when calling animals are present in the detection range of the recorder. However, one cannot determine when the animals are absent, since they could simply not vocalize and still remain in the area.

When the recorder array consists of at least 3 hydrophones, that record the same vocalization simultaneously, the location of the animal can be determined from differences in the arrival time of the vocalization. This method is commonly termed triangulation (Clark, 1995, Au and Hastings, 2008). Other methods of localizing vocalizing whales utilize the effects of multipath propagation (Valtierra et al., 2013, Newhall et al., 2012, McDonald and Fox, 1999). Next to the use of hydrophones, whales have also been tracked using ocean bottom seismometers (Wilcock, 2012). However to determine marine mammal distribution it is necessary to know the approximate position of thousands of animals. To

track that many individuals on an ocean basin scale requires an unrealistically large number of recorders.

To connect the detection of vocalizations with animal density or distribution estimates, other approaches exist. These have to deal with the large uncertainties connected with animal behavior. For example, recording an increasing number of vocalizations does not automatically imply an increased abundance of whales, but could be caused by an increasing call rate or increasing detection probability (Helble et al., 2013b). Some of the most important variables to connect acoustic detection with animal abundance are the source pressure level (SL) of the animals, their call rate (CR) and the probability to detect the calls (Marques et al., 2013). Helble et al. (2013a) showed that ignoring the detection probability in passive acoustic surveys can introduce significant biases. The two most promising methods connecting acoustic detection and animal abundance, are distance sampling and mark-recapture methods (Marques et al., 2011, 2013, Küsel et al., 2011, Martin et al., 2013, Ward et al., 2012). However, they rely on recording individual whale calls. To determine the distribution of an entire population on an ocean basin-scale, this again requires an unrealistically large number of recorders. In this thesis, I present a different approach to estimate marine mammal distribution: Not by analyzing individual vocalizations but the chorus generated by all calling whales.

Depending on the local ambient noise levels from physical and anthropogenic sources, the marine mammal chorus can then be seen as a peak in recorded ambient noise spectra. Ambient noise spectra are calculated from spectral averages of sound recordings. To show how a spectrum changes over time, it is commonly visualized as a spectrogram. In a spectrogram, the time and frequency are represented by the x and y axis and the power spectral density by the color of each pixel. Figure 2 shows a 3 year long ambient noise spectrogram from the Southern Ocean containing 3 whale choruses (Menze, 2012). The horizontal line at 27 Hz is the blue whale chorus, the annually reoccurring line at 98 Hz the fin whale chorus and the annually reoccurring broad peak between 100 and 300 Hz is the Antarctic minke whale chorus. The spectrogram shows considerable intra- and inter-annual variation in the strength of the marine mammal choruses. This is connected to changes in the distribution and behavior of the vocalizing whales. How to use data from ambient noise spectra to estimate the distribution of calling whales will be presented in the methods section.

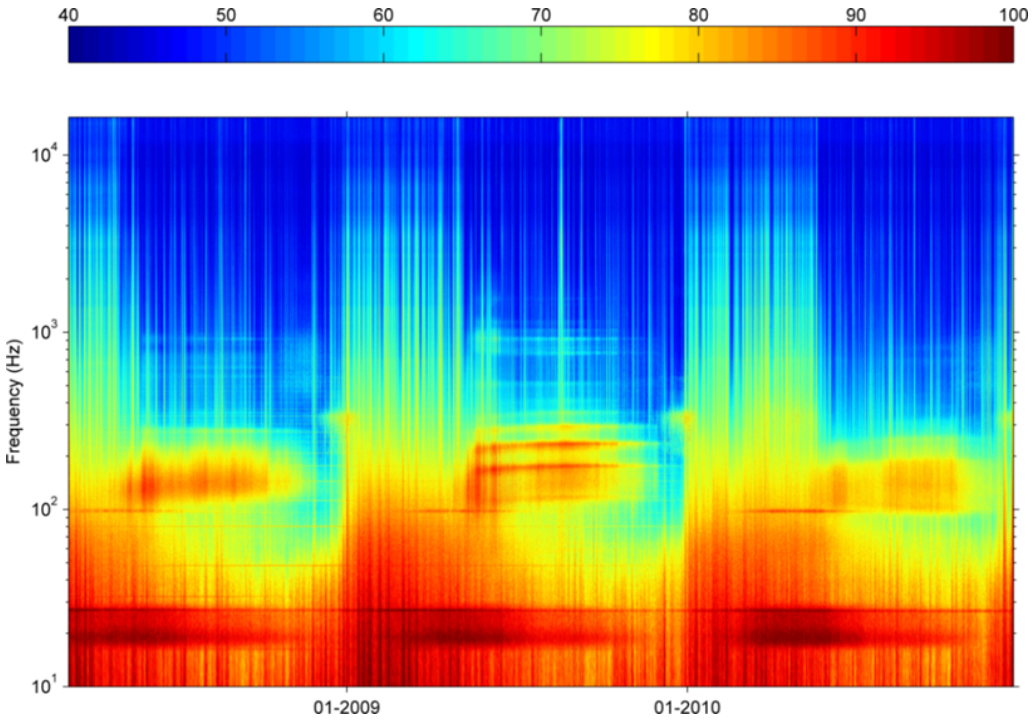

Figure 2: Spectrogram of ambient noise recordings at 66°S, 0°E in the Southern Ocean. X axis represents time, y axis frequency and color the power spectral density (PSD in dB re 1 µPa^2 Hz^{-1}). Sawtooth like pattern in the background represents noise variation caused by annual change in sea ice cover. Vertical spikes are caused by storm events and horizontal line represent the different marine mammal choruses as described in table 1. From Menze (2012).

2.3. Fin whales

Fin whales (*Balaenoptera physalus*) can be found from high to low latitudes, but are most common in cold and temperate waters. The global fin whale population can be divided into a Southern and Northern hemisphere stock, that rarely mix (Perrin et al., 2009). During industrial whaling both populations were brought close to extinction. A recent study by Rocha, Jr. et al. (2015) reports that about 874 068 fin whales were killed during industrialized whaling between 1909-1999. The Northern hemisphere stock can be separated into the North Atlantic and North Pacific stock. The management of whale stocks is an international political effort. Since the habitat of most whale species rarely falls into the jurisdiction of a single nation, international committees were formed. The international whaling commission (IWC) manages whales stocks on a global level. Several nations surrounding the North Atlantic, founded a separate commission to manage the marine mammal stocks in their jurisdiction: The North Atlantic Marine Mammal Commission (NAMMCO). The IWC's current estimate for the North Atlantic fin whale population is 26 500 animals (IWC, 2015). The NAMMCO gives a similar number: Between 18,186 and 30,214 whales (Víkingsson et al., 2013). The IWC and NAMMCO divide the North Atlantic fin whale population into 5 stocks: West Greenland, East Greenland – Iceland, North Norway, West Norway and Faroe Islands and British Isles, Spain and Portugal (NAMMCO, 2015, Donovan, 1991). Figure 3 shows the boundaries of the putative stock

areas. The population structure adopted by the IWC and NAMMCO, is based on visual surveys and catch data from whaling operations (Donovan, 1991). Given these sparse data, the stocks are only a rough approximation of the true population structure. A good example for this, is the fin whale population in the Mediterranean sea. They are thought to be separate from the North Atlantic stocks (Notarbartolo-di Sciara et al., 2003). However, an acoustic survey by Castellote et al. (2004), found that fin whales from the Icelandic stock seem to migrate through the Strait of Gibraltar into the Mediterranean. A genetic study on the other hand, roughly confirms the separate stocks as adopted by the IWC and NAMMCO (Bérubé et al., 1998).

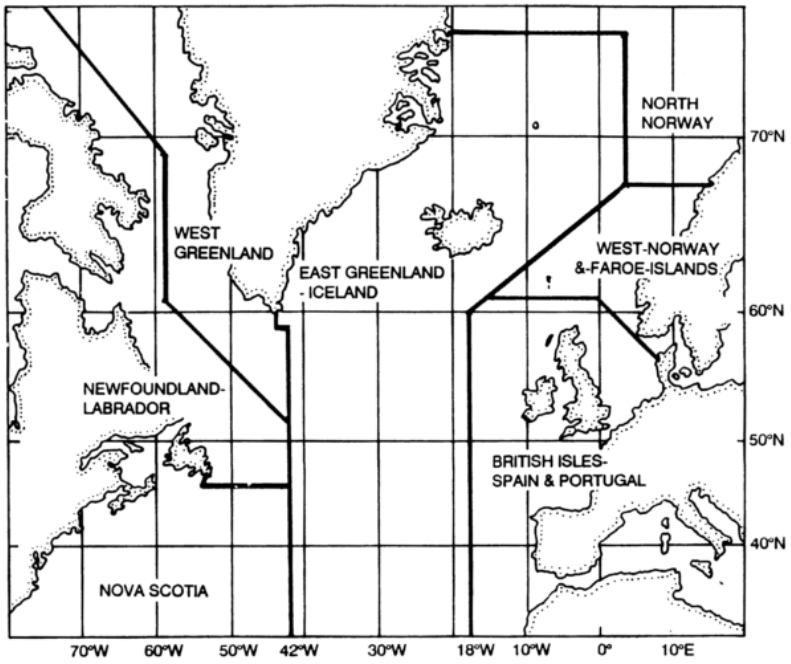

Figure 3: Map showing the borders of the putative stock areas as used by the IWC and NAMMCO. From Donovan (1991).

Since 1988, the NAMMCO conducts visual surveys of the fin whale distribution between Greenland and Europe (Víkingsson et al., 2013). These surveys found that fin whale sightings where clustered along the coast of Greenland, the Iceland-Faroe ridge as well as on the West coast of Svalbard (Figure 4). The surveys were performed using several research vessels in June and July of each survey year, and indicate relatively stable summer distribution patterns throughout the years. Víkingsson et al. (2013) estimated an increase in North Atlantic fin whale abundance from 17 482 animals in 1988 to 29 891 animals in 2001. In the Norwegian sea only, Øien (2004) estimated and abundance of 5,034 fin whales.

Other visual surveys on fin whale summer distribution report fin whales along the Spanish coast and in the Bay of Biscay (Hammond et al., 2009), whereas comparatively few fin whales were sighted along the mid Atlantic ridge (Waring et al., 2008). All of the described surveys were performed in the summer months. Very little literature exists on

sightings of fin whales during the three other seasons. A land based survey by Silva et al. (2014) on the Azores, sighted fin whales mainly in spring and summer, but also in late autumn and winter. Fin whales that were tagged in spring off the Azores showed migratory behavior towards East Greenland and Iceland Silva et al. (2013).

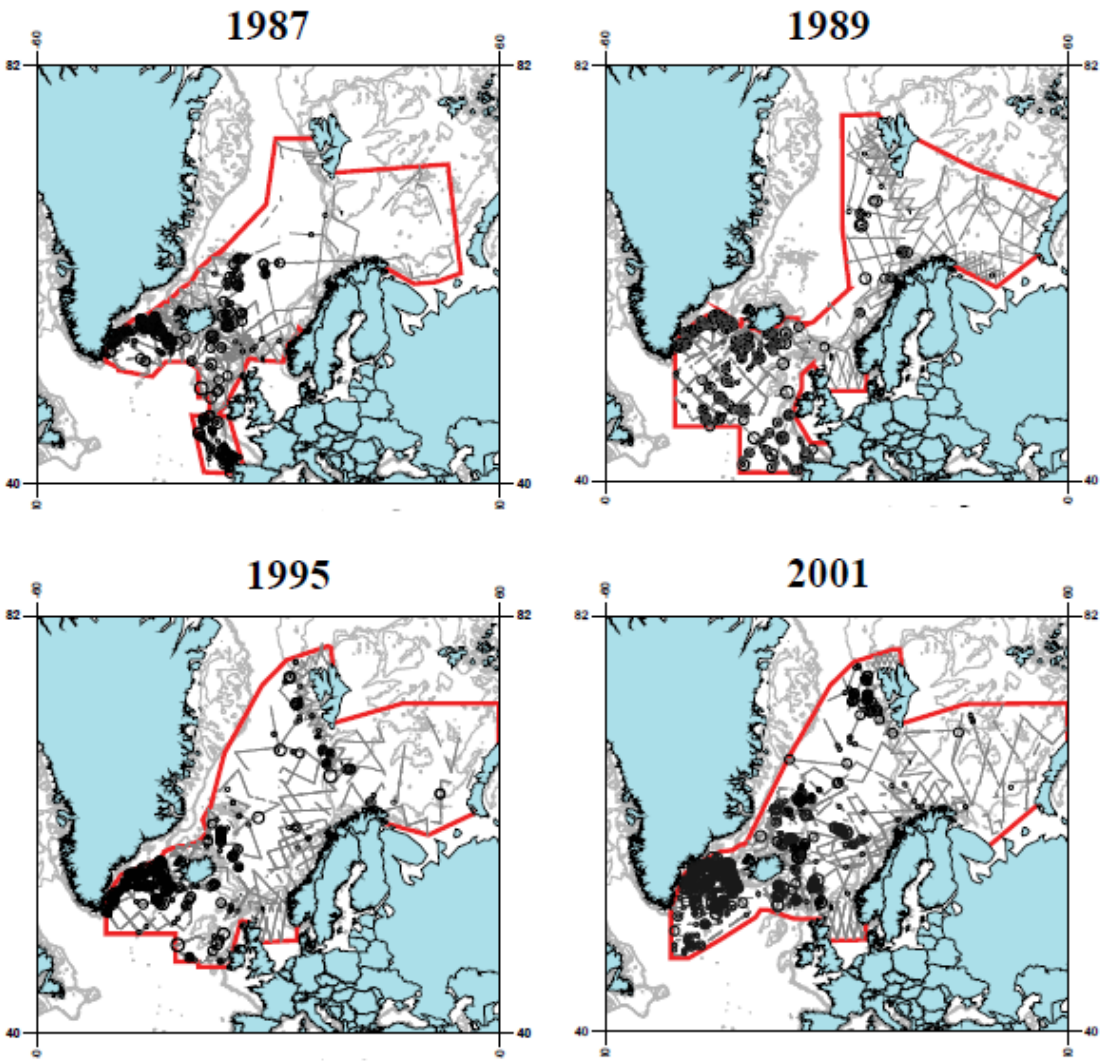

Figure 4: Sightings of fin whales during the NASS ship surveys (1987 to 2001). Gray lines show the survey tracks and the circles fin whale sightings (symbol size is proportional to group size from 1 to 4+). From Víkingsson et al. (2013)

The mating season of fin whales is between December and February (Perrin et al., 2009). Their winter distribution, presumably at their breeding grounds, remains largely unknown. Assuming a simple north-south migration between feeding and breeding grounds might oversimplify fin whale migration. It has been hypothesized that some populations do not migrate, or that one populations' feeding ground is another populations' breeding ground (Mizroch et al., 2009). Daylight and weather conditions render visual surveys difficult during winter, creating a lack of data on the distribution of fin whales during the

mating season. The calling activity of fin whales, which is mainly observed in winter (Watkins et al., 1987, Simon et al., 2010, Nieukirk et al., 2012), can help to fill this knowledge gap.

Fin whales emit pulsed vocalizations that have been recorded since the 1960s. Early underwater acoustic research was mainly led by the US navy, which was highly interested in this suspicious signal (Nichols, 2005). Watkins et al. (1987) could eventually show that fin whales and not Russian submarines were the sources of these remarkably regular sounds. Pioneering work on underwater ambient noise led by Wenz (1962) had already correctly identified whales as sources of ambient noise at certain frequencies.

Fin whale vocalizations are down-sweeps from 23 to 18 Hz, sometimes accompanied by a higher frequency down sweep (around 100 Hz) that varies between populations. However, most energy is contained in the 20 Hz pulse. Figure 5 shows an example fin whale pulse train and the fin whale chorus. The average fin whale source level has been estimated as 189 dB re 1 µPa (Weirathmueller et al., 2013, Watkins et al., 1987, Sirović et al., 2007). The higher frequency component of the call can only be observed under low noise conditions, since it contains much less energy. Simon et al. (2010) have observed it around 130 Hz in West of Greenland. In the Southern Ocean it has been observed at 89 Hz west of the Antarctic peninsula (Sirović et al., 2007) and at 98 Hz east of the Antarctic peninsula (Menze, 2012).

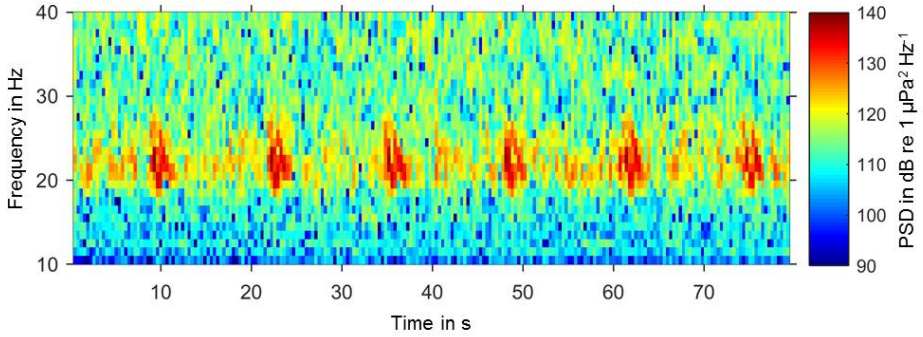

Figure 5: Spectrogram of fin whale pulse train recored in Fram Strait: x axis represents time, y axis frequency and color the power spectral density. Fin whale calls visible as down-sweeps from 23 to 18 Hz. Fin whale chorus visible as red band at 20 Hz.

A study by Croll et al. (2002) in the Gulf of California found that only male fin whales vocalize. This supports the hypothesis that fin whale calls serve to attract mating partners, as proposed by Payne and Webb (1971). They furthermore observed a 1:1 sex ratio and that the whales foraged on dense patches of krill. Thus their conclusion was that male fin whales likely vocalize to attract females to favorable feeding locations (dense aggregation of prey).

The depth at which fin whales vocalize has been described as around 50 m by Watkins et al. (1987). The depth of the vocalizing animal influences the shape of the acoustic near field, due to interference with surface reflected sound waves. Weirathmueller et al. (2013)

modeled this effect for fin whale calls and found a variability of ± 6 dB with depth in the near field. For the basin-scale distances (>100 km) between source and receiver considered in this thesis, near field interference due to source depth variation seems negligible.

The vocalizations are emitted in regular pulse trains, each lasting between hours and days (Watkins et al., 1987). The pulses are commonly emitted with a constant inter pulse interval (IPI). But it has also been observed that the pulse trains alternate between a shorter and a longer IPI (Watkins et al., 1987). In the North Pacific Watkins et al. (1987) found IPIs ranging between 7-26 s with a mean of 12.48 s. Further studies showed that the IPI varies between populations, similar to the high frequency pulse component. Delarue et al. (2009) found that the IPI recorded in the Gulf of Maine and Gulf of St. Lawrence differs significantly and supports the notion of distinct populations. However, defining distinct populations based on their IPI remains difficult. Morano et al. (2012) found that the IPI of fin whales along the American coast changes seasonally: from 9.6 s in September–January to 15.1 s in March–May. A similar seasonal modulation of IPI exists in the North Pacific (Oleson et al., 2014).

Fin whale pulse trains have been frequently recorded in the North Atlantic, North Pacific and Southern Ocean (Nieukirk et al., 2012, Watkins et al., 2000, Širović et al., 2004). The fin whale chorus (the combined pulse trains of all vocalizing animals) has been recorded and described in the North Atlantic and Southern Ocean. Figure 6 shows a map of all published fin whale chorus observations.

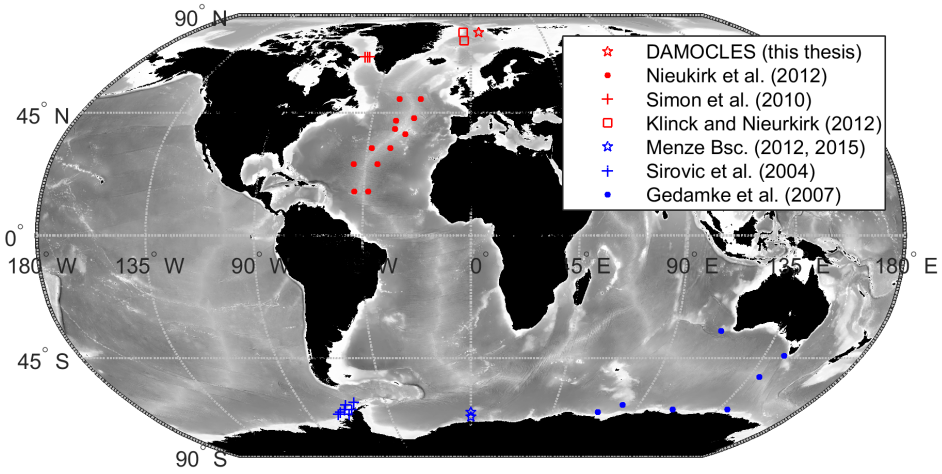

Figure 6: Map showing fin whale chorus observations in the Northern (red) and Southern (blue) hemisphere.

The recorder array used by Nieukirk et al. (2012) monitored the North Atlantic fin whale chorus with a high spatial resolution. The authors described the fin whales chorus with a measure termed fin index. The exact method will be discussed in section 5.1. Figure 7 displays the fin index time series recorded by Nieukirk et al. (2012) using moored recorders along the mid Atlantic ridge. They found that the fin index is strongest north

of 32°N and increased during the late summer and fall months throughout the North Atlantic. Peak levels were reached in December and January and within the likely mating period. Simon et al. (2010) found that in the Davis strait (West of Greenland), the fin index peaked in November and December. The fin index in Davis strait was partly following a diel rhythm, being stronger during the dark hours and weaker during daylight hours. This indicates a link between calling activity and feeding. A similar diel marine mammal chorus rhythm can be found in Antarctic minke whales and is synchronous to the diel vertical migration of krill (Menze, 2012). The fin index observed by Klinck and Nieukirk (2012) East of Greenland and in the Fram strait peaked in December and January. The northernmost fin whale chorus observation has been made by Hope (2013) at 84°N, deep in the Arctic sea ice in September 2012.

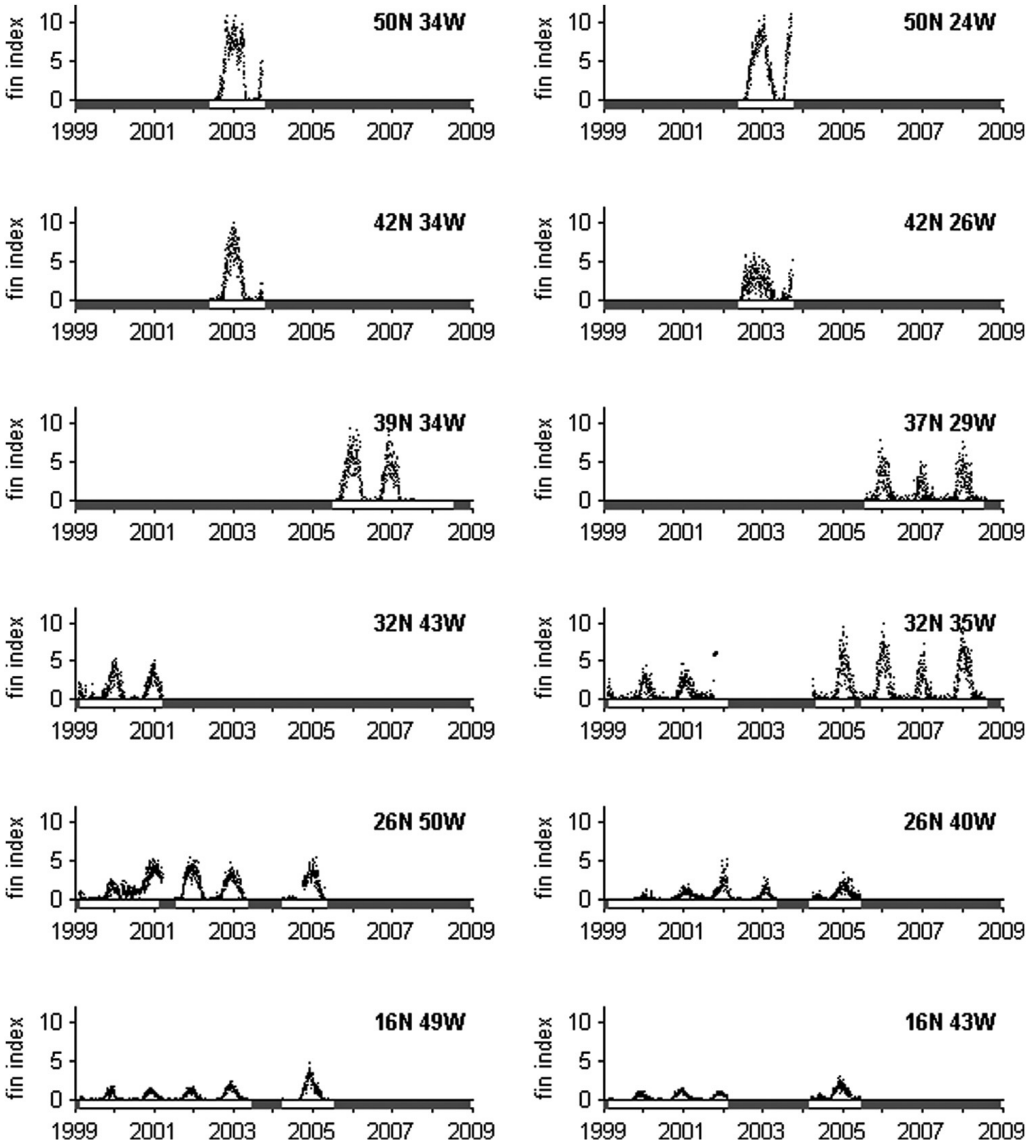

Figure 7: Fin index observations in the mid North Atlantic by Nieukirk et al. (2012)

3. Underwater sound propagation

3.1. Acoustic waves

Sound energy in a fluid propagates in the form of pressure waves. These can be described with the acoustic wave equation (Equation 1, Lurton (2002)).

$$\nabla^2 p - \frac{1}{c^2}\frac{\partial^2 p}{\partial t^2} = 0 \tag{1}$$

Here p represent the acoustic pressure, c the sound speed, x, y, z the spatial dimensions and t time. Solutions of varying complexity exist for equation 1. Two simple solutions are plane waves and spherical waves, which also form the basis of the transmission loss models described in section 3.3. When assuming sinusoidal waves in one dimensional space with constant sound speed, plane waves (Eq. 2) are a solution to the acoustic wave equation.

$$p(x,t) = p_0 e^{(i\omega(t-\frac{x}{c}))} \tag{2}$$

Here ω represents the circular frequency. This equation describes that surfaces of constant phase are planes normal to the x direction.

If we on the other hand assume a point source in a homogeneous infinite three dimensional medium, spherical waves are a solution to equation 1.

$$p(r,t) = \frac{p_0}{r} e^{(i\omega(t-\frac{r}{c}))} \tag{3}$$

These waves propagate simultaneously in all three dimensions. The surfaces of constant phase (wave front) take the form of spheres around the point source. The variable r represents the radius of this sphere. At ranges far away from the point source, the curvature of the wave front can be neglected. This allows us to approximately describe spherical waves using the plane wave equation.

The recording of underwater sound involves the use of hydrophones, that act as sound receivers. The sound pressure (emitted by a sound source) that arrives at a receiver is described by the sonar equation:

$$\begin{aligned} RL(x_r, y_r, z_r, t, f) = \quad & SL(x_s, y_s, z_s, t, f) - TL(x_s, y_s, z_s, x_r, y_r, z_r, t, f, \tau) \\ & -NL(x_r, y_r, z_r, t, f, \tau) \end{aligned} \tag{4}$$

In this equation, RL stands for received sound pressure level, SL for the source sound pressure level, TL for the transmission loss and NL for the noise level at the receiver. The variables x_s, y_s, z_s stand for the source position, those with index $_r$ for receiver position, t represents time, f frequency and τ varying environmental conditions (for example the sound speed profile). A wave propagating though the ocean is subject to attenuation, in the context of sound sources and receivers this is termed transmission loss. It is caused by absorption, scattering, refraction and reflection of the acoustic wave.

In sea water, absorption is an effect of the viscosity of water, chemical reactions and heat loss (Lurton, 2002). To calculate the absorption loss depending on frequency, temperature, salinity and depth the empirical model of Francois and Garrison (1982) is widely

used. It describes how the viscosity of sea water, magnesium sulfate and boric acid ions absorb the energy of an acoustic wave. For the low frequencies considered in this thesis, the relaxation of boric acid ions and viscosity are the main causes for absorption. Figure 8 shows the absorption coefficients for sea water over frequency. In general, the absorption coefficient increases with increasing frequency. In this thesis the Francois-Garrison model is part of all transmission loss estimates.

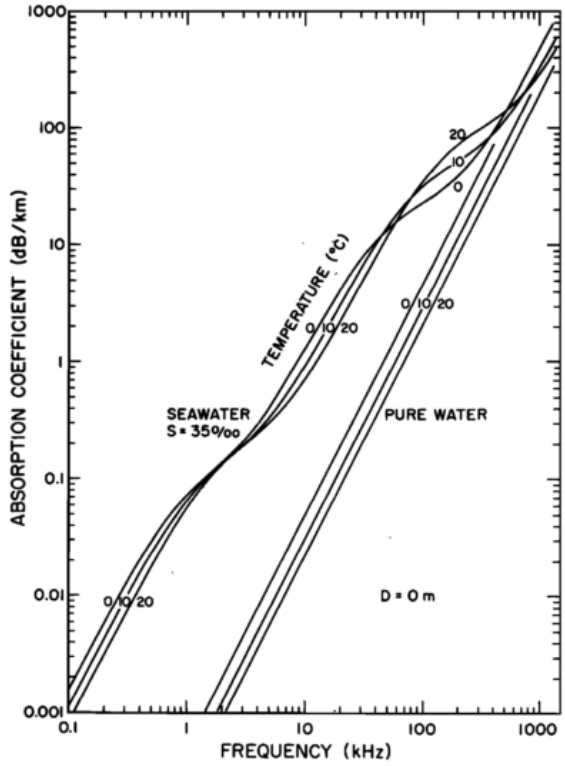

Figure 8: Absorption coefficients for sea water over frequency: for three temperatures values (0,10 and 20 °C), a salinity of 35 PSU and a pH of 8. From Francois and Garrison (1982)

In addition to absorption, sound energy is attenuated by reflection and refraction. Reflection occurs at the sea surface and the sea floor, but can also occur within the water column due to convex sound speed profiles.

The sound speed c in the ocean is not a constant, but a function of temperature, salinity and pressure. As with absorption, empirical models have been derived from measurements, leading to a standardized UNESCO reference model. In general sound speed increases mostly with temperature and pressure (Lurton, 2002). Salinity has a minor but not negligible effect. In contrast to a medium with uniform sound speed, acoustic wave fronts in the ocean will thus not have the idealized spherical or plane shape. A sound wave is refracted when passing regions of variable sound speed. If the sound speed gradient is large enough this can even lead to the total internal reflection of a sound wave. This process leads to the formation of so called sound channels, that are located at the

depth of sound speed minima (Lurton, 2002). A wave entering such a channel will always be reflected back into it. This leads to reduced interaction with the sea floor and sea surface, and thus allows sound waves to propagate over large ranges and with little attenuation. In low and mid latitude oceans with warm surface layers a deep sound channel exists. It is often called the SOFAR (sound fixing and ranging) channel. In high latitude oceans, especially in ice covered regions, the sound speed minimum is located at or near the sea surface. This leads to a surface channel, where the wave fronts are repeatedly reflected towards the sea surface. Figure 9 illustrates the path of waves being trapped in a surface channel.

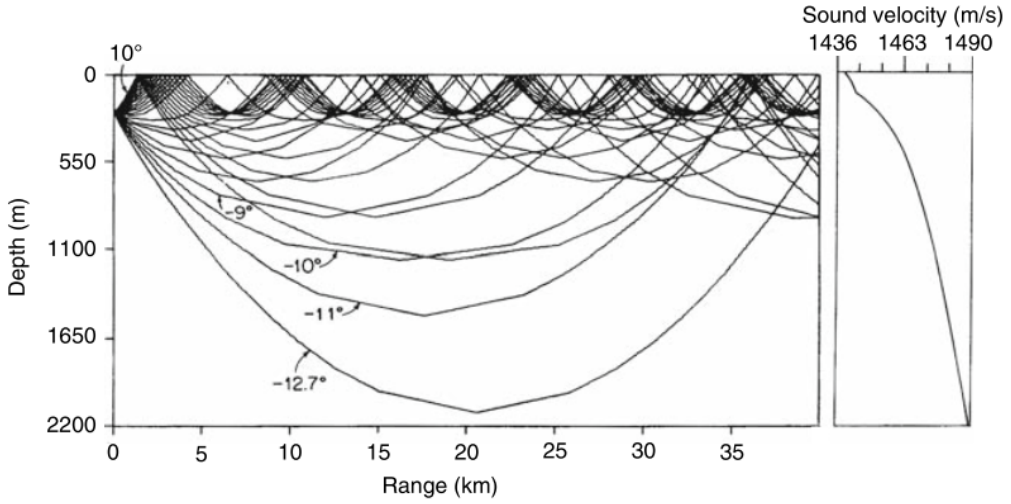

Figure 9: Propagation paths (rays) of plane waves given a sound speed profile with the sound speed minimum at the surface. The sound speed profile is depicted to the right. From Urick (1983).

When the wave front hits the sea surface it is reflected according to Snells law (Lurton, 2002). However, a part of the sound energy is also scattered and absorbed by the rough sea surface or sea ice. How much the wave amplitude is reduced after each reflection varies with frequency and can be described with a reflection coefficient. Similarly to the absorption coefficient, higher frequencies are attenuated more than lower ones. Thus wave reflection at the sea surface or underside of sea ice, acts as a low pass filter (Diachok, 1980). The magnitude of the transmission loss due to surface reflection changes with sea state and sea ice conditions. Reflection also occurs at the sea floor. However the reflection coefficient varies greatly with the material and structure of the sea floor. Sediment that overlies the base rock can have similar sound speeds to water (Lurton, 2002). Depending on the structure of the sea floor, very complex wave propagation paths will occur. Implementing these correctly is one of the many challenges in underwater sound propagation modeling.

3.2. Geometrical spreading transmission loss

One of the simplest ways to calculate transmission loss is geometrical spreading. The attenuation due to sound speed variation as well as sea floor and surface reflection are neglected. It is assumed that initially, the sound wave propagates spherically according to equation 3. The intensity of the wave is defined as power P passing through a unit area. Since energy is conserved, the intensity I of the wave will decrease with increasing radius of the sphere:

$$\begin{aligned} P &= 4\pi r^2 I_r \\ P_{1\ m} &= P_r \\ \frac{I_r}{I_{1m}} &= \frac{4\pi r^2}{4\pi r_{1m}^2} \end{aligned} \tag{5}$$

If the absorption coefficient α is added and the intensity ratio is converted to the decibel scale, the equation for spherical transmission loss becomes:

$$TL(r) = 20\ log(\frac{r}{r_{1m}}) + \alpha r \tag{6}$$

This equation roughly holds until the sound wave hits the sea floor and sea surface. From then on it can no longer propagate spherically but is trapped and forced to propagate in cylindrical form. The radius to where the wave propagates spherically is described by the radius $r_{critical}$. To calculate the transmission loss for ranges larger than $r_{critical}$, one needs to assume cylindrical spreading. This results in the following equation where r can be a range larger than $r_{critical}$ (Lurton, 2002):

$$TL(r) = 20\ log(\frac{r_{critical}}{r_{1m}}) + 10\ log(\frac{r}{r_{critical}}) + \alpha r \tag{7}$$

This simple description of the initial spherical and then cylindrical spreading of an acoustic wave in the ocean is a basic but still useful transmission loss estimate.

3.3. Ray trace sound propagation modeling

To include the effects of bathymetry and variable sound speeds on transmission loss, more sophisticated sound propagation models are required. A commonly used class of models for this purpose, are ray trace models (Lurton, 2002, Hovem, 2013). The key assumptions of raytracing is, that the wave front can be approximated as a fan of rays emerging from the source (Porter and Liu, 1994). Figure 9 shows an example of multiple ray paths. Each of these rays represents the path of a plane wave (Eq. 2). The path each ray takes is defined by Snells law of refraction and the sound speed gradient. If a ray hits the sea floor or sea surface, it is reflected according to Snells law and a specific reflection coefficient. The resulting sound pressure field can then be calculated by combining the sound pressure from each ray. Next to estimating the transmission loss, this method can also be used to calculate the impulse response for any given location (Porter and Liu, 1994).

Most available raytracing models are range dependent: They can calculate the sound pressure field depending on depth and radius from the sound source. Fully 3 dimensional raytracing models are theoretically possible, but not common due to their heavy computational requirements (Lurton, 2002). Instead it is common to rotate the 2-D slices

created by a range depended model, over 360° around the sources. This approach is often termed 2xN dimensional modeling. Unfortunately this methods does not implement ray reflections in the horizontal axis and is thus likely inaccurate around shelf slopes and sea mounts (Sturm et al., 2008). The rays interaction with the sea floor can be modeled with varying complexity, depending on the sea floor's layering and properties. Often it is simply assumed as acousto-elastic half space with constant sound and shear wave speed.

Next to raytracing, other types of underwater sound propagation models exist. A large family of models is based on solving the wave equation using normal modes. These models can be used to simulate spreading of sound around islands and sea mounts, but rarely include range depend sound speed (Heaney et al., 2013, Ballard, 2012). The most recent approaches include parabolic equation and fast field models, that have the advantage of being very accurate, but the disadvantage of heavy computational requirements (Lurton, 2002). For the purpose of estimating the transmission loss between vocalizing fin whales and a set of recorders, ray trace models are considered sufficient enough (McDonald and Fox, 1999).

4. Inverse theory

4.1. Bayesian inversion

Inverse theory describes how to estimate a set of unknown parameters from indirect measurements (Tarantola, 2006). It is almost always impossible, to obtain a perfect set of measurements describing all parameters of a system. We will, for example, never be able to record or sight all whales in the ocean. To estimate the whale distribution, an inverse theory which interprets the few recordings or sightings available is needed. The first step towards solving an inverse problem is, to know how the unknown parameters and observed data are connected. This part is termed the forward operator or forward model (Tarantola, 2004). The forward operator g describes which data vector $\boldsymbol{d}$ is produced by a parameter vector $\boldsymbol{m}$:

$$\boldsymbol{d} = g(\boldsymbol{m}) \tag{8}$$

The forward operator g could for example stand for an acoustic propagation model, $\boldsymbol{m}$ for a set of sound sources and $\boldsymbol{d}$ for sound pressure recordings. For many physical problems it is not possible to find the inverse of g directly (Snieder and Trampert, 1999). This can be caused by the mathematical formulation of the forward problem or a lack of data $\boldsymbol{d}$. In the case of marine mammal choruses we deal with sound pressure from many dispersed sources, so that many source combinations can produce similar sound pressure observations.

A special case occurs if the forward problem is linear, then $g(\boldsymbol{m})$ is a function of the type $\boldsymbol{d} = \boldsymbol{G}\boldsymbol{m}$ (Tarantola, 2004). This simplifies the estimation of the correct solution to the inverse problem. However, even if the forward problem can be expressed as a set of linear equations, most inverse problems are ill-posed and ill-determined (Snieder and Trampert, 1999). This means that there is not enough data points $\boldsymbol{d}$ as well as contradicting data, to determine a unique solution $\boldsymbol{m}$. Linear algebra determines that for a set of linear equations there are either infinitely many, one or no solutions at all. Similar dilemmas can be found in nonlinear inverse theory.

Most progress in solving extremely under-determined inverse problems has been made in the field of geophysics (Snieder and Trampert, 1999). In this thesis I will follow the Bayesian approach described by Tarantola (2004). It embraces the fact, that the observed data and forward model are uncertain and can be described using probability distributions. Calculating with probability distributions has the advantage, that Bayesian reasoning can be applied (Tarantola, 2004, Allmaras et al., 2013). This means that we can work with *a priori* (independent of observation, before reasoning) and *a posteriori* information (information acquired by observation, after reasoning).

The a priori information feeds into how the forward model is designed and describes the a priori probability distribution over the parameter space. The solution of the inverse problem is to find the posterior probability of the parameters $\boldsymbol{m}$ given the data $\boldsymbol{d}$. To simplify the notation, I follow Tarantola (2004) and define $\rho(\boldsymbol{m})$ as prior probability distribution over the parameter space and $\sigma(\boldsymbol{m})$ as posterior probability distribution over the parameter space. Figure 10 shows a general scheme of an inverse problem including Bayesian reasoning. The steps to solve it include defining the a priori distribution $\rho(\boldsymbol{m})$, defining a

suitable forward model to calculate $\boldsymbol{d}_{simulated}$ from $\boldsymbol{m}$, appraising how well the simulated data $\boldsymbol{d}_{simulated}$ fit to the observed data $\boldsymbol{d}_{observed}$ and estimating the likely forward model parameters $\boldsymbol{m}$ given the observed data (the posterior distribution $\sigma(\boldsymbol{m})$).

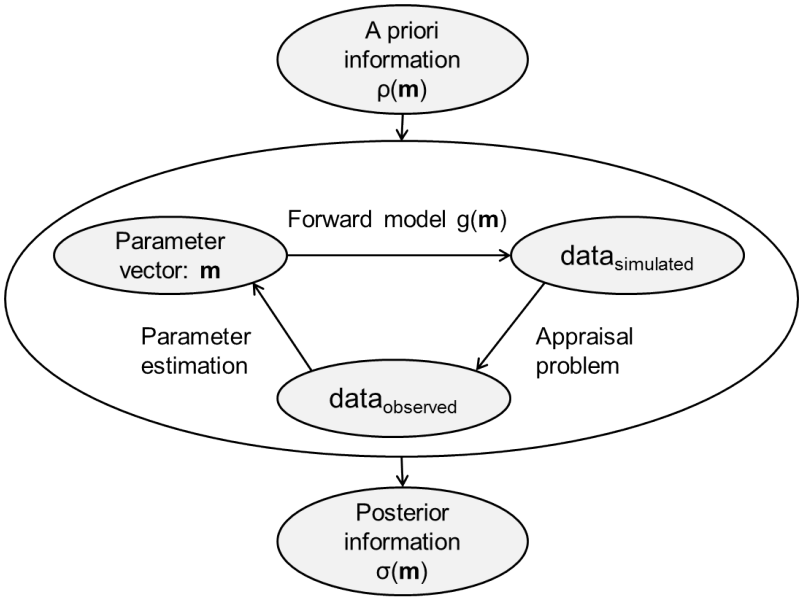

Figure 10: General formulation of an inverse problem including Bayesian reasoning. Adapted from Snieder and Trampert (1999).

Every combination of forward model parameters $\boldsymbol{m}$ produces corresponding data as given by $\boldsymbol{d} = g(\boldsymbol{m})$. If we assume our forward model to be perfect, data and model will be connected by a line in the data and parameter space, as shown in figure 11. Since knowing the perfect forward model is unrealistic, a better approach is to describe the output of the forward model with Gaussian uncertainties (with the standard deviation s). The forward model and data are then connected by the joint probability distribution $\theta(\boldsymbol{d}|\boldsymbol{m})$, that describes the probability of the data $\boldsymbol{d}$ for a given set of parameters $\boldsymbol{m}$. It is shown in the right panel of figure 11.

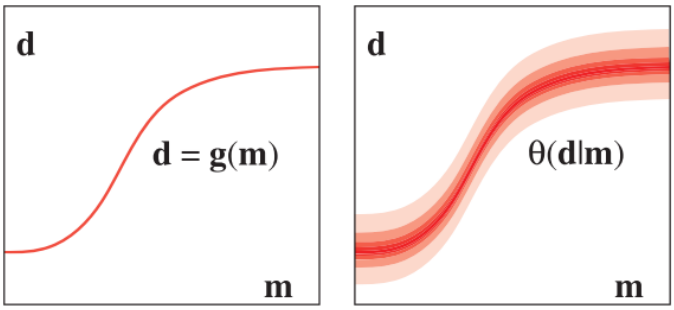

Figure 11: Comparison between a perfect forward model $\boldsymbol{d} = g(\boldsymbol{m})$ (left panel) and a forward model that produces the probability distribution $\theta(\boldsymbol{d}|\boldsymbol{m})$ with the standard deviation s (right panel). X axis shows model parameter value, y axis data value. From Tarantola (2004).

The observations are given as probability distribution in data space: $\rho(\boldsymbol{d})$. Normally the observed data has a very narrow probability distribution, so that it is often assumed perfect. Together the prior information in parameter and data space form the joint prior probability distribution $\rho(\boldsymbol{d}, \boldsymbol{m})$. Figure 12 illustrates $\rho(\boldsymbol{d}, \boldsymbol{m})$ as 2-D Gaussian distribution in the left panel. In this graphical example, model and data space have one dimension each. The marginal prior probability distribution in data and parameter space ($\rho(\boldsymbol{d})$ and $\rho(\boldsymbol{m})$) are shown as one dimensional Gaussian to the left and below the panel.

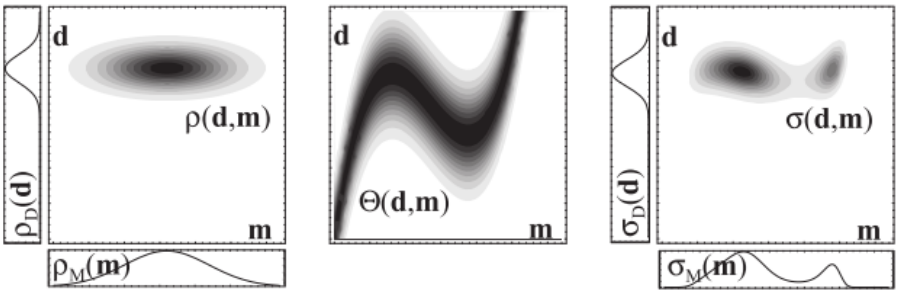

Figure 12: General representation of a Bayesian solution of an inverse problem: x axis show model parameter value, y axis data value. The left panel displays the joint prior probability distribution $\rho(\boldsymbol{d}, \boldsymbol{m})$, the middle panel displays $\theta(\boldsymbol{d}, \boldsymbol{m})$ (the probability the forward model assigns to the data $\boldsymbol{d}$ for a given parameter $\boldsymbol{m}$), and the right panel displays the joint posterior probability distribution $\sigma(\boldsymbol{d}, \boldsymbol{m})$. From Tarantola (2004).

The joint posterior probability distribution $\sigma(\boldsymbol{d}, \boldsymbol{m})$ in data and parameter space can be calculated by combining the prior information $\rho(\boldsymbol{d}, \boldsymbol{m})$ with the information we have about the forward model $\theta(\boldsymbol{d}|\boldsymbol{m})$. It is the conjunction of $\rho(\boldsymbol{d}, \boldsymbol{m})$ and $\theta(\boldsymbol{d}|\boldsymbol{m})$, which can be seen in the right panel of figure 12 (Tarantola, 2004). The solution of the inverse problem, the posterior probability distribution over the parameter space $\sigma(\boldsymbol{m})$, is then a marginal probability distribution. It is shown below the right panel of figure 12 and can be calculated using the following equation (Tarantola, 2004):

$$\sigma(\boldsymbol{m}) = k\rho(\boldsymbol{m}) \int_D \frac{\rho(\boldsymbol{d})\theta(\boldsymbol{d}|\boldsymbol{m})}{\mu(\boldsymbol{d})} d\boldsymbol{d} \tag{9}$$

Where D represents the data space, k a normalization constant and $\mu(\boldsymbol{d})$ the homogeneous probability density over the parameter space. If the parameter space is linear, the term $\int_D \frac{\rho(\boldsymbol{d})\theta(\boldsymbol{d}|\boldsymbol{m})}{\mu(\boldsymbol{d})} d\boldsymbol{d}$ can be replaced by the likelihood function $L(\boldsymbol{m})$ (Tarantola, 2004). It describes how well the parameters $\boldsymbol{m}$ fit to the data $\boldsymbol{d}$, so that equation 9 becomes:

$$\sigma(\boldsymbol{m}) = k\rho(\boldsymbol{m})L(\boldsymbol{m}) \tag{10}$$

Here k is again a normalization constant. The likelihood function $L(\boldsymbol{m})$ is commonly expressed as exponential of the negative misfit function $S(\boldsymbol{m})$ (Mosegaard and Sambridge, 2002):

$$L(\boldsymbol{m}) = ke^{-S(\boldsymbol{m})} \tag{11}$$

The uncertainty of the forward model (the standard deviation s) needs to be considered when determining the misfit between observed and simulated data. The misfit is a measure of distance between the observed and simulated data points, also referred to as a norm in the literature (Tarantola, 2004). The general equation for the misfit $S(\boldsymbol{m})$ is:

$$S(\boldsymbol{m}) = \frac{1}{p} \sum_{i}^{n_{data}} \frac{|g_i(\boldsymbol{m}) - d_i|^p}{s_i^p} \tag{12}$$

Where p is the order of the norm and s the standard deviation of the forward model. It is common to use l_2 norm ($p = 2$) which is the sum of squared errors (SSE) between true and simulated data (Tarantola, 2004). This has the advantage of being robust to the influence of outliers. However, it has the disadvantage of being sensitive to the location of the data points in data space, a property termed stability. The l in the description of a norm stands for "least". Other measures of distance between data points change the order of the norm (between l_0 to l_∞). In this thesis the misfit is determined using the l_2 norm:

$$S(\boldsymbol{m}) = \frac{1}{2} \sum_{i=1}^{n_{data}} \frac{(g_i(\boldsymbol{m}) - d_i)^2}{s^2} \tag{13}$$

To find the most likely parameters (for example the most likely distribution of vocalizing whales) that explain the observed data $\boldsymbol{d}$, one needs to find the maximum of the posterior distribution $\sigma(\boldsymbol{m})$, which equals finding the maximum of the likelihood function (Eq. 11):

$$\text{max}(\sigma(\boldsymbol{m})) = \text{max}(e^{-S(\boldsymbol{m})}) \tag{14}$$

This approach is termed the maximum likelihood method (Allmaras et al., 2013). For well determined linear systems, analytical solutions to this problem exist. However for under-determined inverse problems (as most real world problems are), finding the maximum of $\sigma(\boldsymbol{m})$ is not a trivial task. Numerical techniques that sample the likelihood functions are needed. The next section presents an example problem with two forward model parameters to illustrate the misfit and likelihood functions.

4.2. Example problem with 2 parameters

This sections presents the misfit and likelihood functions for a simplified sound source and receiver problem. The example problem consists of 2 sound sources at fixed locations and a varying number of recorders. The emitted and received sound signals are assumed constant, so that time can be neglect. To simplify the problem, latitude, longitude and depth of the sources and receiver are ignored and range is the only spatial dimension. The locations of the sound sources are at 50 and 80 km range and their source levels are 50 and 70 dB re 1 µPa respectively. Two recorder scenarios are used: One where 10 recorders are distributed evenly over the range, and another where 100 recorders are also distributed evenly over the range. The received level the recorders measure is calculated using the sonar equation (Eq. 4) and the cylindrical spreading transmission loss equation (Eq. 7). Figure 13 shows the locations as well as source and received levels for the two sources and recorder scenarios.

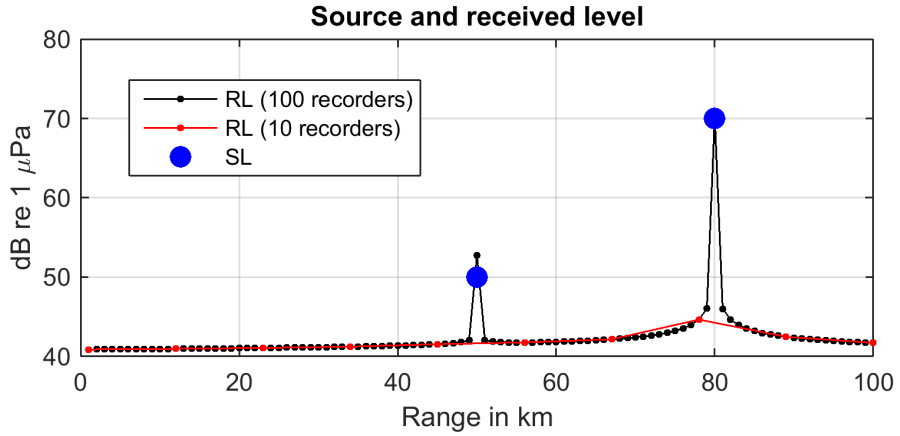

Figure 13: Example of parameter estimation problem including two fixed sources and cylindrical transmission loss over range. Blue dots represent the true source level for each source, lines with dots the received levels for a recorder at that location.

This example can now be reformulated as an inverse problem. The observed data $\boldsymbol{d}$ is given by the received levels of the recorders and the unknown parameters $\boldsymbol{m}$ are the source levels of the 2 sources. This means the likelihood and misfit functions will have 2 dimensions and are easy to visualize. The forward model is given by the sonar equation (Eq. 4), that calculates the received level for each recorder, and the cylindrical spreading transmission loss equation (Eq. 7). This inverse problem is well-determined: There are more data points $\boldsymbol{d}$ (recorders) than parameters $\boldsymbol{m}$ (source level).

The misfit and likelihood values for each parameter combination between 0 and 100 dB re 1 µPa (source level combination) are calculated using equation 13 and 11. The forward model standard deviation is assumed as 5 dB. Figure 14 shows the misfit and likelihood functions for both the 10 and 100 recorder scenario.

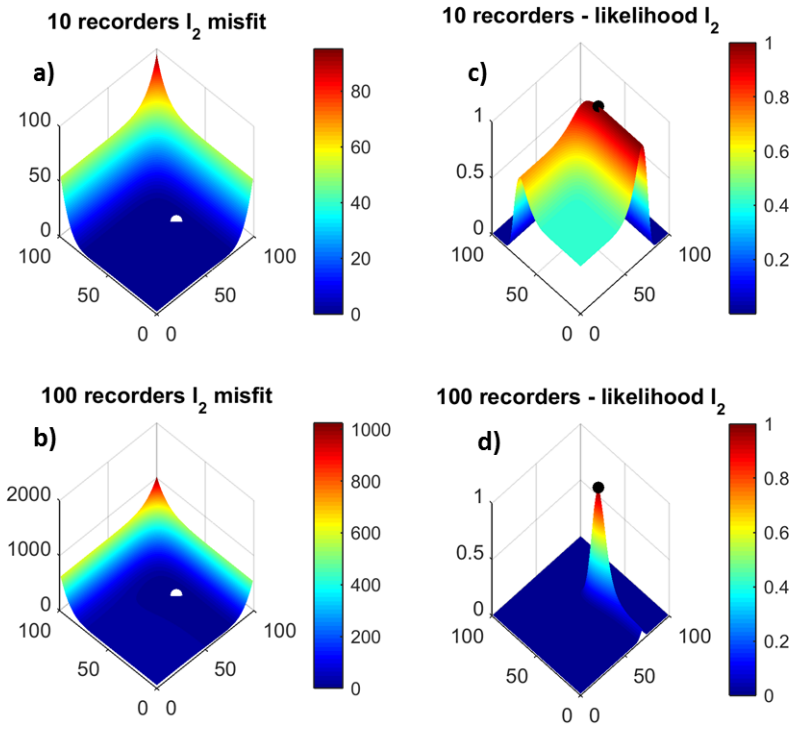

Figure 14: Misfit and likelihood functions for the example problem: x and y axes show the SL of each source, Z axis and color the value of the misfit and likelihood function. Plots a and c show the likelihood and misfit for the 10 recorder scenario, plots b and d for the 100 recorder scenario. The white and black dots represent the minimum and maximum of the misfit and likelihood function. It is located at the true values of the parameters (true source levels).

The misfit functions show little optically discernible difference between the 10 and 100 recorder scenario. The likelihood functions however, show a more pronounced peak at the true source level values when 100 instead of 10 recorders are used. For both the 10 and 100 recorder scenario, the maximum of the likelihood function can be correctly identified. Using 10 instead of 100 recorders, adds regions of quasi-constant likelihood to the likelihood function. For this example problem, having a smaller number of observations d reduces the gradients of the likelihood functions. This will render it difficult to find the maximum of the likelihood functions with gradient based methods. The effect of forward model uncertainty on the likelihood function is shown in figure 15. It can be seen that the peak of the likelihood function becomes broader with increasing forward model uncertainty. However, the maximum of the likelihood function stays identifiable up to 20 db forward model standard deviation.

Since the example problem had only two parameters, we could easily calculate the misfit and likelihood values for each parameter combination (100^2 combinations). This will become impossible for inverse problems with many parameters. Unfortunately most real world inverse problems include hundreds of parameters. Instead of calculating the

likelihood of all parameter combinations one can resort to finding the maximum of the likelihood function using numerical techniques. The next section describes these techniques.

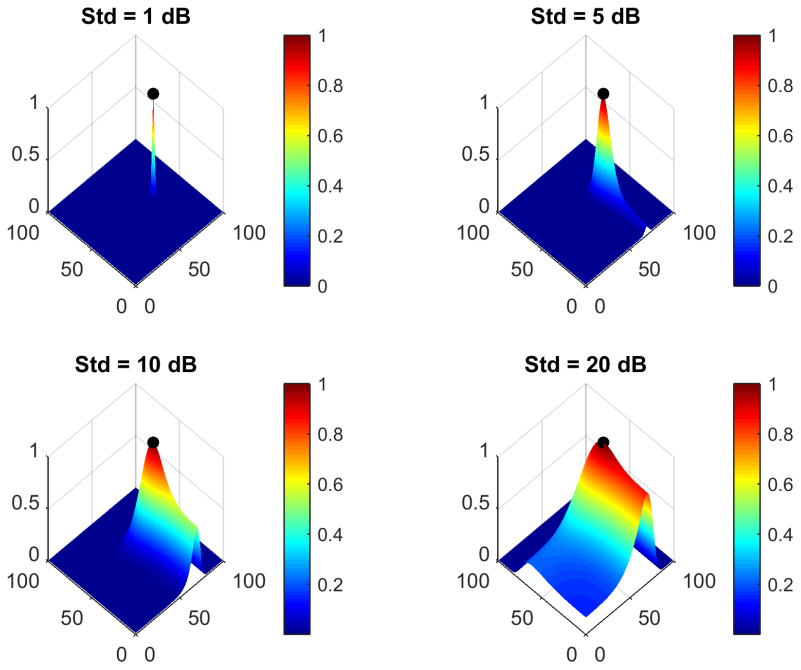

Figure 15: Comparison of likelihood function using 100 recorders, the l_2 norm and different forward model uncertainties: x and y axes show SL of each recorder, z axis and color the value of the likelihood function. Black points mark the true parameters and maximum of likelihood function.

4.3. Monte Carlo Markov chains

A useful method of finding the maximum of the posterior distribution $\sigma(\boldsymbol{m})$, when the parameter space has many dimensions, are Monte Carlo Markov chains (Metropolis et al., 1953). The term Monte Carlo stands for the technique of describing a probability distribution with a set of discrete samples (Mosegaard and Sambridge, 2002), whereas Markov chains describe a process where a transition from one state to another can be defined with a probability (Tarantola, 2004). In the context of Bayesian inversion, this means that a set of forward model parameter samples are drawn from the prior probability distribution $\rho(\boldsymbol{m})$. Each of these samples is a parameter vector $\boldsymbol{m}$ (a solution of the inverse problem). The samples are moved iteratively across parameter space to find the parameter values with maximum likelihood. For each iteration, the parameters are randomly altered. The change is accepted if it increases the likelihood of the solution, otherwise it is neglected and a new random change is produced. The consequent movement of the Monte Carlo Markov chain (MCMC) through parameter space, is commonly termed a random walk (Mosegaard and Sambridge, 2002). When the likelihood function has only one maximum (similar to the 2 parameter example), the MCMC will find it after a sufficient number of

iterations. Figure 16 displays an example random walk across the parameter space of the two parameter example problem.

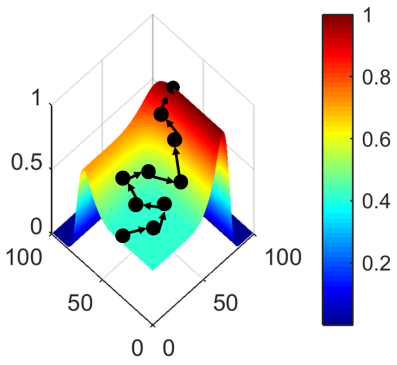

Figure 16: Monte Carlo Markov chain performing a random walk through the parameter space of the example problem from section 4.2: x and y axis represent the two parameter space dimensions, z axis and color the value of the likelihood function. Black dots show the location of the Monte Carlo Markov chain at each iteration and arrows indicate the direction of its movement.

With the Monte Carlo Markov chain method it is possible to find the maximum of a function with hundreds of dimensions. However, many functions have more than one maximum. One can then distinguish between the global maximum and other local maxima (Mosegaard and Sambridge, 2002). To find the maximum likelihood point, we need to identify the global maximum of the likelihood function. The key to finding the global maximum is to determine which moves of the MCMC are accepted and which are rejected. This is not a trivial task: If one only accepts increases in likelihood (better solutions) and neglects all moves that lead to a likelihood decrease (worse solutions), the MCMC will get "stuck" at a local maximum.

A commonly used acceptance rule is given by the Metropolis-Hastings algorithm: it always allows increases in likelihood, and randomly accepts moves that decrease the likelihood (Metropolis et al., 1953). This results in a constant movement of the MCMC through parameter space and prohibits the MCMC from getting stuck at local maxima. After a sufficient number of iterations the MCMC will converge towards the global maximum. However, when an inverse problem is extremely under-determined, the likelihood function can have large regions of almost equal likelihood as well as many local maxima. This renders it difficult to find global maximum using the Metropolis-Hastings algorithm (Mosegaard and Vestergaard, 1991). For these inverse problems, an algorithm termed "simulated annealing" describes a useful acceptance rule.

The term annealing stems from metallurgy and describes the gradual cooling of a metal, which results in metals with small grain size and high ductility (Kirkpatrick et al., 1982). In the context of Monte Carlo Markov chains, simulated annealing is a modification of the Metropolis-Hastings algorithm (Kirkpatrick et al., 1982). In this case, the temperature is used to determine the acceptance of moves that decrease the likelihood.

Similar to metallurgic annealing, the temperature is reduced exponentially over the iterations (time). In the beginning of the algorithm's run-time, the MCMC will move randomly through parameter space. However, over the iterations the acceptance rule is altered, and will eventually only accept moves that increase the likelihood. Analogous to the cooling of metal, the variable controlling the acceptance rule is termed the temperature. It has been shown by Granville et al. (1994) that this algorithm will converge to the global maximum within a finite amount of time. For the extremely under-determined inverse problems found in geophysics, parameter estimation with simulated annealing is widely used (Mosegaard and Vestergaard, 1991).

5. Methods

This section will initially describe how to measure the fin whale chorus received level, and then explain the inversion method used to estimate fin whale distribution from these measurements.

5.1. Measuring chorus received level

5.1.1. Processing of spectral averages

The major part of a recorded underwater sound signal is noise (Lurton, 2002, Carey and Evans, 2011). This means, that the ambient noise spectrum can be calculated as power spectral density (PSD) of a recording (Duennebier et al., 2012). The power spectral density describes how the power of a signal is distributed over frequency. Basically, it can be expressed as the squared Fourier transformation of a time series, divided by the time series length (Smith, 2003). Multiple methods exists to calculate the PSD, but Welch's method (Welch, 1967) is the most used (Smith, 2003). It divides a time series into a subset of overlapping sections (Hamming windows) and then averages their squared Fourier transformations. All power spectra presented in this thesis have been calculated with this method.

In the literature, the strength of the fin whale chorus is often described with a measure termed the fin index (Nieukirk et al., 2012, Klinck and Nieukirk, 2012, Simon et al., 2010). Nieukirk et al. (2012) defines the fin index as the sum of the normalized PSD between $f_{min} = 19.0$ Hz and $f_{max} = 22.0$ Hz:

$$Fin\ index(t) = \sum_{f_{min}}^{f_{max}} PSD(t,f) - PSD_{median}(t) \tag{15}$$

Here PSD_{median} describes the median PSD between 0 and 55 Hz (Nieukirk et al., 2012). The sound pressure described by the fin index contains energy both from the fin whale chorus and other noise sources. This renders it unsuitable for an inversion. Instead, a different method is proposed to calculate the received level of the fin whale chorus. It is based on Parsevals relation (Eq. 16, Smith (2003)). This relation states that the energy of a signal in the time domain ($x(t)$) equals its energy in the frequency domain ($X(t)$).

$$\int_{-\infty}^{\infty} |x(t)|^2 dt = \int_{-\infty}^{\infty} |X(f)|^2 df \tag{16}$$

Every underwater sound recording will contain energy from biotic, abiotic and anthropogenic sources. In the time domain we cannot differentiate between these noise sources. However, in the frequency domain we can utilize the fact that marine mammal choruses are usually confined to a narrow frequency band. From Parcevals relation, we can derive the recorded sound pressure for a given frequency band as:

$$p_{recorded} = \sqrt{\int_{f_{min}}^{f_{max}} FFT_{recorded}(f) df} \tag{17}$$

Here FFT stands for the Fourier transformation of the sound pressure signal. For the discrete values of the PSD, the integral can be written as sum over the desired frequency band:

$$p_{recorded} = \sqrt{\sum_{i=f_{min}}^{f_{max}-f_{min}} PSD_{recorded}(f)} \tag{18}$$

To now calculate the chorus sound pressure, we need to subtract the abiotic sound pressure from the recorded sound pressure. It can be interpolated from the PSD of frequency bands slightly below and above the chorus frequency band. In this thesis it was interpolated with an 8th degree polynomial from the recorded spectrum (excluding the fin whale chorus band between 15 and 25 Hz). Figure 17 shows an example ambient noise spectrum with distinct fin whale chorus peak. The interpolated abiotic PSD is displayed in red.

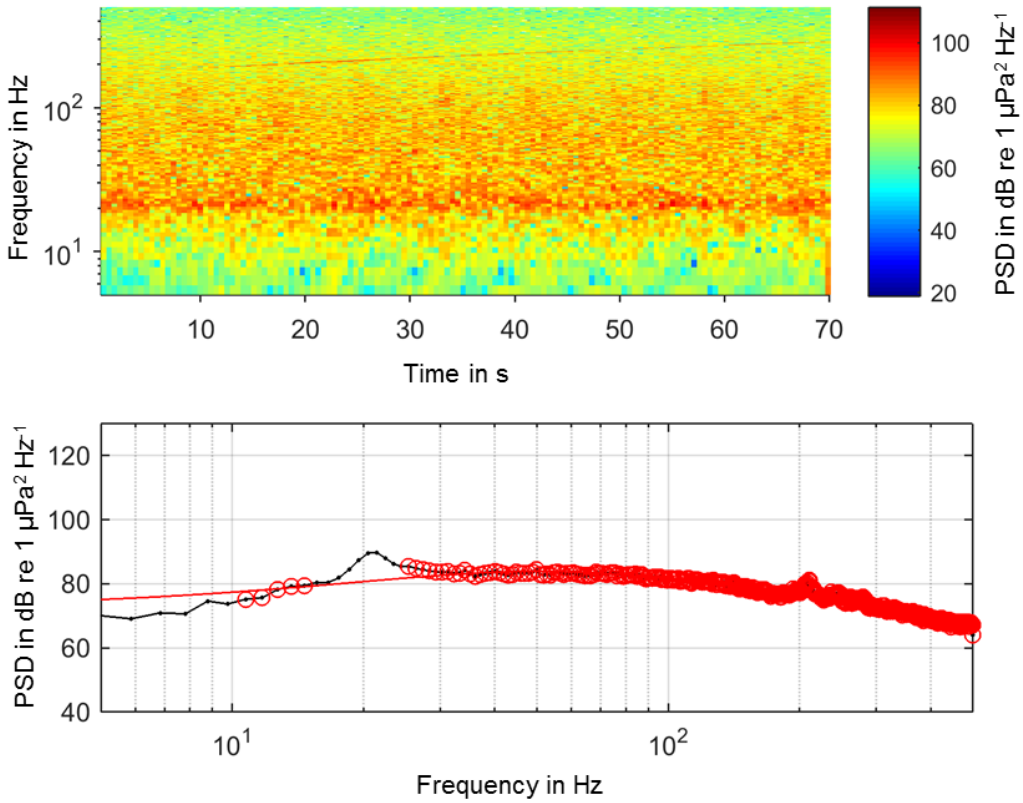

Figure 17: Spectrogram and ambient noise spectrum of a recording taken on the 3.10.2008 in Fram strait. Fin whale chorus is visible as a red band at 20 Hz in the spectrogram (upper panel). In the ambient noise spectrum, the fin whale chorus is visible as a peak at 20 Hz (lower panel). Here the black line represents the recorded spectrum and the red line the interpolated abiotic spectrum.

After determining the abiotic sound pressure, the chorus sound pressure and respective chorus received level can be calculated as follows:

$$p_{chorus} = p_{recorded} - p_{abiotic} \tag{19}$$

$$RL_{chorus} = 20\ log_{10}(p_{chorus}) \tag{20}$$

How much the chorus differs from the abiotic noise is defined by the chorus signal-to-noise ratio (SNR):

$$SNR_{chorus} = 20\ log_{10}(p_{recorded}) - 20\ log_{10}(p_{abiotic}) \tag{21}$$

The chorus signal-to-noise ratio gives similar values to the fin index introduced by Nieukirk et al. (2012). Both describe the intensity of the fin whale chorus relative to the abiotic noise. As an example, the next section presents the fin whale chorus recorded by a hydrophone array in Fram strait.

5.1.2. Example recordings from the DAMOCLES array

The DAMOCLES acoustic array was moored in Fram strait (Figure 18) between 2008 and 2009 (Sagen et al., 2010b, Mikhalevsky et al., 2015). DAMOCLES stands for: Developing Arctic Modeling and Observing Capabilities for Long-term Environmental Studies. The array consisted of a sound source that emitted 90 s sweeps between 200 and 300 Hz and a set of 8 hydrophones in a vertical string. The recording unit, the Simple Tomography Acoustic Receiver system (STAR), sampled with 1000 Hz. The recordings were kindly provided by the Nansen Environmental and Remote Sensing Center. The original purpose of the acoustic array was to monitor the mean ocean temperature of Fram strait (Sagen et al., 2008). In this thesis however, the recordings are used to calculate the fin whale chorus received levels.

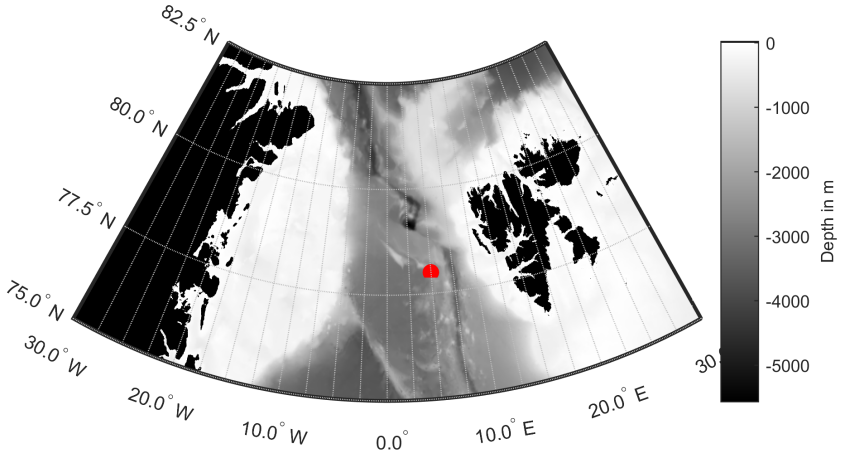

Figure 18: Map showing the location of the DAMCLOES hydrophone array as a red dot.

The STAR unit recorded 100 s snippets every 3 h. However, due to technical problems many recordings were either missing, too short or contained electronic noise. These

recordings were sorted out on the basis of their low pass filtered amplitude (electronic noise had unrealistically high amplitude). In the remaining recordings, visual analysis revealed sparse occurrence of fin whale calls, but reoccurring presence of the fin whale chorus. The ambient noise PSD was calculated from the first 10 s of each recording using Welch's method (Welch, 1967) with a 1 s window length. This results in a frequency resolution of 1 Hz. The consequently obtained ambient noise spectrogram can be seen in figure 19. The fin whale chorus can be seen as a horizontal band at 20 Hz between August and April. In June and July increased noise levels from seismic surveys dominate the spectrum between 10 and 100 Hz. This agrees with the analysis of recordings from Fram strait by Moore et al. (2011) and Klinck and Nieukirk (2012).

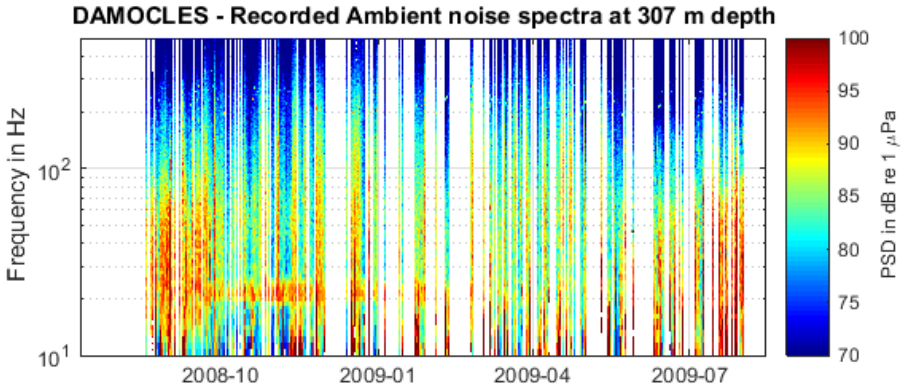

Figure 19: Longterm spectrogram of ambient noise recorded by the DAMOCLES tomography array, PSD of 10 s snippets using Welch's method with 1 s window length, 50 % overlap. Fin whale chorus visible at 20 Hz.

The fin whale index, chorus received level and signal to noise ratio were calculated from the ambient noise spectra as described in the previous section. The results are displayed in figure 20 and indicate that the fin whale chorus is detectable from September to February in the Fram strait. Peak chorus received levels are reached in November. The few fin whale chorus received level observations larger than 100 dB re 1 µPa after December 2008 are likely caused by individual vocalizing whales near the recorder. The fin index shows different patterns than the chorus received level. Upon closer examination, it becomes evident that some patterns in the fin index correspond to an increase in signal to noise ratio. Whilst other patterns correspond to an increase in chorus received level. This demonstrates that the method used to describe a marine mammal chorus, significantly influences the results and interpretation of a study. Variation in signal to noise ratio might explain why the fin index varies strongly between 2 close recorders in the study of Simon et al. (2010).

For the inversion of marine mammal chorus observations, it is necessary to calculate the chorus received level and not the fin index. The fin index obtained from the DAMOCLES array differs from observations by Klinck and Nieukirk (2012). They observed fin index values between 0 and 3. This could either be caused by inter-annual variations, or differences in the way the fin index was calculated.

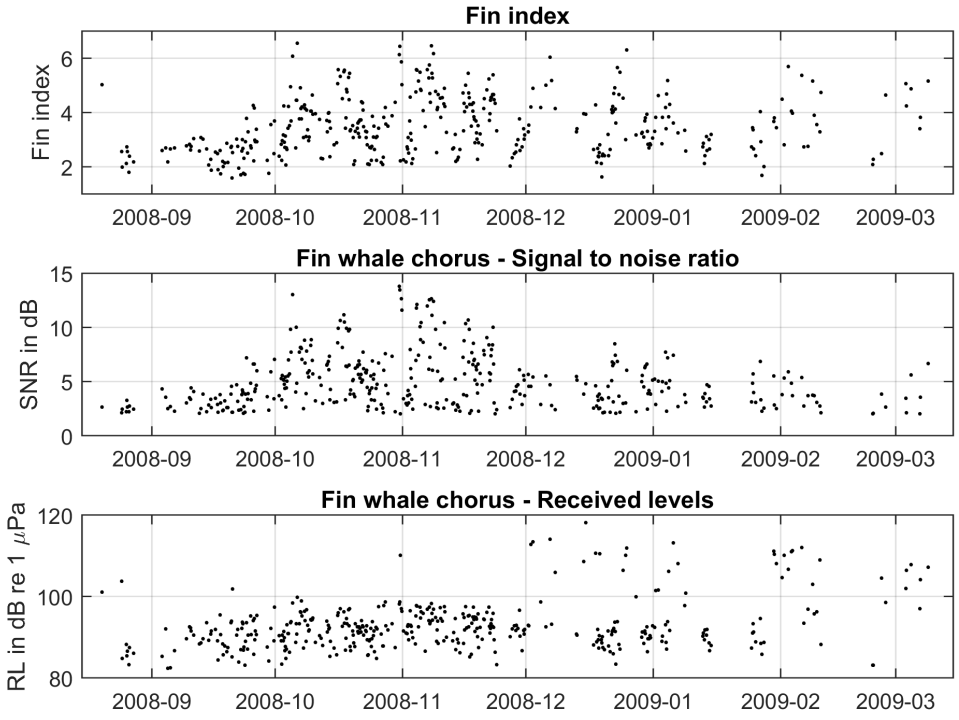

Figure 20: Time series of fin whale chorus recorded by the DAMOCLES array.

5.2. Overview of inversion method

The aim of the inversion method is to find the most likely distribution of vocalizing fin whales, for a given set of chorus received level observations. Therefore we need to describe the unknown whale distribution with a set of parameters $\boldsymbol{m}$. The data $\boldsymbol{d}$ is a vector describing the received levels of the fin whale chorus recorded at different locations: $RL_{observed}$. It could for example be (in dB re 1 µPa):

$$\boldsymbol{d} = RL_{observed} = [93.45,\ 95.34,\ 91.45,\ ...\ 94.28] \tag{22}$$

The inversion method can be divided into two processes: The forward model $g(\boldsymbol{m})$ and the parameter estimation algorithm. Combined they form the inversion algorithm. The flowchart in figure 21 shows the basic structure of the inversion algorithm. All input variables (received level data, a priori information and auxiliary variables) are displayed in yellow. The modules describing the forward model are displayed in blue, whereas the parameter estimation modules are shown in gray and white. The inversion algorithm uses Monte Carlo Markov chains and simulated annealing (introduced in section 4.3) to find the maximum of the posterior distribution ($max(\sigma(\boldsymbol{m}))$). The output of the inversion algorithm is a set of parameters, that are solutions to the inverse problem. The most likely parameters (corresponding to the maximum of the posterior distribution) can be averaged from these solutions. A detailed discussion of the different modules will be given in the following sections.

All code developed for this thesis was written in Matlab 2014b. The source code can be found in the Appendix. Several functions are also available as binaries for Windows and Linux. Due to the high computational effort of the acoustic propagation model and inversions, most computations were run on a Unix cluster owned by the University of Bergen. However all software is also able to run on the 2 cores of a normal consumer computer. Future implementation of the inversion algorithm in C++ or Fortran will likely reduce the computational costs.

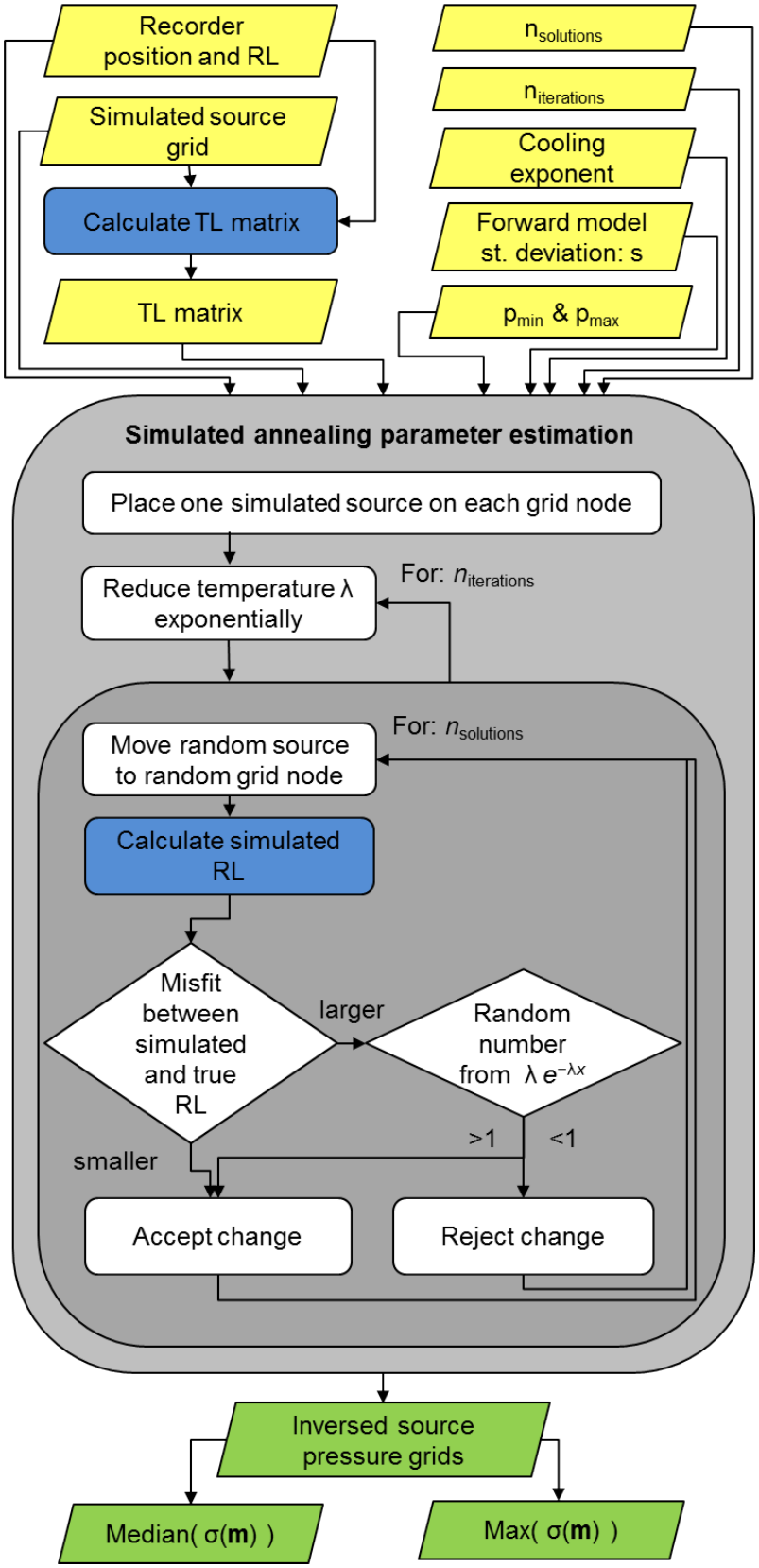

Figure 21: Flow chart showing the basic functionality of the inversion algorithm. Yellow boxes represent input variables, green boxes inversion results, blue boxes the forward model and the gray box the parameter estimation algorithm

5.3. The forward model

The forward model calculates the received level (data $\boldsymbol{d}$) for a given fin whale distribution (parameters $\boldsymbol{m}$):

$$g(\boldsymbol{m}) = RL_{simulated} \tag{23}$$

From the sonar equation (Eq. 4) we know that the received sound pressure level is influenced by a large number of factors. Firstly, the source level and source location have a large influence on the received levels. Secondly, the transmission loss is not only influenced by the source and receiver locations, but also a large number of environmental variables. The most important are the sound speed field, sea floor shape and properties, sea surface roughness, sea ice and bubble clouds. Additionally the RL varies with time. One can hardly include all of these parameters correctly into an efficient forward model. Instead several assumptions are necessary.

The first assumptions concerns time. As will be shown in the following section, we can assume a steady state situation in which the source level and received level are constant over the recorded period. The quasi-continuous nature of the fin whale chorus arises due to the many sources involved, the multi-path propagation that spreads impulsive signals over time, and the monotonous nature of fin whale pulse trains. For simplification, the following sections address vocalizing whales as sound sources.

The second necessary assumption is to discretize the parameter space in which the algorithm searches for likely parameters. It is also termed the search space in literature (Tarantola, 2004). For simplification, the depth of a vocalizing whale is neglected. This is deemed appropriate since the source depth mainly affects transmission loss in the acoustic near field (Weirathmueller et al., 2013). The possible fin whale locations are furthermore reduced to nodes on a geodesic grid (discussed in section 5.3.2) and the possible source levels limited by a minimum and maximum value. Then a TL matrix connecting all possible source and recorder locations is calculated using an arbitrary propagation model.

5.3.1. Substitution of sound sources

In the forward model, we assume a steady state and substitute the impulsively vocalizing whales with continuous sources. Due to multi-path propagation, the initially impulsive signal emitted by a vocalizing fin whale will become a quasi-continuous signal several hundred kilometers away from the source. This process was modeled with the raytracing model BELLHOP for an example scenario involving a fin whale north of Iceland (Porter and Bucker, 1987, Porter and Liu, 1994). Figure 22 shows the source location and the section along which the sound propagation was modeled. The bathymetry was extracted from the ETOPO world topography dataset, and the sound speed from the annual mean world ocean atlas climatology dataset (Amante and Eakins, 2009, Dushaw et al., 2013). The source depth was 25 m and the impulse response was calculated for 50 receivers at 100 m depth along the section. The bathymetry and sound speed along the section as well as source and receiver locations are displayed in figure 23.

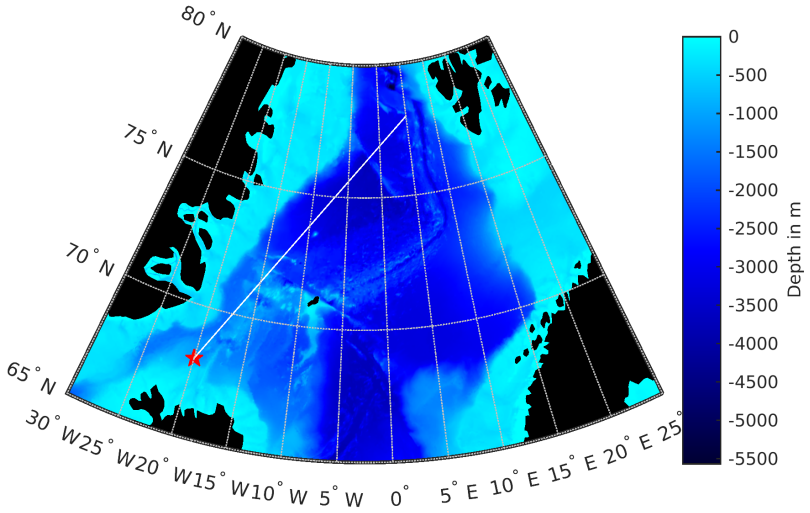

Figure 22: Map of section for which impulse response was modeled, the red star represents the sound source.

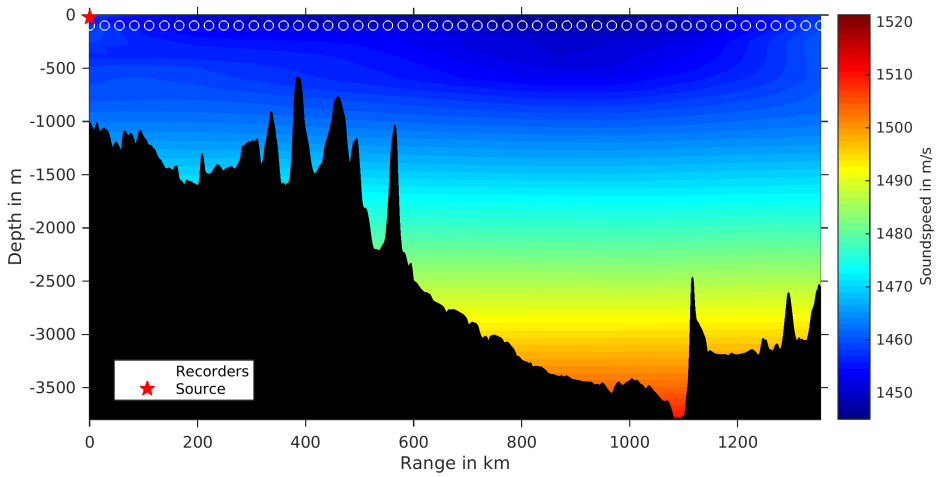

Figure 23: Bathymetry and sound speed of section for which impulse response was modeled. Bathymetry extracted from ETOPO-1 dataset, Sound speed from world ocean atlas mean climatology dataset. Red star represents the location of the sound source and the white circles the receiver locations.

The ray trace underwater sound propagation model BELLHOP (Porter and Liu, 1994) calculates the range depended sound-field using the approach described in section 3.3. It can calculate the impulse response and transmission loss over range and depth. One of its advantages is the possibility to include range dependent bathymetry and sound speed profiles. Ray trace models such as BELLHOP are deemed most accurate above a few hundred Hz (Porter and Bucker, 1987). However, at frequencies lower than 100 Hz they still indicate reliable results for impulsive signals such as fin whale calls (Hovem, 2013, Hovem and Korakas, 2014).

BELLHOP calculates the impulse response for up to 500 arrivals and thus gives a good estimate of the true impulse response. However, due to this limitation, the modeled impulse response does not resolve the long tail of low amplitude echoes very well. Figure 24 shows the arrival time and transmission loss of each eigenray (arrival) over the range. It can be seen that the impulse response spreads out over more than 12 s already 100 km away from the sound source. As the signal passes a set of sea mounts at a range of 400 km, many eigenrays are filtered out. At more distant ranges, most eigenrays have a very low amplitude, with two strong eigenrays visible at ranges larger than 800 km.

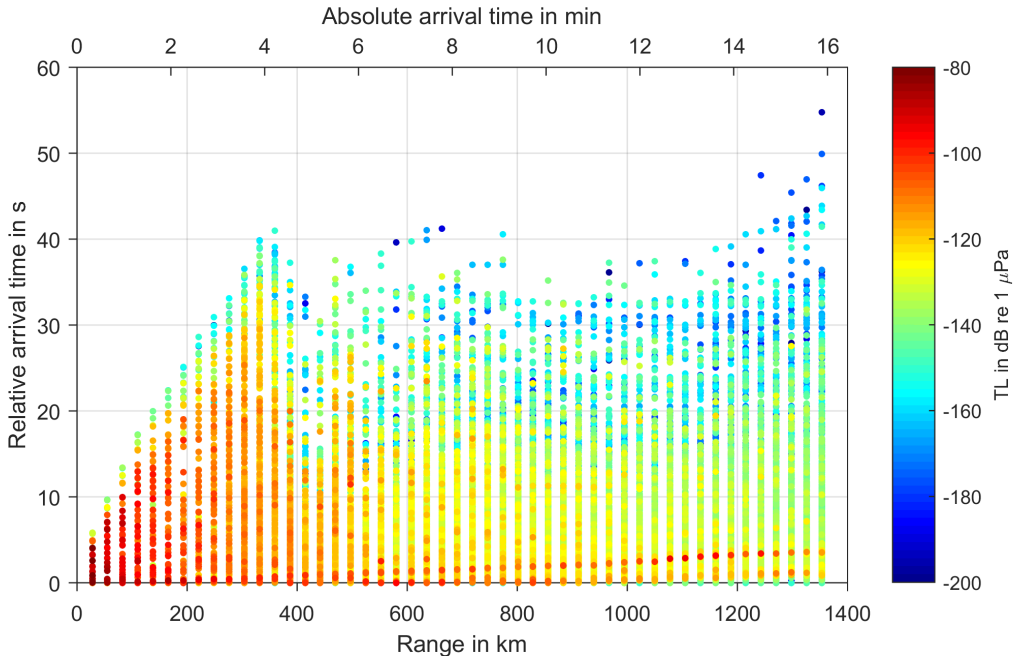

Figure 24: Plot of impulse response over range and time. Each dot represents the arrival of an eigenray, the x axis represents range and absolute arrival time and the y axis the relative arrival time. The relative arrival time was calculated by subtracting the time of the first arrival at each receiver, from the respective absolute arrival time. Note that the model was limited to 500 arrivals at every receiver due to numerical reasons. In reality the impulse response will have a longer tail of low amplitude arrivals.

If we convolute the impulse responses with a fin whale pulse train that has 12 s inter pulse intervals, we obtain a good estimate of how the pulse trains energy spreads out over time (Figure 25). The initial fin whale call is 1 s long, but due to many echoes, it will be about 10 s long once it has propagated 50 km away from the source. Over 100 kilometers away from the source, the sound pressure of one fin whale call arrives over a period of 15 s or more, overlapping with the other calls in the pulse train. The pulse train thus becomes a quasi-continuous signal. Between 400 and 1000 kilometers the pulse-like nature of the signal becomes apparent again, likely caused by blocking of eigenrays from the seamounts at a range of 400 km. Considering all vocalizing fin whales, it becomes evident that the combined fin whale pulse trains will form a continuous signal:

The fin whale chorus. We could demonstrate that fin whale pulse trains become a quasi-continuous signal at several hundred km away from the whale. Furthermore it has been observed that pulse trains commonly last between 1 and 32 hours (Watkins et al., 1987). To simplify the forward model, we can thus substitute the impulsively vocalizing whales with a set of continuous sources at the same frequency.

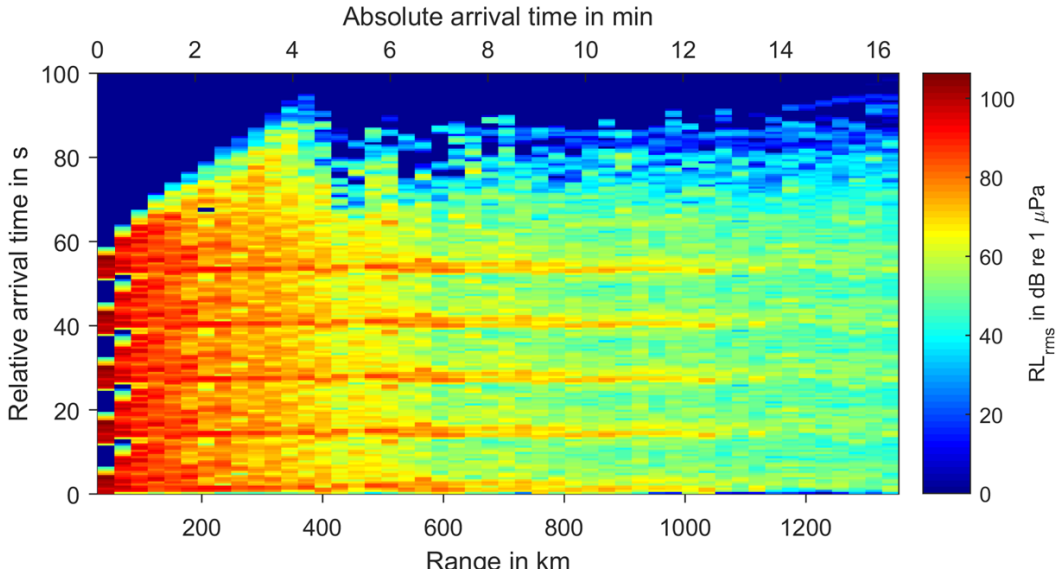

Figure 25: Convolution of fin whale pulse train (5 pulses and 12 s intervals) with modeled impulse response. X axis represents range and absolute arrival time and the y axis the relative arrival time (the time of first arrival at each receiver subtracted from the absolute arrival time) Color represents the received level.

5.3.2. Geodesic source grid

The two previous sections demonstrated that we can neglect the dimensions of time and depth in the forward model. This means that the forward model parameters m only need to describe the distribution of vocalizing whales over latitude and longitude. The whales are replaced with a set of sound sources. We assume that these sound sources emit continuous signals at the frequency of 20 Hz. The sound sources can not be allowed to take arbitrary positions, since this would require an extreme computational effort. Instead the possible locations of the sound sources are reduced to nodes on a grid. This grid is termed the simulated source grid.

Using a rectangular latitude-longitude grid will result in uneven distribution of grid nodes across ocean basin scales. Even distribution of grid nodes across these scales can be achieved using a geodesic grid. Teanby (2006) described an algorithm to develop such grids based on approximating the shape of a sphere using an icosahedron. It is available as Matlab code and was implemented into the forward model. Figure 26 shows the location of the grid nodes for 3 resolution steps in the North Atlantic.

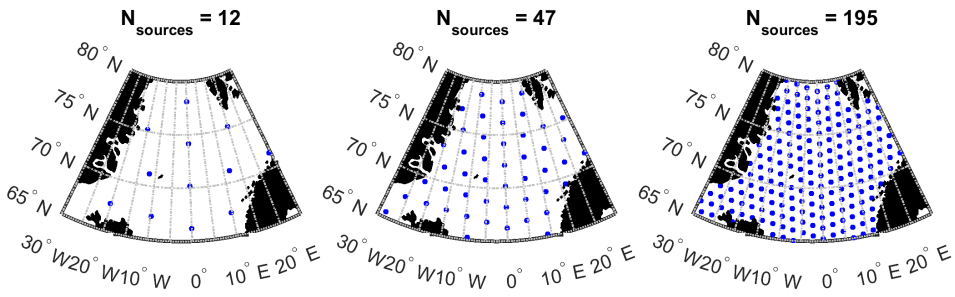

Figure 26: Position of simulated source grid nodes for 3 resolution steps are displayed as blue dots. Geodesic grid nodes span a regular icosahedron around the earth based on Teanby (2006).

After discretizing the search space, there are many ways to formulate the forward problem. A first approach was to place one source on each grid node and allow each to take one of 10 preset sound pressure levels. However, the parameter estimation algorithm could not find the maximum likelihood parameters. There were too many degrees of freedom in the system to find the global maximum of the likelihood function within realizable computation time. It was necessary to find a way to reduce the degrees of freedom and render suboptimal solutions less attractive for the parameter estimation algorithm.

After experimenting with different formulations of the forward model and different parameter estimation algorithms, an efficient formulation of the inverse problem was found. Instead of searching directly for the sound pressure value of each grid node, a fixed number of simulated sources is moved across the grid nodes. This has the effect of reducing the number of possible combinations to $n_{nodes}^{n_{simulated\ sources}}$ (in the benchmark scenario it is 195^{195}). The number of simulated sources is the same as the number of grid nodes, to allow all source location combinations. These range from one simulated source at each node to all simulated sources being at one node.

$$n_{simulated\ sources} = n_{nodes} \tag{24}$$

The parameter vector $\boldsymbol{m}$ is then a vector containing the node index describing where each simulated source is located. If there is one simulated source on each node, the parameter vector will have the following values:

$$\boldsymbol{m} = [1, 2, 3, ... \, n_{nodes}] \tag{25}$$

This can be interpreted as: "Source one is located at node one, source two located at node node two,..." until "source $n_{simulated\ sources}$ is located at node n_{nodes}". To further reduce the degrees of freedom, the total sound pressure of all simulated sources is fixed to the value p_{total}. Each simulated source is then assigned the same sound pressure, based on equation 26.

$$p_{source} = \frac{p_{total}}{n_{simulated\ sources}} \tag{26}$$

Since the true p_{total} is usually unknown, we assume it is somewhere between a minimum and maximum value p_{min} and p_{max}. The minimum and maximum total pressure are part of the a priori probability distribution $\rho(\boldsymbol{m})$. Appropriate values for p_{min} and p_{max} can be obtained from published values on fin whale acoustics.

The source level of each node is determined by the number of simulated sources positioned at it:

$$n_{sources\ on\ node}(i_{node}) = \sum(i_{node} \in \boldsymbol{m}) \tag{27}$$

Here i_{node} describes the index of each node. The source pressure and source level of each node are determined by the following equations:

$$p(i_{node}) = n_{sources\ on\ node}(i_{node})\ p_{source} \tag{28}$$

$$SL(i_{node}) = 20\ log_{10}(p(i_{node})) \tag{29}$$

The source pressure at each grid node describes, where on the grid sound energy is emitted and how much. It is an approximation of the distribution of vocalizing fin whales. In regions where the grid nodes have non-zero sound pressure values, vocalizing fin whales must be present. In regions where the grid nodes have zeros as sound pressure values, no vocalizing fin whales are present. Nodes with high source pressure indicate increased fin whale calling activity, compared to nodes with low source pressure. However, increased calling activity does not automatically imply an increased whale abundance. Increased calling activity could either be caused by an increasing number of vocalizing whales or an increase in the whales source levels and call rates.

Compared to the simulated sources (that are confined to take positions on a geodesic grid) the recorders can take any position within the ocean. According to the sonar equation (Eq. 4), the simulated received levels depend on the transmission loss between the grid node and recorder locations. For a given set of recorders, equation 30 determines the simulated received levels:

$$RL_{simulated}(i_{recoder}) = \sum_{i_{node}=1}^{n_{nodes}} SL(i_{node}) - TL(i_{node}, i_{recoder}) \tag{30}$$

This is a simplified version of the sonar equation, RL stands for received level, SL for source level and TL for transmission loss. The indices i_{node} and $i_{recoder}$ describe the respective elements of the source grid and recorder array. The transmission loss can be determined using an arbitrary sound propagation model, as long as the TL can be given as a matrix connecting each node and recorder. Two ways of calculating the TL matrix were tested in this thesis: Geometrical spreading and ray trace modeling using BELLHOP. They will be described in the next section.

5.3.3. Transmission loss matrix

The transmission loss between each node and all recorders can be expressed as a matrix. Equation 31 gives an example TL matrix:

$$TL = \begin{array}{c} \\ node_1 \\ node_2 \\ ... \\ node_{n_{nodes}} \end{array} \begin{array}{c} \begin{array}{ccccc} recorder_1 & recorder_2 & recorder_3 & ... & recorder_{n_{recorders}} \end{array} \\ \begin{pmatrix} -65.364 & -66.289 & -70.345 & ... & -120.321 \\ -87.343 & -78.342 & -85.743 & ... & -97.954 \\ ... & ... & ... & ... & ... \\ -34.454 & -50.432 & -63.552 & ... & -98.112 \end{pmatrix} \end{array} \tag{31}$$

In this thesis the TL matrix was calculated in two ways. In general, one could use any acoustic propagation model for this. For the sake of simplicity and reduced computational effort, the cylindrical spreading model from equation 7 and the raytracing model BELLHOP (Porter and Bucker, 1987) were used. The TL matrix was estimated for signals at 20 Hz.

The cylindrical transmission loss matrix was calculated using equation 7 with a $r_{critical}$ of 4000 m. The critical range was set to 4000 m since this represents the average ocean depth. The absorption coefficient α was calculated using the empirical equations from Francois and Garrison (1982) (Figure 8).

The raytracing transmission loss matrix was calculated using the two dimensional, range dependent sound propagation model BELLHOP (it is described in section 5.3.1). It calculates the TL for 2D "slices" (range and depth). The bathymetry for each slice was obtained from the ETOPO-1 topography and bathymetry dataset (Amante and Eakins, 2009). The sound speed over range and depth for each slice was interpolated from the world ocean atlas mean annual climatology dataset (Dushaw et al., 2013). The sea floor was simply assumed as elasto-acoustic half-space with a pressure wave sound speed of $1800\,ms^{-1}$ and an attenuation of $0.1\,\mathrm{dB}\,\lambda^{-1}$ and a density of $2.0\,g\,cm^{-3}$. BELLHOP includes the source and recorder depths into its TL estimates. Each sound source was assumed to be at 50 m depth and all recorders assumed to be at 100 m depth.

The 2 methods of estimating transmission loss were compared along the section between Iceland and Svalbard (Section 5.3.1). Figure 27 shows the estimated TL over range. It shows that geometrical spreading overestimates the TL in the first 500 km compared to BELLHOP, and agrees with the latter for ranges larger than 500 km from the source. However this will vary with the bottom topography and sound speed field between source and receiver. In general, geometrical spreading and raytracing provide a roughly similar logarithmic TL curve.

To estimate the 3-D sound field, the 2-D sound fields "slices" BELLHOP creates, can be rotated around the source. This approach is also termed 2xN dimensional modeling. In this thesis, the transmission loss was estimated for 72 slices along 5° intervals around the source (covering the entire 360° around the source). From the 72 BELLHOP slices, a latitude-longitude grid containing the transmission loss at 100 m depth for each location was interpolated. The transmission loss at each recorder location was obtained from the latitude-longitude grid. To obtain a complete TL matrix connecting all nodes and

recorders, this methods was applied to every node in the simulated source grid. Figure 28 displays an example of the TL slices calculated by BELLHOP, the interpolated latitude-longitude grid and TL at the recorder locations.

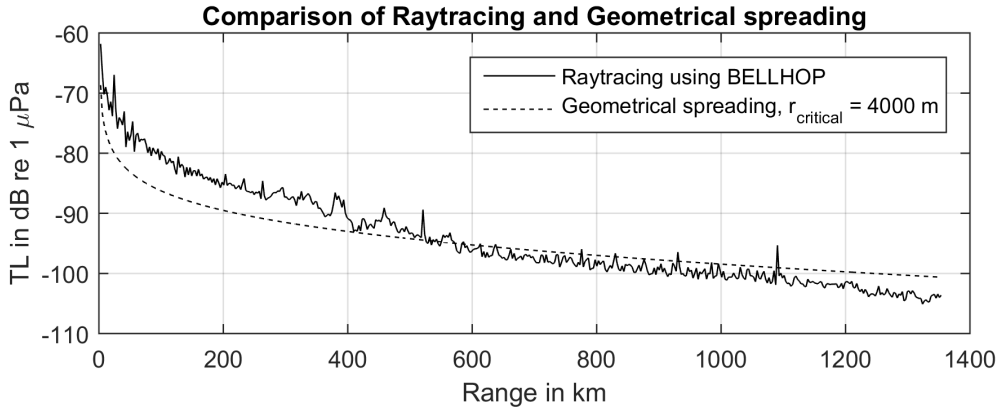

Figure 27: Comparison of transmission loss estimates at 100 m depth for the example transect from section 5.3.1.

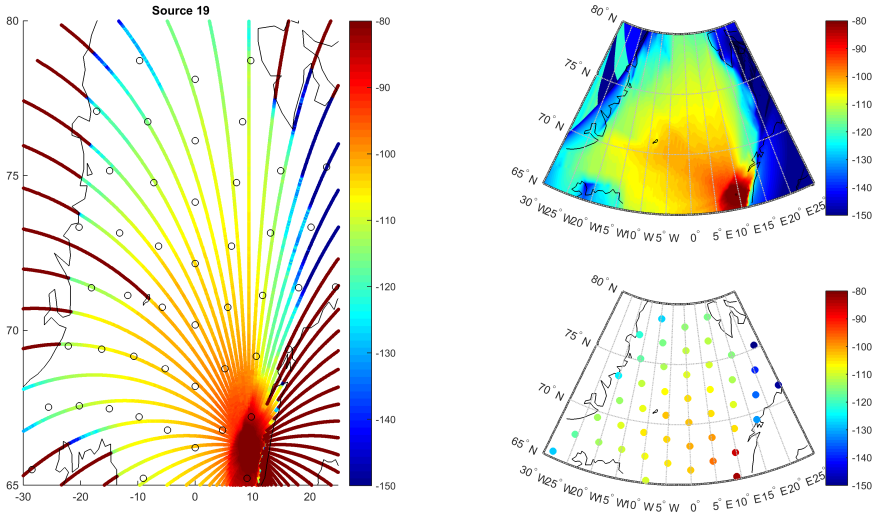

Figure 28: Example of 2xN dimensional raytracing for calculating the transmission loss (TL) matrix. Left plot shows TL of slices calculated with BELLHOP. Upper right plot shows a map of interpolated latitude-longitude grid and the lower right plot the TL at the recorder locations.

5.4. Parameter estimation using simulated annealing

The previous section established a forward model $g(\boldsymbol{m})$, that determines how the parameters $\boldsymbol{m}$ (describing the distribution of vocalizing fin whales) generate the chorus received level data $\boldsymbol{d}$. This section describes the parameter estimation algorithm used to determine the most likely parameters $\boldsymbol{m}$ given the data $\boldsymbol{d}$.

The parameter vector describes the position of simulated sources on a grid covering the ocean (in latitude and longitude). Depending on the resolution of the grid, there are hundreds of parameters to estimate. A benchmark scenario presented further in the text uses 195 grid nodes. This means there are 195 parameters, resulting in 195^{195} possible combinations. It is thus impossible to calculate the likelihood of all possible combinations. Instead Monte Carlo Markov chains (Section 4.3) are used to find the maximum of the likelihood function in parameter space. In the case of the benchmark scenario, the parameter space has 195 dimensions, one for each entry of the parameter vector $\boldsymbol{m}$. Compared to the large number of parameters, the number of RL observations is very small (below 50). This means that the inverse problem is extremely under-determined and the likelihood function will have many local maxima. The many local maxima and dimensions render it difficult to find the global maximum for the Monte Carlo Markov chains.

The first challenge is to define how the Monte Carlo Markov chains move though parameter space. This is displayed in figure 29. Initially one simulated source is located on each grid node. Then, for each iteration, a simulated source is chosen randomly and moved to a random new grid node. If a move is accepted or rejected, is determined by an acceptance rule that will be discussed later in this section. After the decision, a new random move is generated. In this fashion the MCMC moves through the parameter space until a it has carried out a fixed number of iterations.

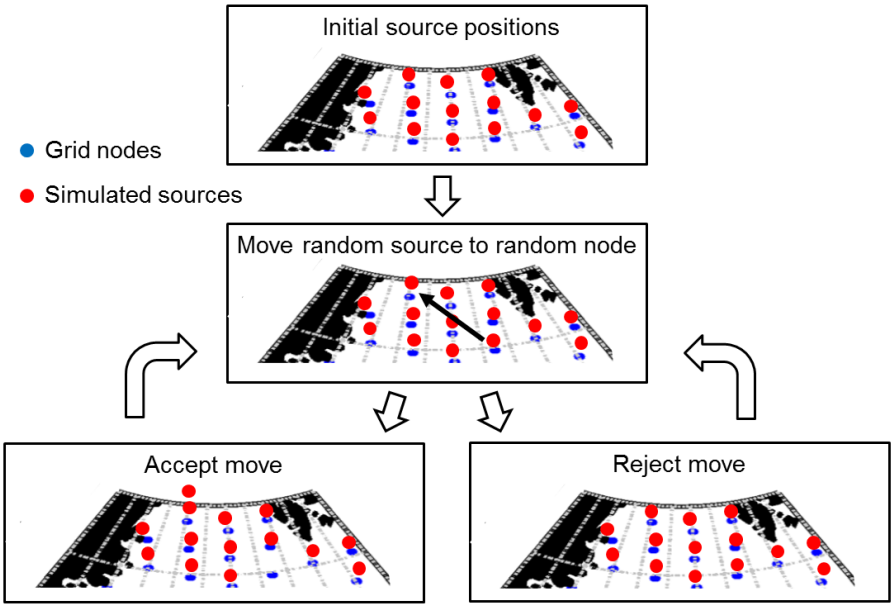

Figure 29: Movement of simulated sources across the grid nodes.

The development of a suitable acceptance rule proved to be the most challenging part of this thesis. After unsuccessful trials with the Metropolis-Hastings algorithm (Metropolis et al., 1953) and Ant Colony optimization (Dorigo et al., 2006), a suitable acceptance rule was found using simulated annealing (Kirkpatrick et al., 1982). A move is always accepted if it increases the likelihood $L(\boldsymbol{m})$ of the parameters $\boldsymbol{m}$. The likelihood was calculated after equation 11, using the l_2 misfit between the observed and simulated RL (given by equation 13). However, to prevent the MCMC from getting stuck at local maxima, sometimes moves that decrease the likelihood ("wrong moves") need to be accepted. The likelihood to accept a wrong move is determined with the exponential probability distribution $P(\lambda, x)$:

$$P(\lambda, x) = \frac{1}{\lambda} e^{-\frac{x}{\lambda}} \tag{32}$$

Here λ is termed the temperature and x describes a range of values from 0 to ∞. A wrong move is accepted when a random number x, drawn from $P(\lambda, x)$ is larger than 1. The mean x drawn from $P(\lambda, x)$ equals λ. For each iteration a new random number is drawn from $P(\lambda, x)$. Furthermore, for each iteration the temperature λ is reduced following an exponential function. This will render it less and less likely to accept wrong moves for each iteration. The function used to "cool" the temperature λ is defined as follows:

$$\lambda = (1 - \frac{i_{iteration}}{n_{iterations}})^{\varepsilon} \tag{33}$$

Here ε is defined as the cooling exponent, $i_{iteration}$ the number of the iteration and $n_{iterations}$ the total number of iterations. The cooling exponent determines how fast the temperature λ drops over the iterations. To visualize this concept, figure 30 shows λ and $P(\lambda, x)$ over 10000 iterations, with a cooling exponent ε of 5. Given a sufficient amount of iterations, the simulated annealing algorithm will converge towards the global maximum of the likelihood function (Granville et al., 1994). To illustrate this process, figure 31 shows snapshots of how the source pressure grid is changing during simulated annealing (using 10000 iterations). Initially, the source pressure is distributed evenly. But as simulated sources are moved across the grid nodes, the simulated source pressure grid increasingly resembles the true source pressure grid.

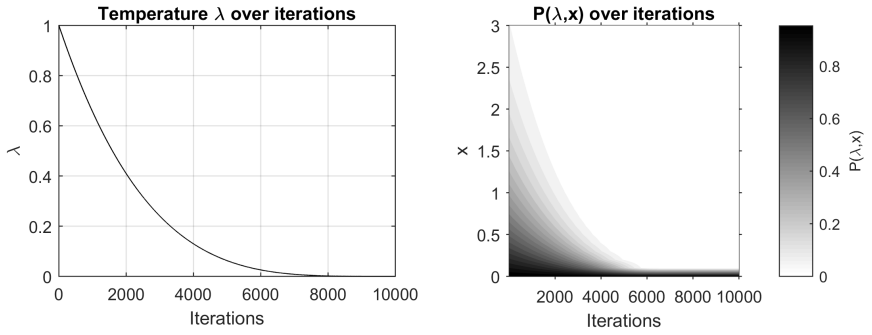

Figure 30: Simulated annealing example plot. Left panel shows how the temperature λ is reduced exponentially over 10000 iterations using a cooling exponent of 5. Right panel shows the resulting probability distribution $P(\lambda, x)$ for each iteration.

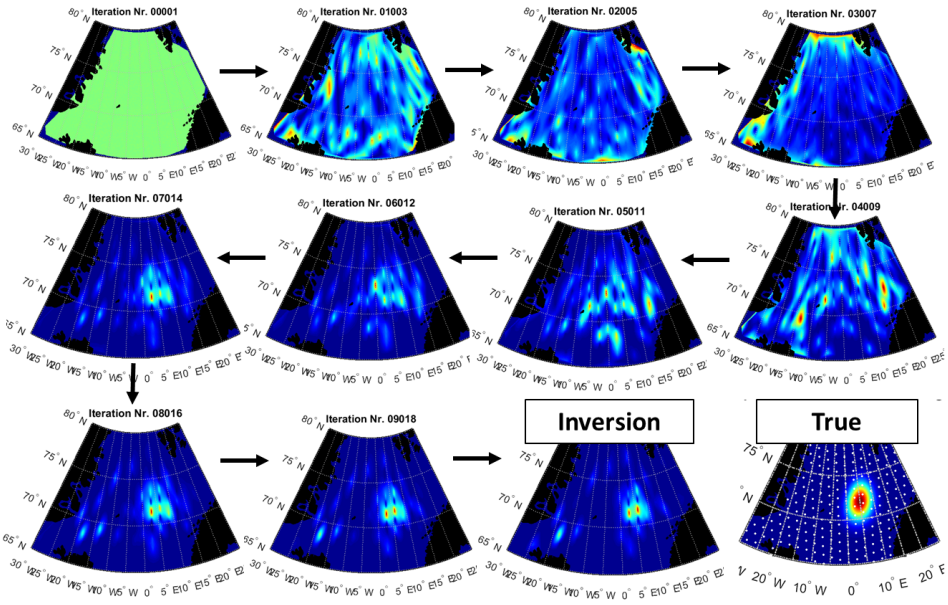

Figure 31: Schematic view of source pressure grid change during simulated annealing. Color surface represents source pressure in µPa. Lower right plot shows true source pressure grid in µPa. The inversion algorithm ran with 10000 iterations, $\varepsilon = 5$ and 195 simulated sources.

After the last iteration, the simulated parameters are a useful estimate of the "true" parameters. However, the most likely parameters are estimated even better, when more than one MCMC is used to estimate it. This increases the likelihood of finding the maximum of the likelihood function and filters out small artifacts (as in figure 31). The parameters the Monte Carlo Markov chains take after simulated annealing, are solutions of the inverse problem. The number of solutions (number of MCMCs) used by the inversion algorithm is determined by the variable $n_{solutions}$. Each solution represents a sample of the posterior distribution $\sigma(\boldsymbol{m})$. How the maximum likelihood parameters can be estimated from the solutions will be discussed in the next section.

In addition to finding the most likely locations the simulated sources have on the source grid, the parameter estimation algorithm needs to find the most likely total source pressure p_{total}. It is located somewhere between a known minimum p_{min} and maximum value p_{max}. To find it, the solutions are assigned different total source pressure values, that are evenly distributed between p_{min} and p_{max}. The more solutions are generated, the better the source pressure grid and p_{total} can be estimated. Since each MCMC moves through parameter space independently, the solutions will have different likelihoods. Figure 32 shows how the misfit and likelihood of the different Monte Carlo Markov chains changes over the iterations. Before the inversion algorithm starts, on the left side of figure 32, the misfit for each solution is high and the likelihood low. But after simulated annealing, on the right side of 32, the solutions show a smaller misfit and increased likelihood. It can also be seen, how the simulated annealing allows decreases in likelihood in the first 2000 iterations.

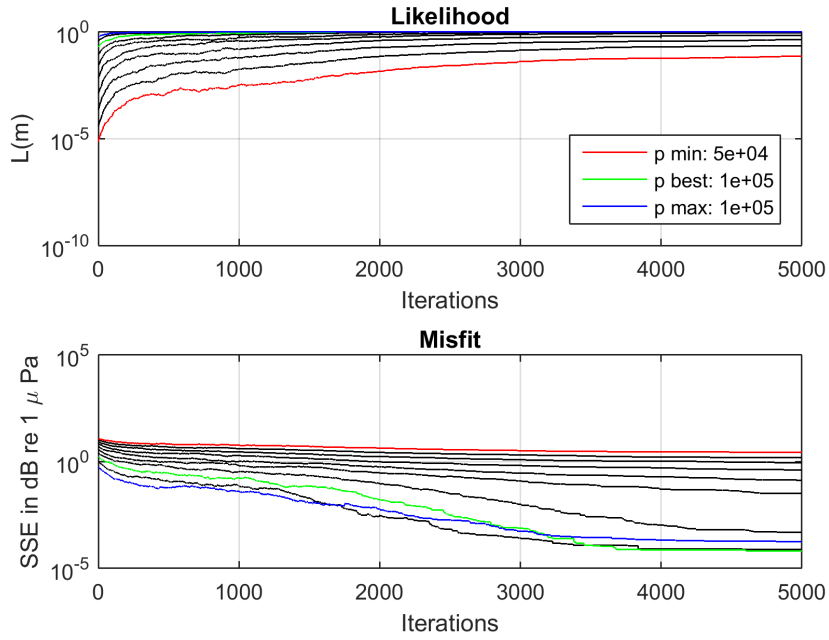

Figure 32: Misfit and likelihood over iterations, each line represents a Monte Carlo Markov chain moving through parameter space. Y axis on both plots has a logarithmic scale. The legend shows the color and value of the solutions with p_{min} and p_{max} as well as the solution with the highest likelihood p_{best}.

The complete parameter estimation algorithm that produces a set of solutions (samples of $\sigma(\boldsymbol{m})$) can be expressed as follows:

for $n_{iterations}$ **do**
  $\lambda = (1 - \frac{i_{iteration}}{n_{iterations}})^{\varepsilon}$
  for $n_{solutions}$ **do**
    Move random source to random node $\rightarrow \boldsymbol{m}_{new}$
    Calculate RL_{new} and determine likelihood $L(\boldsymbol{m})_{new}$
    if $L(\boldsymbol{m})_{new} \geq L(\boldsymbol{m})_{old}$ **then**
      $\boldsymbol{m}_{old} = \boldsymbol{m}_{new}$
      $L(\boldsymbol{m})_{old} = L(\boldsymbol{m})_{new}$
    else
      $P(\lambda, x) = \frac{1}{\lambda} e^{-\frac{x}{\lambda}}$
      if *random number from* $P(\lambda, x) > 1$ **then**
        $\boldsymbol{m}_{old} = \boldsymbol{m}_{new}$
        $L(\boldsymbol{m})_{old} = L(\boldsymbol{m})_{new}$
      else
        $\boldsymbol{m}_{old} = \boldsymbol{m}_{old}$
        $L(\boldsymbol{m})_{old} = L(\boldsymbol{m})_{old}$
      end
    end
  end
end

Algorithm 1: Parameter estimation algorithm based on simulated annealing

The output of the parameter estimation algorithm is a matrix of parameters $\boldsymbol{m}$: the solutions $\boldsymbol{s}$. They are samples of the posterior distribution $\sigma(\boldsymbol{m})$ and are represented as a matrix of likely source pressure values for each source grid node:

$$\boldsymbol{s} = \begin{array}{c} \\ \boldsymbol{m_1} \\ \boldsymbol{m_2} \\ ... \\ \boldsymbol{m_{n_{solutions}}} \end{array} \begin{array}{c} \begin{array}{ccccc} p_{node\ 1} & p_{node\ 1} & p_{node\ 3} & \cdots & p_{node\ n_{nodes}} \end{array} \\ \begin{pmatrix} 0 & 3456.5 & 2745.3 & ... & 7453.4 \\ 567.3 & 1322.5 & 0 & ... & 0 \\ ... & ... & ... & ... & ... \\ 477.4 & 0.7 & 230.6 & ... & 546.7 \end{pmatrix} \end{array} \tag{34}$$

Each solution has its own likelihood value (from 0 to 1). For example:

$$L(\boldsymbol{s}) = \begin{array}{c} \\ \boldsymbol{m_1} \\ \boldsymbol{m_2} \\ ... \\ \boldsymbol{m_{n_{solutions}}} \end{array} \begin{array}{c} L(\boldsymbol{m}) \\ \begin{pmatrix} 0.63 \\ 0.94 \\ ... \\ 0.82 \end{pmatrix} \end{array} \tag{35}$$

The prior $\rho(\boldsymbol{m})$) and posterior distribution $\sigma(\boldsymbol{m})$ of the source pressure at one grid node are visualized in figure 33. The a priori distribution (before the inversion, left panel) at each grid node is given as a uniform distribution from the minimum to the maximum source pressure. It is determined by the minimum and maximum total source pressure (p_{min} and p_{max}) using equation 28. The a priori Monte Carlo samples, which form the starting points of the Monte Carlo Markov chains, are displayed as red dots. The solutions the MCMCs provide after the inversion, are samples of the a posteriori distribution. It is displayed in the right panel as a green line, and the solutions $\boldsymbol{s}$ (the a posteriori Monte Carlo samples) are displayed as red dots. How to use the solutions $\boldsymbol{s}$ to estimate the maximum of the posterior distribution, and thereby the most likely source pressure grid, will be discussed in the next section.

5.5. Interpretation of inversion results

Due to computational constraints, the inversion algorithm cannot calculate the exact shape of the posterior distribution $\sigma(\boldsymbol{m})$. Instead, we obtain a set of samples describing the maximum of $\sigma(\boldsymbol{m})$: the solutions matrix $\boldsymbol{s}$. From this matrix, the median source pressure at each grid node can be calculated as follows:

$$\text{median}(\sigma(\boldsymbol{m})) \approx \text{median}(\boldsymbol{s}) \tag{36}$$

This measure is termed the median source pressure grid (median of $\sigma(\boldsymbol{m})$). It is a robust measure of the likely source pressure at a each grid node. However it does not incorporate the likelihood value $L(\boldsymbol{s})$ assigned to each solution. In order to find the source pressure grid with maximum likelihood $\max(\sigma(\boldsymbol{m}))$, the median of solutions with a likelihood larger than a certain threshold percentile is used:

$$\max(\sigma(\boldsymbol{m})) \approx \text{median}(\ \boldsymbol{s}(L(\boldsymbol{s}) > L(\boldsymbol{s})_{percentile\ threshold})\ ) \tag{37}$$

This approximation method is used due to the limited number of solutions $\boldsymbol{s}$. We cannot be sure where the true maximum is located and cannot assume a Gaussian shape to successfully represent the posterior distribution at each grid node. Therefore, taking the

median of solutions with a likelihood better than a certain threshold was found to be the best estimate of the maximum likelihood source grid. The threshold percentile can be varied and depends on how large the variation in the posterior distribution is and how many solutions were generated. In general, taking the median of solutions with a likelihood greater than the 75th percentile (of the likelihood), has proven to be a valid approximation of the maximum likelihood source grid (the maximum of the posterior distribution).

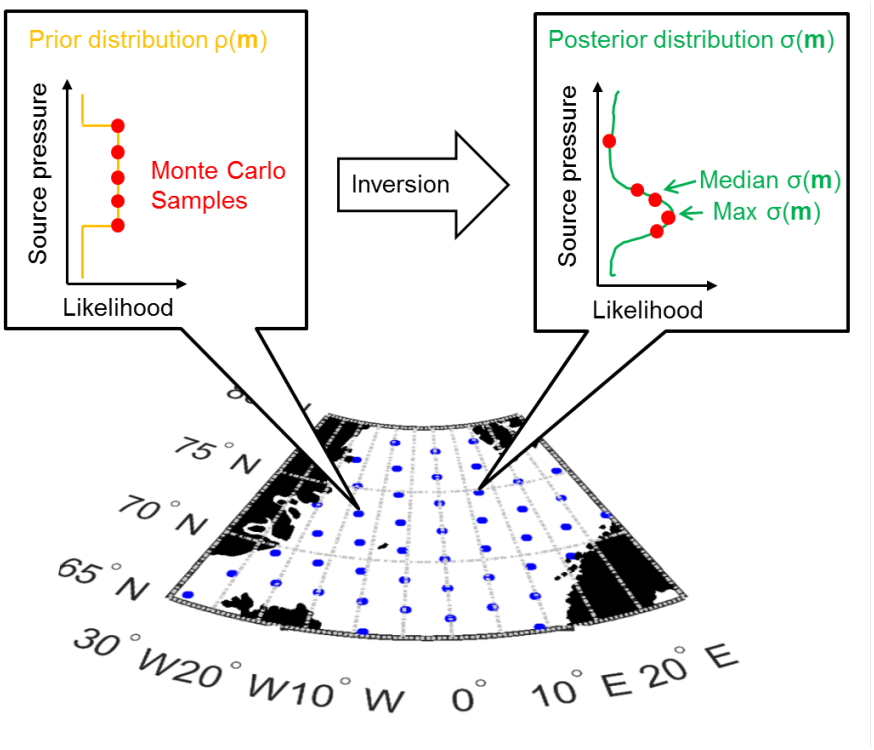

Figure 33: Schematic view of a priori and a posteriori distribution at each simulated source grid node (blue dots). Yellow and Green lines represent $\rho(\boldsymbol{m})$ and $\sigma(\boldsymbol{m})$, red dots the Monte Carlo samples that sample them.

To determine how certain the source pressure at a grid node could be determined, the inter quartile range source pressure (IQR) is subtracted from the median source pressure at each node. The IQR is defined as the range between the 25th and 75th percentile value of the source pressure. If the median source pressure is greater then the IQR, the source pressure estimate at that node is deemed certain. This leads to the practical measure of the ratio of certain grid nodes:

$$r_{certain} = \frac{\sum \text{median}(\boldsymbol{s}) \geq \text{IQR}(\boldsymbol{s})}{n_{nodes}} \tag{38}$$

The most practical way to visualize and interpret the result of an inversion, is to display the source grids that correspond to the median and maximum of the posterior distribution as contour maps. To show which source grid nodes can be trusted (that have a narrow posterior probability distribution), the grid nodes with low uncertainty (with a median source pressure larger than the IQR) are plotted over the source grid as red dots.

This corresponds to equation 38 which estimates the ratio of certain grid nodes. For the median source grid the contours are interpolated using all grid nodes. The contours of the maximum likelihood source grid are interpolated only from nodes with low uncertainty.

An example result is displayed in figure 34. It can be seen that the true source distribution is represented well by the maximum likelihood source grid (lower right panel). The upper right map shows the median source grid. The areas defined by gray-scale contours contain sound sources. Darker areas indicate higher source levels. When a gray area contains red dots (representing grid nodes with low uncertainty), it is considered certain. However, if a gray area does not contain red dots, its source pressure is questionable. For example, the gray areas east and west of the true source distribution, contain no dots. This indicates these are uncertain estimates compared to the gray area corresponding to the true source distribution. Combining the gray contour areas (source pressure grid) and red dots (grid nodes with low uncertainty) is a useful way to interpret the inversion results.

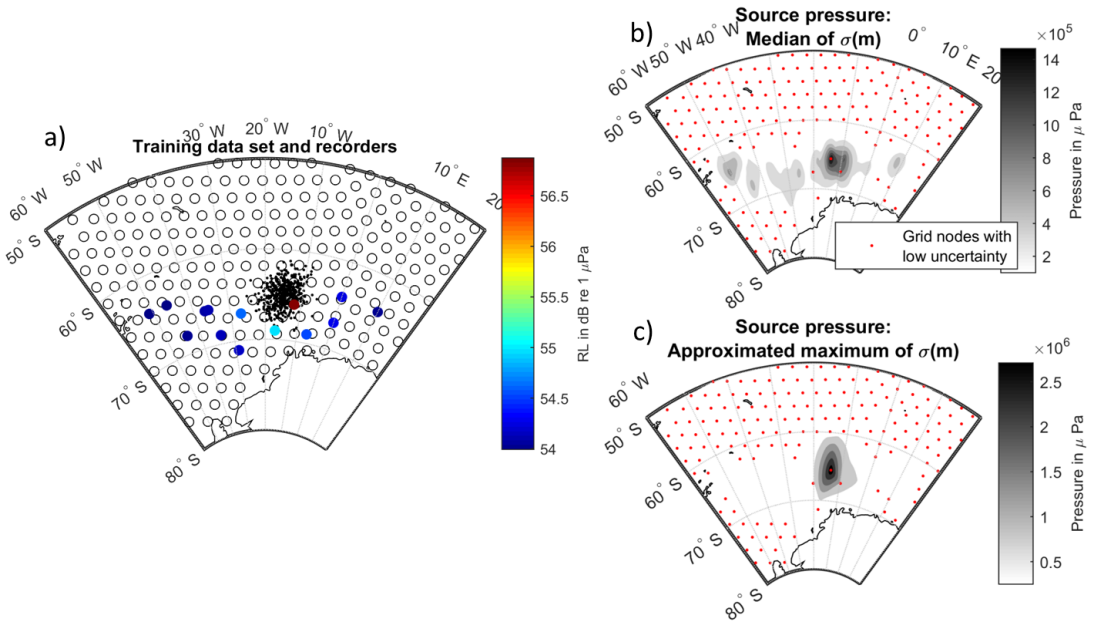

Figure 34: Example to demonstrate the inversion in and output. Plot a shows the input data, the black dots represent the true sources, the colored dots the recorders and their respective RL and the white circles the simulated source grid nodes. Plot b shows the median source grid and plot c the maximum likelihood source. The red dots in plot b and c represent the grid nodes with low uncertainty (median larger than the IQR).

6. Results

6.1. Benchmark scenario: Gaussian source distribution

To test the capabilities of the inversion algorithm and determine the sensitivity to the different input variables, a benchmark scenario was developed. It consists of 500 sound sources (fin whales) that are distributed as a 2D Gaussian centered at 66°N and 5°E. Figure 35 shows the location of the sources and the respective whale density. The source level of each whale was randomly assigned using a Gaussian distribution with a mean of 180 dB re 1 µPa and 10 dB standard deviation. All simulated whales were assumed to have a call rate of 2.5 calls per minute (calling 50% of the time). This results in a total source pressure of $1.9\,10^7$ µPa.

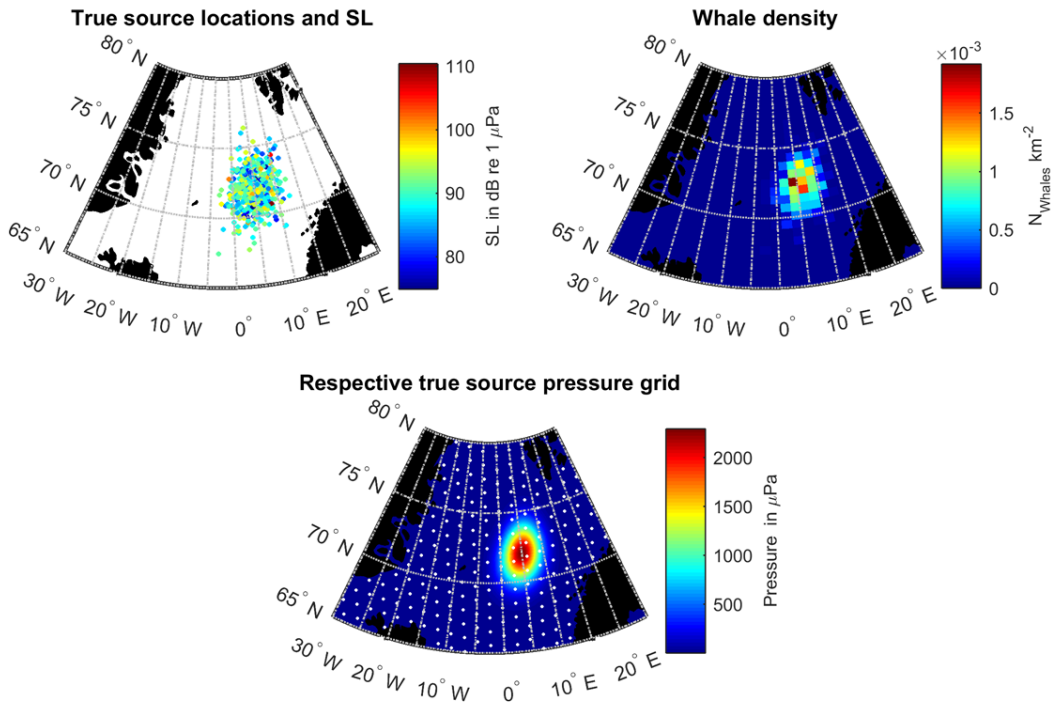

Figure 35: Source data for benchmark scenario: True distribution of sources and source level (upper left plot), respective whale density (upper right plot) and respective true source pressure grid using 195 simulated sources (lower plot).

The studied area (the simulated source grid) was restricted to a rectangle between 65°N and 80°N, and 30°W and 30°E. The simulated source pressure grid that corresponds to the benchmark scenario is shown in the lower panel of figure 35. It is the "true" source pressure grid. Since we assumed constant call rate and spatially independent normally distributed source levels, the whale density and source grid have an almost identical shape. In reality however, call rate and source level are not independent of lo-

cation and are likely not Gaussian. Thus the source grid does not necessarily represent the whale density, but rather whale calling activity.

The "observed" received level was determined using the sonar equation (Eq. 4) and two different TL models: Geometrical spreading and raytracing with BELLHOP. The respective received levels for 195 receivers (on a geodesic grid) are displayed as contour lines in figure 36. The left panel shows the RL when using geometrical transmission loss and the right panel the RL when using BELLHOP and 2xN dimensional raytracing. The environmental conditions for both TL models were the same as described in section 5.3.3. For both TL scenarios the "observed" received levels varied between 54 and 59 dB re 1 µPa.

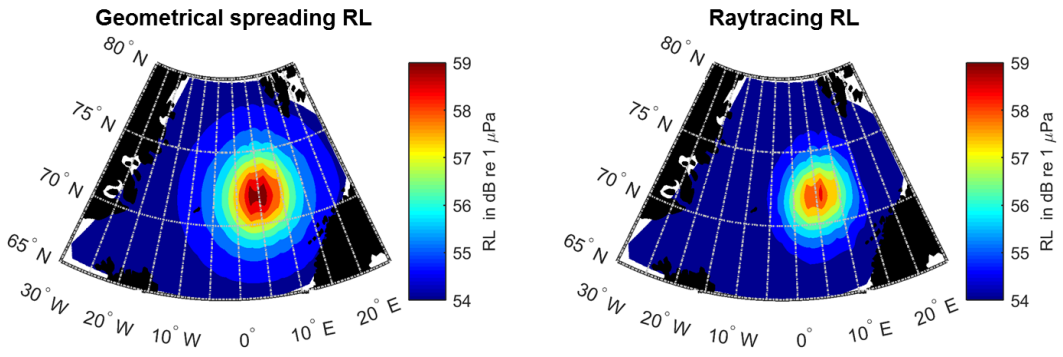

Figure 36: Benchmark scenario received levels using geometrical spreading (left plot) and raytracing (right plot). True received level interpolated from an array of 195 recorders in a geodesic grid at 100 m depth

6.1.1. Sensitivity of inversion algorithm

This section describes the sensitivity of the inversion algorithm (Figure 21) to changes in the input variables. The "observed" received levels are given by the sonar equation (Eq. 4) and geometrical spreading transmission loss (Figure 36). Three performance metrics were used to determine how well the inversion algorithm estimated the source grid under changing input variables. The first two describe the fit between true and inversed source grid: The correlation coefficient r^2 between the inversed and "true" source grid and the misfit (measured as the negative sum of squared errors (-SSE) between the "true" and inversed sound grid in dB re 1 µPa). The third useful measure of performance, is the ratio of certain source grid nodes $r_{certain}$ (Equation 38). It describes difference between the solutions.

To calculate the response of the performance metrics to changes in the input variables, inversions of the "observed" RL were calculated varying one input variable each and keeping the others fixed to a standard. The standard input variables are presented in table 2.

Table 2: Standard input variables used for the sensitivity analysis

$n_{iterations}$	10000
$n_{solutions}$	10
ε	5
p_{min}	$1\ 10^7$ µPa
p_{max}	$3\ 10^7$ µPa
Simulated source grid	Geodesic grid with 195 nodes
Recorder location	Geodesic array with 12 recorders
TL matrix	Geometrical spreading
s	1 dB

The first input variable to be tested was the number of recorders. For this 3 scenarios were used: 3, 12 and 47 recorders arranged as geodesic array (similar to the simulated source grid in figure 26). The results are shown in figure 37. The inversion algorithm showed increasing accuracy with increasing recorder number: The correlation and fit between the "true" and inversed model increased almost linearly with the number of recorders, as did the ratio of certain grid nodes.

In addition to the number of recorders, the number of nodes in the simulated source grid affects the accuracy of the inversion. Figure 37 shows that, for the median source grid, the correlation coefficient r^2 decreased with increasing source grid resolution. For the maximum likelihood source grid, r^2 increased with increasing source grid resolution. The misfit and ratio of certain grid nodes decreased with an increasing number of source grid nodes.

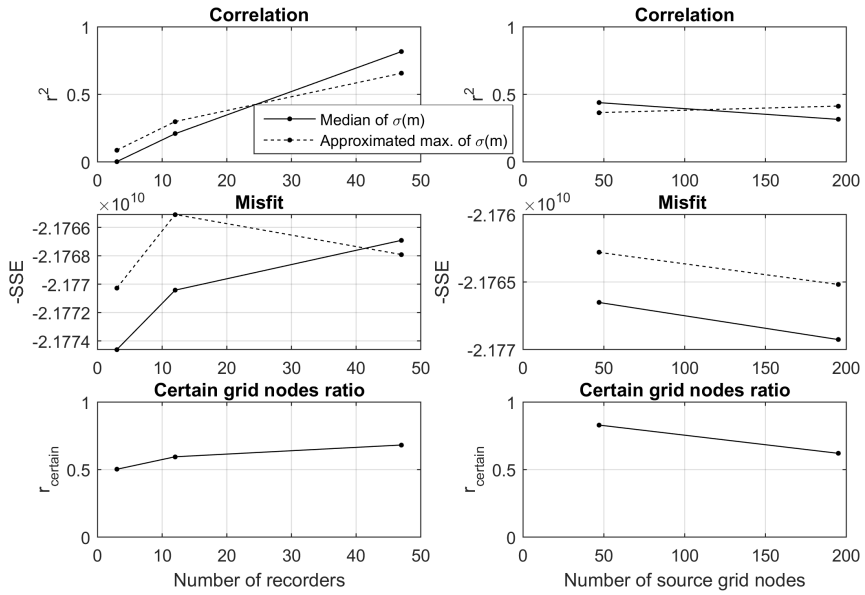

Figure 37: Sensitivity of inversion algorithm to the number of recorders (on the left) and the number of source grid nodes (on the right).

The number of generated solutions determines how well the a posteriori probability distribution $\sigma(\boldsymbol{m})$ is sampled. Varying this parameter resulted in little change of correlation and misfit between the "true" and inversed grid (Figure 38). The certain grid nodes ratio increased with increasing number of solutions. This is a promising result which demonstrates, that as few as 10 solutions are sufficient to sample $\sigma(\boldsymbol{m})$ successfully. To increase the number of certain grid nodes however, the number of solutions is best when greater than 20. However, the optimal number of solutions will depend on the range between the minimum and maximum total source pressure.

The number of iterations used to find the maximum of the likelihood function, showed surprisingly little influence on the results of the inversion (Figure 38). The misfit and correlation between true and inversed source grid decreased slightly with an increasing number of iterations, whereas the certain grid nodes ratio increased.

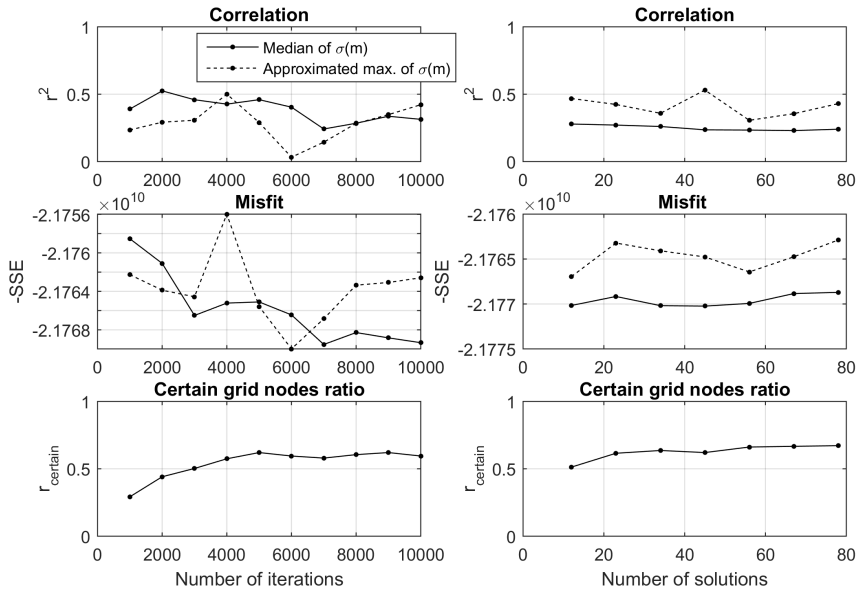

Figure 38: Sensitivity of the inversion algorithm to the number of iterations (on the left) and the number of solutions (on the right).

The total pressure range between p_{min} and p_{max}, is a priori information used for the inversion. For the benchmark scenario the true total pressure is $1.9\ 10^7$ µPa. For the sensitivity analysis, the pressure range was increased from 0 to 4 times the true total pressure (Figure 39). The correlation between "true" and inversed source grid increased until the pressure range equaled the "true" pressure, and decreased after the pressure range was about 3 times larger than the "true" pressure. The misfit between "true" and inversed grid however, showed little response to changes in the a priori pressure range. In contrast, the certain grid nodes ratio decreased with increasing pressure range, until the pressure range was double the "true" pressure.

The cooling exponent ε was increased from 2 to 8. This showed little effect on the inversion results (Figure 39). Both correlation and misfit between inversed and "true" source grid showed no clear trend with increasing ε. The same applies to the ratio of certain grid nodes.

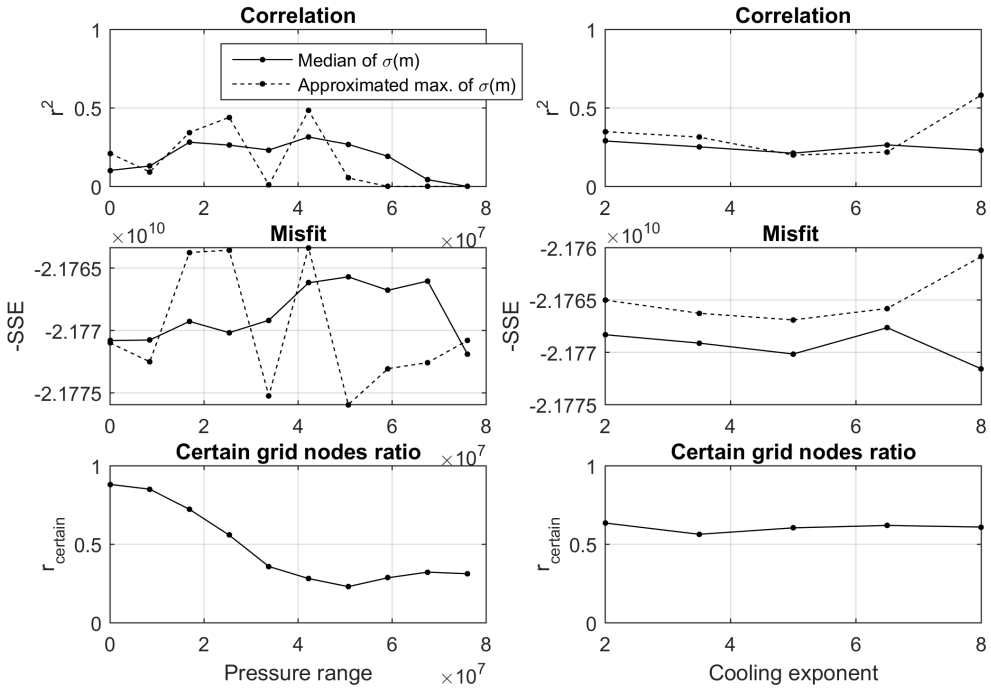

Figure 39: Sensitivity of inversion algorithm to the range of a priori pressure p_{sum} (on the left) and the cooling exponent (on the right). The true source total pressure is $1.9\ 10^7$ µPa.

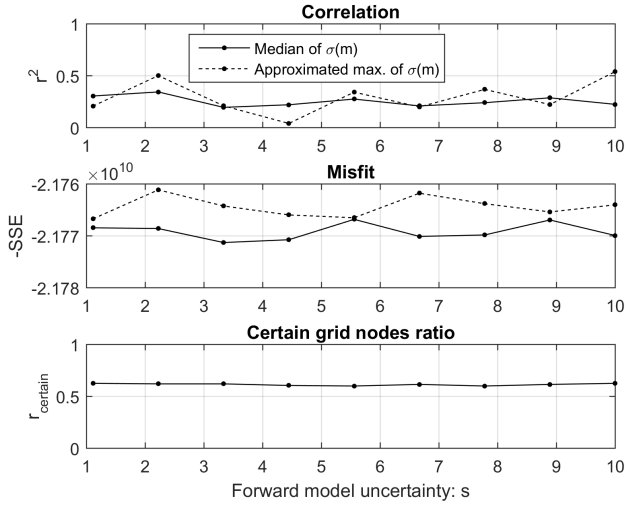

Figure 40: Sensitivity of inversion algorithm to the forward model standard deviation s.

An critical input variable is the forward model uncertainty s. Since the forward model and TL matrix will always contain errors, it is necessary to know how much uncertainty the inversion method can tolerate. The results for varying the forward model standard deviation between 1 and 10 dB are presented in figure 40. Correlation and misfit between true and inverse source grid, as well as the certain grid nodes ratio showed no trend with increasing forward model standard deviation.

6.1.2. Raytracing vs. geometrical spreading TL matrix

To quantify the effect an imprecise transmission loss model has on the inversion results, the "observed" RL of the benchmark scenario was calculated using 2xN dimensional raytracing (right plot of figure 36). The TL Matrix used for the inversion on the other hand, was calculated using geometrical spreading. The mean absolute difference between the raytracing and geometrical spreading TL matrix was 6.8 dB. The mean absolute difference between the resulting received levels was 0.48 dB (with RL estimates being higher when using geometrical spreading instead of raytracing).

The performance metrics (describing the accuracy of the inversion, see previous section) were calculated for 10 inversions with forward model standard deviation ranging from 1 to 10 dB (Figure 41). This sensitivity analysis showed that the correlation, misfit and ratio of certain grid nodes varied little with increasing forward model standard deviation. These results were remarkably similar to the sensitivity analysis in figure 40, where the same TL matrix was used to calculate the "observed" RL and the inversion. However, the ratio of certain grid nodes was around 0.2 lower when using non-identical TL matrices. The correlation remained stable ($r^2 \approx 0.3$) with increasing forward model uncertainty, when using both identical and non-identical TL matrices.

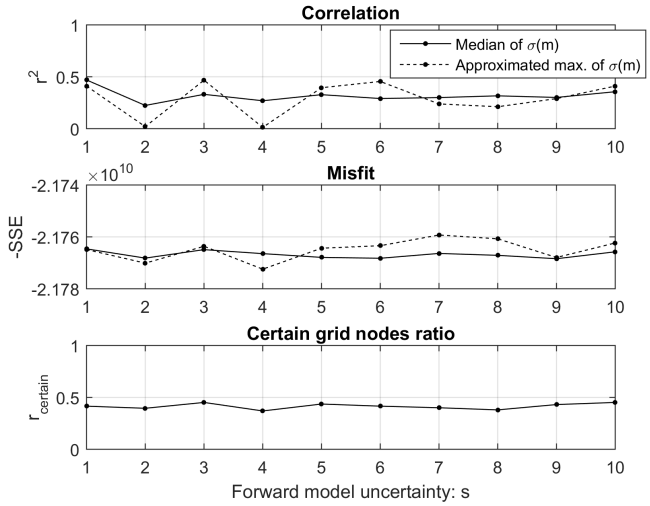

Figure 41: Sensitivity of inversion algorithm to the forward model uncertainty. Observed RL was calculated using a raytracing TL matrix whereas the forward model used a geometrical spreading TL matrix.

Overall, these results show that inversions with an imprecise TL matrix can still produce reliable source pressure grid estimates. This is promising, since every transmission loss model contains errors (due to the assumptions necessary to create them). As this section showed, using an imprecise TL model such as geometrical spreading can still produce reliable inversion results.

6.1.3. Drifting recorders

If the recorders are not stationary, their changing location can influence the results of the inversion. This will be especially relevant when recorders are mounted on drifting platforms such as oceanographic floats. To simulate this effect, the random dispersal of 12 recorders in the North Atlantic was modeled. The initial recorders positions were given as a geodesic array, covering the studied area from 65°N to 80°N and 30°W to 25°E uniformly. They are displayed as black stars in figure 42. For the sake of simplicity, random drift was then modeled assuming a constant drift speed of 0.25 m s^{-1} and constant drift in one direction for 10 days. The direction of drift was assigned randomly for 20 steps. The resulting float trajectories (200 days, distance of 4320 km) show a stepwise transformation from uniform to random recorder distribution. They are displayed as colored dots in figure 42. In reality, float trajectories are influenced by currents and eddies. However, to investigate the effect of recorder dispersion on the accuracy of the inversion algorithm, the assumption of random float trajectories is deemed sufficient.

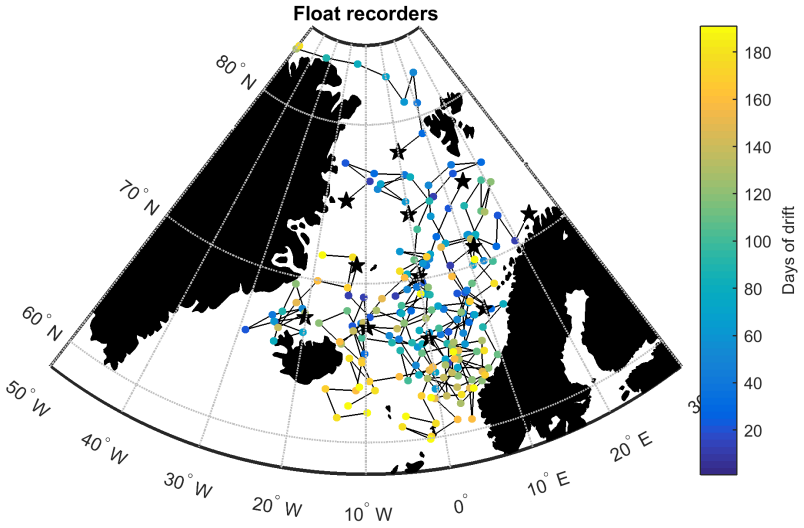

Figure 42: Map showing simulated float tracks. Black stars represent initial locations on geodesic grid, and the colored dots represent the float locations at each random drift step.

The sensitivity of the inversion algorithm to drifting recorders was determined using the Gaussian benchmark scenario. Geometrical spreading was used to calculate both the "true" RL and forward model TL matrix. Figure 43 shows the sensitivity of the inversion

to the random drift. The correlation between true and inversed source grid remained stable, and partially increased up until the 80th day of drift. The same applied to the misfit between "true" and inversed source grid. The ratio of certain grid nodes increased until the 60th day of drift and remained stable afterwards.

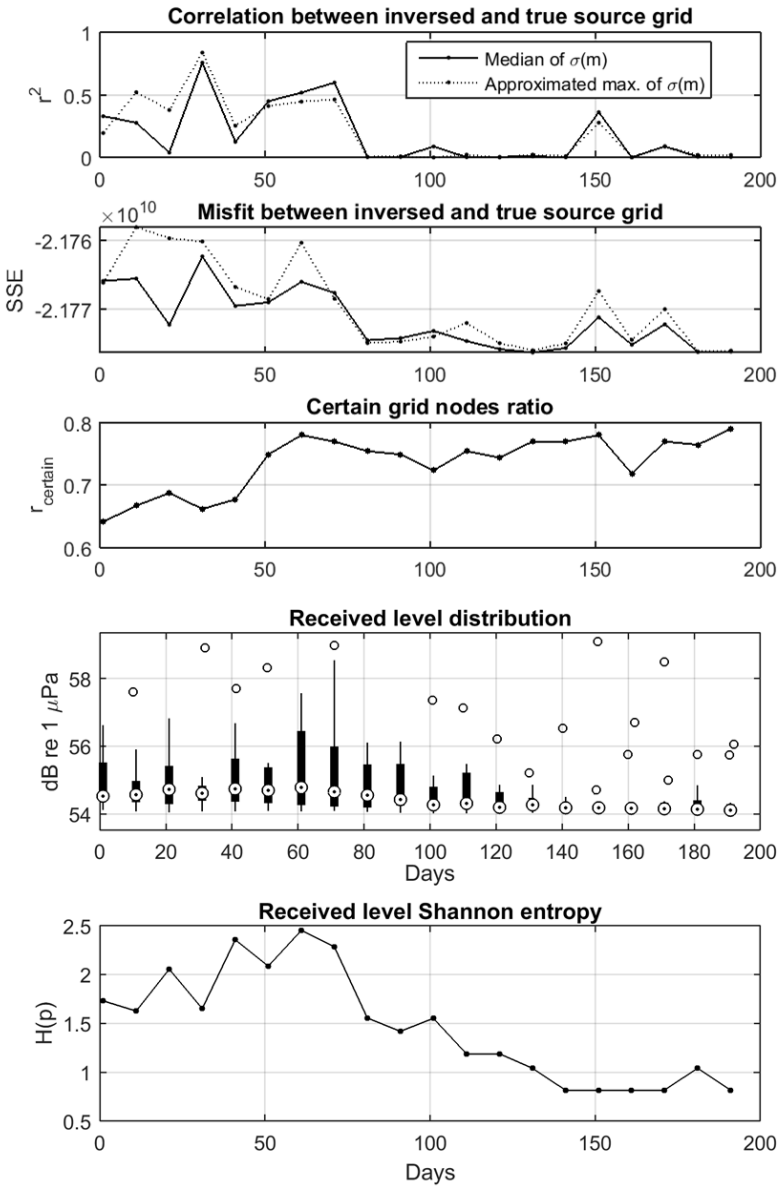

Figure 43: Effect of recorder dispersal on inversion accuracy. From top to bottom the panels display: Correlation between inversed and "true" source grid, Misfit between inversed and "true" source grid, ration of certain grid nodes, the RL distribution (Median as black dots, IQR as a black bar, extreme values as line) and the RL Shannon entropy. X axis represents the drifting time of the simulated floats.

When comparing these trends with the distribution of received levels at each step, it became clear that the inversion success was strongly influenced by the distribution of received levels. The information contained in the received level distribution (P_{RL}) can be described by the Shannon entropy (Shannon, 1948):

$$H(P_{RL}) = -\sum P_{RL} \log_2(P_{RL}) \tag{39}$$

It is a measure of information content (Borda, 2011), which reaches its maximum when all elements of a distribution have the same likelihood of occurring (uniform probability distribution). The Shannon entropy of the received level distribution is displayed in the lowest plot of figure 43. It increased until 80 days of simulated float drift, and then decreased abruptly to lower levels. This pattern agrees well with the correlation and misfit between the "true" and inversed source grid.

These results suggest that, as long as the RL distribution contains enough Shannon entropy ("is uniform enough"), the inversion method tolerates random recorder movement. The best inversion was achieved after 30 days of simulated drift, and is displayed in figure 44. An example of an unsuccessful inversion (after 90 days) can be found in the same figure. Although the correlation between the true and inversed source grid was zero, the median source grid of the unsuccessful inversion still indicated sound pressure near the true source locations.

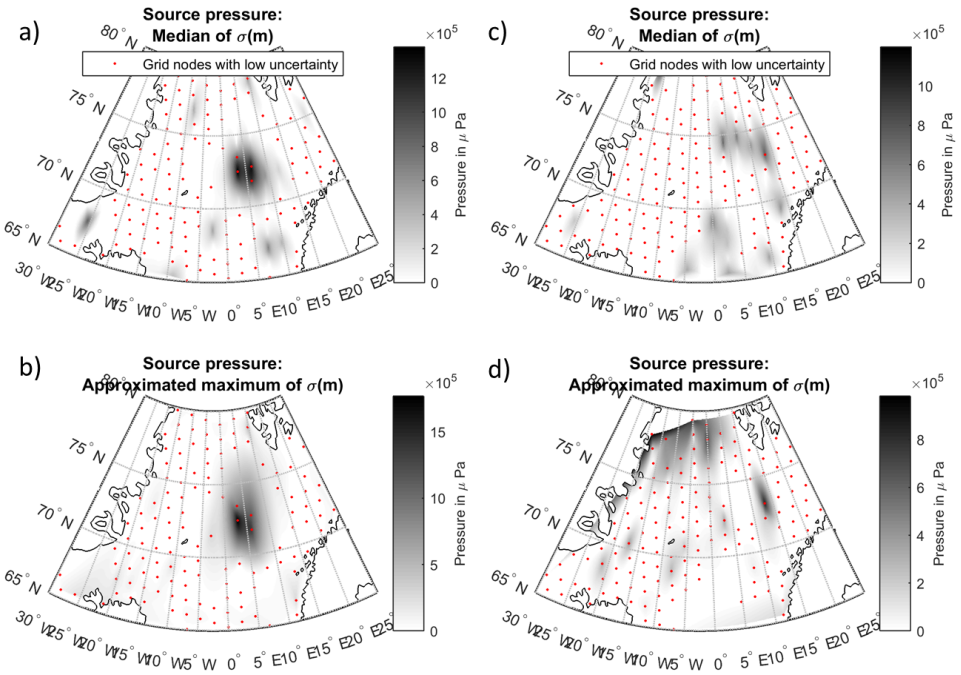

Figure 44: Inversed source pressure grid using drifting recorders. Plots a and b show a successful inversion 30 days after float release, plots c and d an unsuccessful inversion 90 days after float release.

The simulated float drift also revealed an artifact in the misfit calculation. When the recorder and source grid node locations overlap, the misfit values will be much higher for the first quarter iterations, compared to locations that do not overlap. Roughly after the first quarter of iterations, the misfit jumps over several orders of magnitude to lower values. The misfit difference between overlapping and non-overlapping recorder and source grid node locations, is displayed in figure 45. It can be explained by the fact that, in the beginning of the iterations there is one simulated source on each node. Thus the simulated RL at this node equals its SL plus the RL from all other sources. This renders the RL at the node locations much higher and creates a larger misfit between simulated and observed RL.

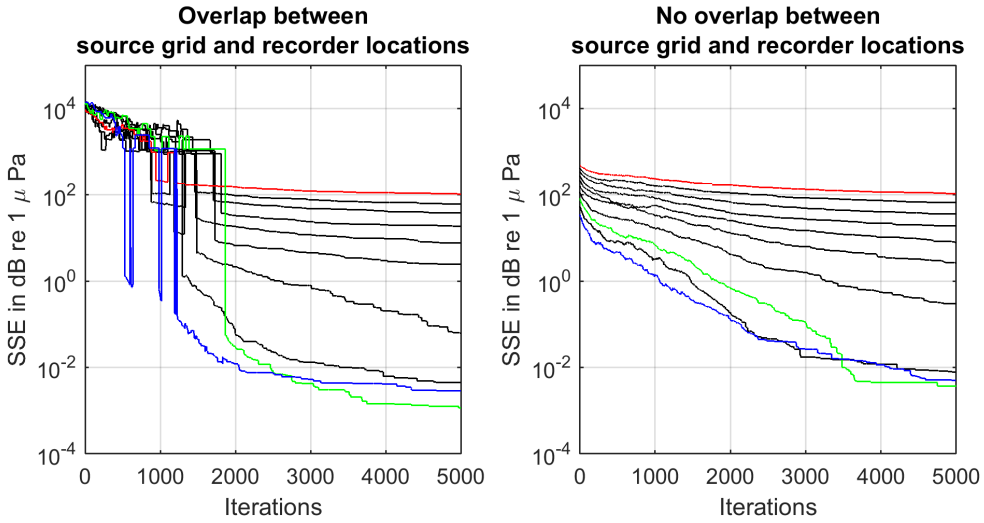

Figure 45: Misfit jump artifact resulting from overlap between source grid nodes and recorder locations. Left panel shows performance of inversion algorithm for initial float positions (Recorder in geodesic grid, 100 % overlap), right side for floats after 50 days of simulated drift (no overlap).

6.2. Recorder array coverage

6.2.1. Confidence regions

To determine the performance of an array of recorders, it was tested how reliably a source at each grid node could be found by the inversion algorithm. For each grid node, a true source grid and received level observations were generated, assuming a source level of 200 dB re 1 µPa at the selected node and no sources at all other nodes. Following this, the inversed source grid was estimated from the respective received level observations. To quantify how reliably a source at each node was found, the correlation between the respective "true" and inversed median source pressure grid was calculated. The exact values of the correlation coefficients were of minor interest, since they will vary with all inversion input variables. Therefore, the correlation coefficients were normalized (dividing each value by the maximum correlation coefficient). Regions with high correlation coefficients indicate the confidence region. In these areas the inversion algorithm can

find sound sources with high certainty. Extending the simulated source grid outside of the confidence regions will produce less certain results.

The confidence region for a geodesic array with 12 recorders between Iceland and Svalbard, is displayed in figure 46. It was calculated using 5000 iterations, 5 solutions, a cooling exponent of 4, p_{min} of $5\ 10^9$ µPa, p_{max} of $1.5\ 10^{10}$ µPa and a forward model standard deviation of 6 dB. In the area between Iceland and Svalbard the correlation coefficients between the "true" and inversed source grid are sufficiently high. However, south of Iceland too few recorders are present for a successful inversion and the correlation coefficients drop to zero.

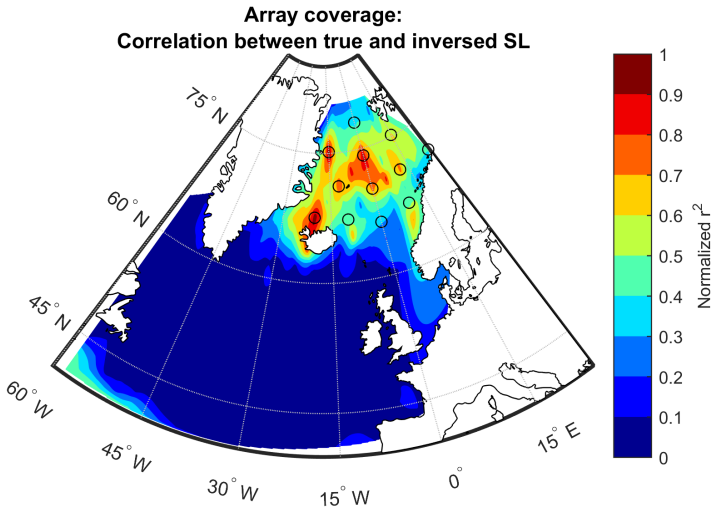

Figure 46: Map showing confidence region of geodesic recorder array. Contours show normalized correlation coefficients between the "true" and inversed source grid for a source at each of the grid nodes. Black circles show recorders location.

6.2.2. Sources outside the confidence region

The confidence region describes the area where the inversion algorithm can find sound sources with high certainty. If all sound sources are within this confidence regions, the inversion algorithm will be able to find their distribution and source pressure. However, what will happen when there are sound sources outside of the area covered by the recorder array? This has been simulated for the 12 recorder array between Iceland and Svalbard. The true sources were located in a Gaussian distribution south of Greenland (Figure 47). The inversion algorithm was run with 2 simulated source grids: One covering the entire North Atlantic and another covering only the confidence region. The results are displayed in figure 48.

For the source grid extending further than the confidence region, over the entire North Atlantic, no successful inversion was achieved. However, the inversion results for the source grid covering only the confidence region, confirmed that there are no sources present between Iceland and Greenland. This corresponds to the "true" source distribu-

tion where all sources were located south of Greenland. The median source pressure grid showed some nodes where sound was emitted, yet these had a high uncertainty (they are not marked with a red dot). The maximum likelihood source pressure grid indicated sound sources in the corner of the grid that faced the direction of the true sources.

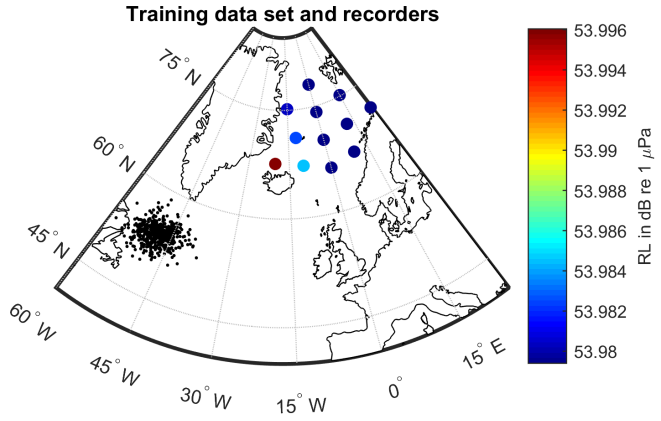

Figure 47: Map of scenario with a Gaussian source distribution outside of the receiver arrays confidence area. Black dots represent sources, colored dots recorders and RL.

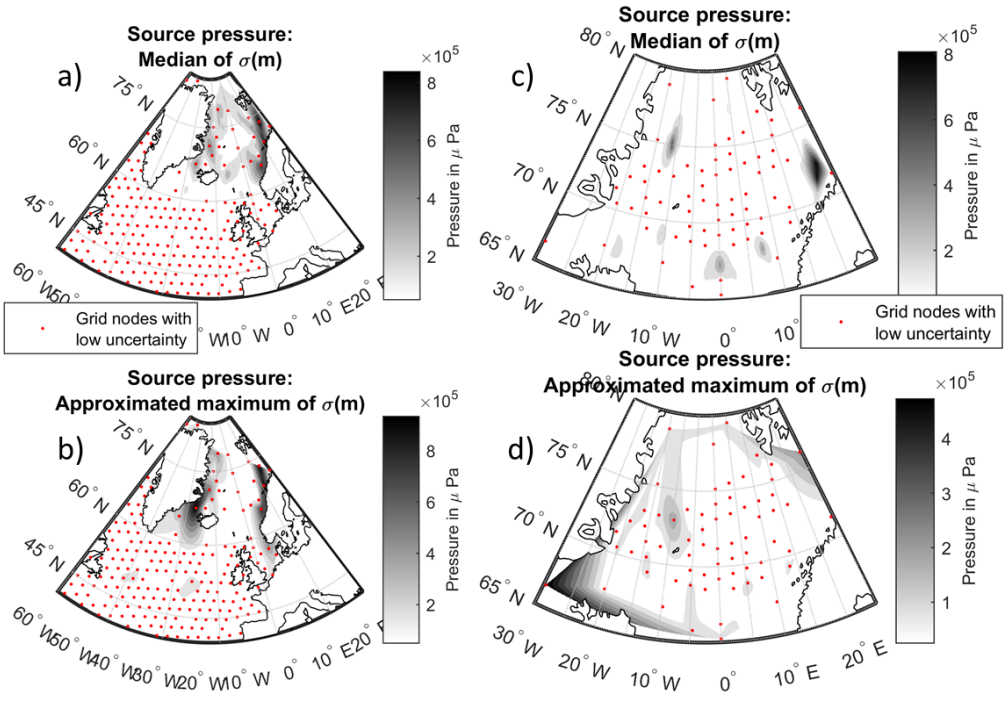

Figure 48: Inversion results for a simulated source grid limited to the confidence region of the recorder array (plots a and b), and a source grid extending further than the confidence region (plots c and d).

6.3. Inversion of published fin index measurements

The inversion method was applied to a composite dataset, generated from fin index measurements by Nieukirk et al. (2012) and Klinck and Nieukirk (2012). Since the fin index is approximately a SNR measurement, the chorus received level was approximated by adding a noise floor of 90 dB to all fin index measurements. This means we assume a constant noise level throughout the North Atlantic. Unfortunately the recordings from Nieukirk et al. (2012) and Klinck and Nieukirk (2012) do not fully overlap in time. Consequently, a composite dataset was generated using average fin index values from the 1st of January for each recorder. Since there is considerable inter-annual variation in fin index measurements and real ambient noise levels are not constant throughout the North Atlantic, this dataset is only a very rough approximation of the actual fin whale chorus RL. However it is deemed useful to test the inversion method. The composite dataset and simulated source grid are displayed in figure 49.

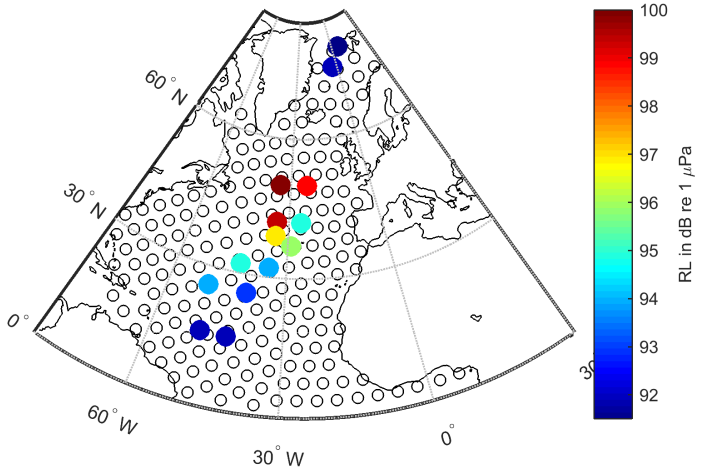

Figure 49: Map showing recorder locations and received level as colored dots. Empty circles represent the simulated source grid nodes. Recorder RL and locations taken from Nieukirk et al. (2012) and Klinck and Nieukirk (2012).

The search space (the simulated source grid), is confined to the deep water and shelf seas of the North Atlantic, excluding narrow estuaries. The recorder array does not cover the search space uniformly. Analysis of the confidence area of the recorder array (Figure 50), showed that the recorder array is far from perfect for an optimal inversion. It does not cover the simulated source grid evenly, thus sources on grid nodes east and west of the narrow recorder array are harder to find for the inversion algorithm. Even within the recorder array, optimal coverage is only achieved where the recorders are close enough to each other (at roughly 40°N). However, as the result will show, the inversed source grid still indicates realistic patterns of fin whale vocal activity. This is likely due to the fact that the received levels were spread from 92 - 100 dB re 1 µPa, which means that the RL distribution had a high Shannon entropy.

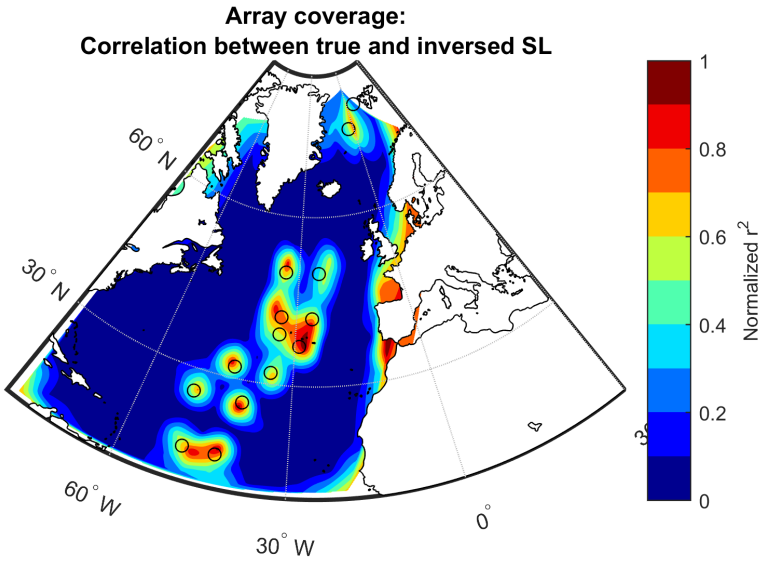

Figure 50: Map showing confidence region of recorder array used by Nieukirk et al. (2012) and Klinck and Nieukirk (2012). Contours show normalized correlation coefficients between the "true" and inversed source grid for a source at each of the grid nodes. Black circles show recorders location.

The inversion was calculated using a geometrical spreading transmission loss matrix, 5000 iterations, 50 solutions, a cooling exponent of 4 and a forward model uncertainty of 6 dB. The minimum and maximum total source pressure were based on published data. The average fin whale source pressure $\overline{p}$ was assumed as $2.8184\ 10^9$ µPa, the average pulse length t_{pulse} as 1 s and the average inter pulse interval t_{IPI} as 12 s (Weirathmueller et al., 2013, Watkins et al., 1987, Morano et al., 2012). The minimum total source pressure is emitted if only one whale calls:

$$p_{min} \approx 1\ \overline{p}\ \frac{t_{pulse}}{t_{pulse} + t_{IPI}}\ \approx\ 2.168\ 10^8\,\text{µPa} \tag{40}$$

The maximum total source pressure will be achieved if the maximum estimated number of males call simultaneously. The maximum estimate of fin whales in the North Atlantic by the IWC is 40 000 (IWC, 2015). If we assume a 1:1 sex ratio and that only males call, the maximum total source pressure can be assumed as follows:

$$p_{max} \approx 20000\ \overline{p}\ \frac{t_{pulse}}{t_{pulse} + t_{IPI}}\ \approx\ 4.336\ 10^{12}\,\text{µPa} \tag{41}$$

How the parameter estimation algorithm manipulated the misfit and likelihood of the Monte Carlo Markov chains, is displayed in figure 51. Due to the large range of possible total source pressure values, the spread in misfit and likelihood between the solutions is large. The solution with the highest likelihood has a total source pressure of $4\ 10^{10}$ µPa. The parameter estimation could reduce the sum of squared errors between simulated and true RL as low as 10 dB.

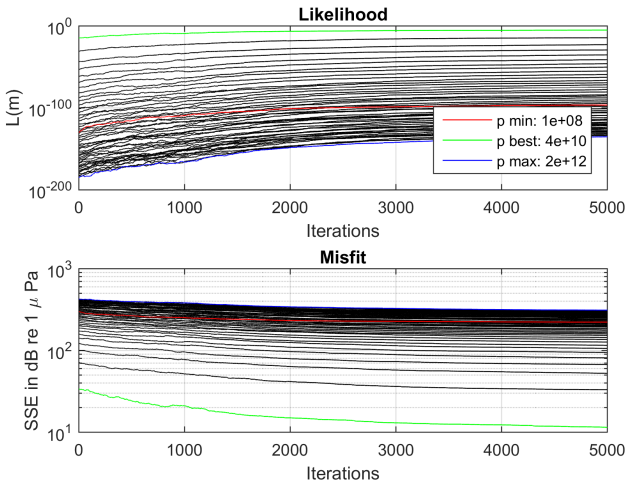

Figure 51: Misfit and likelihood over iterations, each line represents one model $\boldsymbol{m}$. Y axis on both plots in logarithmic scale. The legend shows the total source pressure for the most likely solution and the solutions with p_{min} and p_{max}.

The source pressure grids corresponding to the median and maximum of the posterior distribution are displayed in figure 52. The median source grid shows an area of intense fin whale calling activity along the Caribbean and American coastlines. However, there are no grid nodes with low uncertainty (red dots) in the corresponding gray area, rendering this estimate questionable. The remainder of the North Atlantic contains no sources in the median source grid. However, the maximum likelihood source grid indicates that sound pressure is emitted in Davis strait, along the Norwegian coast and near the Strait of Gibraltar. The difference between the median and the maximum likelihood source pressure grid, can be explained by the large range of total source pressure values. Many of the solutions will have unrealistic total source pressure values and therefore bias the median source grid. Here it becomes clear, that it is important to consider both the median and maximum likelihood source pressure grid.

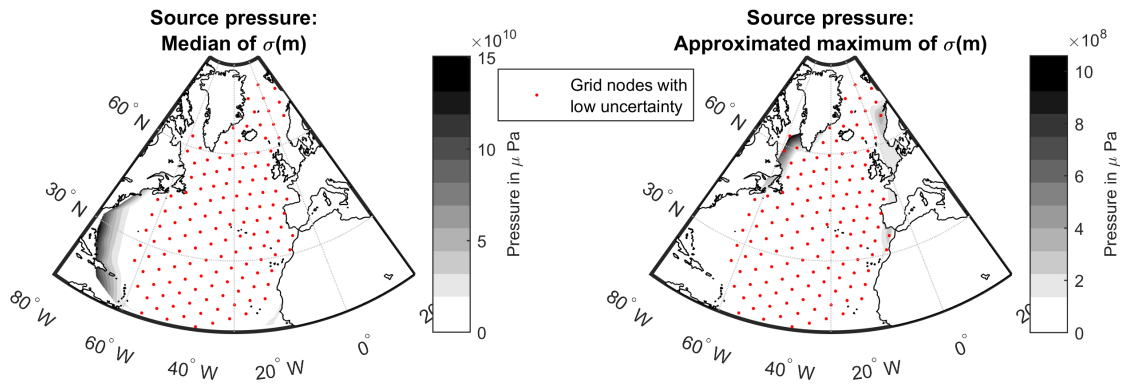

Figure 52: Inversed source pressure grids based on a composite dataset from published fin index measurements. Left plot shows median source pressure grid, right plot the maximum likelihood source pressure grid.

7. Discussion

7.1. Evaluation of inversion method

The inversion method produced promising results both in the benchmark tests and application to real observations. One of the most significant results was, that it is not necessary to have precise knowledge of the TL matrix. Using a geometrical spreading TL matrix for the inversion was sufficiently accurate, even when the true TL matrix was unknown or obtained from a raytracing model (Section 6.1.2). Furthermore, as few as 12 recorders between Iceland and Svalbard, were sufficient to determine the distribution of fin whale calling activity in the Norwegian and Greenland sea (Sections 6.1.1 and 6.2). Another encouraging result was, that accurate knowledge of the a priori total source pressure is not required. Successful inversion was achieved even when the range between the maximum and minimum total source pressure was spanning several orders of magnitudes (Section 6.1.1 and 6.3). The proposed method is able to estimate the distribution of calling fin whales using a small set of recorders, a simple geometrical spreading TL matrix and limited knowledge about the total source pressure. The next sections will discuss the capabilities and limitations of the inversion method in detail.

7.1.1. Recorder array

The sensitivity analysis has shown that increasing the number of recorders almost linearly increases the correlation between true and inversed source grid (Figure 37). This is especially the case when the recorders are arranged as a geodesic grid, covering the studied area uniformly. In general, increasing the amount of a priori information by increasing the number of recorders will result in more accurate estimates. However, as the simulation with drifting recorders demonstrated, the inversion accuracy also depends on the location of the recorders. The simulation of drifting recorders showed, that best inversion result (with a given number of recorders) is achieved when the received level distribution has maximum Shannon entropy (Figure 43). To achieve a successful inversion, the variation of the recorded RL needs to be large enough. The exact soundfield, the vocalizing fin whales create, is not known. Therefore uniformly aligning as many recorders as possible over the studied area, is a secure strategy for successful inversion. The simulation of drifting recorders also demonstrated, that the inversion methods works best when the recorders have fixed locations. This increases the chance of recording enough variation within the received levels (increasing the Shannon entropy).

The confidence area of the recorder array between Iceland and Svalbard indicates, that it is possible to monitor fin whale distribution in the Norwegian and Greenland sea using only 12 recorders (Figure 46). Limiting the simulated source grid to that area will give the best results, and also tolerate sources outside of the simulated source grid. However, the inversion of published fin index measurements showed that meaningful inversion results can also be achieved when the simulated source grid spans areas larger than the confidence area. This is likely due to the large gradient present in the published fin index measurements (high Shannon entropy). If there is only a small gradient in the received levels (low Shannon entropy), inversions outside the confidence regions will be unsuccessful. This can be seen in the 12 recorder example in section 6.2.2. The posterior

distribution can only be successfully determined when the prior distribution and observations contain enough information (that can be quantified as Shannon entropy). This is in agreement with a discussion on Bayesian inversion by Allmaras et al. (2013).

7.1.2. Forward model and parameter estimation algorithm

The sensitivity of the forward model and parameter estimation algorithm to the different input variables is presented in section 6.1.1. A crucial input variable is the resolution and location of the simulated source grid. It contains a priori information: the area where we expect to find vocalizing fin whales. This usually excludes land and shallow or narrow estuaries. The best resolution of the simulated source grid depends on the number of recorders and iterations used. As figure 37 showed, for 12 uniformly located recorders, increasing the simulated source grid resolution higher than 195 nodes, will slightly decrease the fit of the median source grid. In contrast the the fit of the maximum likelihood source grid increased slightly. This is likely caused by an increased resolution, which allows more accurate source pressure grids. On the other hand, a higher grid resolution increases the degrees of freedom, which can introduce larger uncertainties into the source grid estimates. This is likely the reason behind the decreased fit of the median source grid observed with increasing grid resolution. Generally, an increase in source grid resolution must be accompanied by an increase in the number of iterations, since there are more parameters (grid nodes) to be estimated.

Against expectations, increasing the number of iterations did not increase the correlation between the "true" and inversed source grid (Figure 38). This shows that already as few as 1000 iterations are enough to produce successful inversion results. However, the ratio of certain grid nodes benefited from increasing the number of iterations. For the benchmark scenario, using 5000 iterations provided sufficient results. Generally, increasing number of iterations will raise the likelihood to find the "true" source grid. In practice, one needs to find a balance between a high enough number of iterations and increased computational costs.

The correlation between "true" and inversed source grid was insensitive to the number of solutions used for the inversion. As figure 38 showed, around 10 solutions are sufficient for the benchmark scenario inversion. However, the ratio of certain grid nodes increases with increasing number of solutions. The more solutions generated, the better the posterior distribution $\sigma(\boldsymbol{m})$ is sampled. Which in turn will render it more likely to estimate the true maximum likelihood source pressure grid. When increasing the number of solutions, one needs to consider the corresponding increase in computation time. Increasing the cooling exponent has little effect on the outcome of the inversion (Figure 39). The parameter estimation algorithm performs well within the tested range of ε from 2 to 8.

An important a priori information and input variable, is the range between the minimum and maximum total pressure. The best inversion results were achieved when the range was 1 to 3 times the true total pressure (Figure 39). This is supported by the fact, that the ratio of certain grid nodes decreases with increasing a priori pressure range. However, these results strongly depend on the number of solutions used. When more solutions are generated, larger total source pressure ranges can be supported. The so-

lutions are assigned total source pressure values between p_{min} and p_{max}. If the pressure range becomes too large and there are too few solutions, none of the solutions will have a total source pressure near the true total source pressure. With increasing range, the median source grid will become a less useful interpretation of the inversion results, since it does not incorporate the likelihood values assigned to each solution (Eq. 36). On the other hand, the maximum likelihood source grid (Eq. 37) can tolerate large total source pressure ranges, as long as the number of solutions and iterations are high enough. This has been the case for the inversion of published fin index measurements. The total source pressure range spanned several orders of magnitude, and the median source grid contained little useful information compared to the maximum likelihood source grid (Figure 52).

A very promising result is the tolerance of the inversion algorithm to forward model uncertainty (Figure 40). Neither the correlation and misfit between true and inversed source grid, nor the ratio of certain grid nodes decrease with increasing forward model standard deviation (from 1 to 10 dB). This implies that errors in the forward model, due to the discretization of the search space and an imprecise transmission loss matrix, are tolerated. The true transmission loss is affected by a large range of factors ranging from seafloor properties, salinity and temperature variations to sea surface roughness. Since one cannot model all of these processes perfectly, it is crucial that the inversion method can tolerate errors in the forward model. The next section will discuss the effect of different TL matrices on the inversion.

Optimal inversion is achieved using as many recorders as possible, distributed as uniformly as possible. Using a cooling exponent of 4 will give successful results. With 12 recorders and 195 simulated source grid nodes, successful inversion will be achieved using at least 10 solutions and 5000 iterations. It could be shown that for the fin whale chorus (at 20 Hz), the use of a geometrical spreading TL matrix produces successful inversions when the true TL is unknown. This is likely due to the many sources and receivers involved in the inversion. The ensemble average of the TL is more important than the exact TL between each source and receiver. The most important input variables are the received level observations: when the RL data set is too small or does not sample the major gradients of the soundfield, no successful inversion will be achieved.

7.1.3. Transmission loss matrix

The sensitivity analysis in section 6.1.1 demonstrated that the standard deviation of the forward model (including the transmission loss matrix) can be as high as 10 dB (Figure 40). To test whether a simple approximation of the transmission loss is sufficient, the inversion algorithm used a geometrical spreading TL matrix, while the "observed" RL was calculated using the raytracing model BELLHOP. The results (Figure 41) showed that successful inversion can be achieved using a geometrical spreading TL matrix, even though it is only a rough approximation of the true TL matrix.

This reduces the computational costs of the inversion method. Most underwater sound propagation models require long computation times, and need to be run on a computer-cluster if many sources and receivers are involved. However, it might be necessary to use

advanced propagation models to calculate the TL matrix when the studied area is small and involves complex bathymetry, many islands and/or fjords (Heaney et al., 2013). A useful approach could be, to calculate the TL matrix using an adiabatic mode propagation model. It can include the effect sea-mounts and islands have on the TL more accurately than 2 D raytracing models like BELLHOP (Heaney et al., 2012, Ballard, 2012). For North Atlantic fin whale chorus inversion, the results indicate that using a geometrical spreading TL matrix is sufficient. However, this is only applicably to the fin whale chorus inversion at 20 Hz. For higher frequency marine mammal choruses, such as the Minke whale chorus, it might be necessary to use more advanced transmission loss models.

7.1.4. Limitations

The major limitations of the inversion method is its dependency on sufficient chorus RL observations and that it can only provide information about the presence (and calling activity) of fin whales, but not information about their absence. The source pressure grids indicate where (and how much) fin whale calling activity occurs and where not. It is not yet possible to convert fin whale calling activity to fin whale density, since each whale vocalizes with a slightly different source level and call rate. Large scale tagging studies might be able to gather enough data to derive a mean source level and call rate, but these will likely differ significantly between the sub-populations, seasons and individual whale behavior (Goldbogen et al., 2014).

The increasing noise from shipping and seismic survey could render marine mammal chorus observations difficult. The fin whale chorus needs to be discernible as a distinct peak in the power spectra density of a recording. Otherwise it is not possible to determine the chorus received level. Along the major shipping lines between Europe and America and close to the coast, masking due to anthropogenic noise could prohibit successful marine mammal chorus observations (Gervaise et al., 2012, Van Der Schaar et al., 2014). However, Nieukirk et al. (2012) and Klinck and Nieukirk (2012) could successfully observe the fin whale chorus in the mid and north Atlantic. It is thus very likely that a recorder array between Iceland and Svalbard, as described in the benchmark scenario in section 6.2.2, will be able to record the fin whale chorus.

Another question regarding the chorus received level is, how one best averages the spectrum used to estimate them. Especially if a recorder is close to vocalizing fin whales. Then it is necessary to include the energy of the impulsive calls into the power spectral density. The length of the recording from which the PSD is estimated, should be long enough to include the fin whale pulse train. The recording period should be longer than the inter pulse interval of vocalizing whale (± 12 s). Theoretically, the recording period should be long enough, to allow signals from all possible source locations to arrive at the recorder. In the North Atlantic it would take a signal around 15 minutes to propagate from Iceland to Svalbard (see section 5.3.1). It would thus be theoretically optimal to calculate the PSD from a 15 minute long recording. However, fin whale vocalizations are emitted as hour long, regular pulse trains. This enables recording periods shorter than 15 min. For example, using a 1 minute recording period is sufficient to estimate the received sound energy of all vocalizing whales.

7.2. Inversion of published fin index measurements

The inversed source pressure grids based on published fin index measurements are shown in figure 52. They indicate the likely distribution of vocalizing fin whales in January. The source grids indicates that fin whale calling activity mainly happens along shelf areas. The median source pressures grid suggests, that most calling activity occurs along the American coastline and near the Antilles. However, this estimate is considered very uncertain since there are no grid nodes with low uncertainty in the area. The prediction that fin whale calling occurs near the Antilles, agrees with acoustic detections from Clark (1995) and Watkins et al. (1987). They studied fin whale vocalizations using large scale military hydrophone arrays, and found that vocalizing fin whales moved from the Labrador Sea past Bermuda towards the Antilles. The median source grid also agrees with the fact that fin whale calling activity is reported to peak between September and January in the Gulf of Maine and St. Lawrence (Morano et al., 2012).

The maximum likelihood source grid does not cover the areas west of 60 degrees due to the large uncertainty of the grid nodes. It indicates that calling activity occurs in the Davis strait, along the Norwegian coast and off the Strait of Gibraltar. This agrees with the concept of distinct populations in the North Atlantic (Donovan, 1991, Bérubé et al., 1998). The presence of fin whale calling in the Norwegian sea, agrees with Clark (1995), who localized calling fin whales with a naval surveillance hydrophone array. Figure 53 shows the locations of calling fin whales. They agree surprisingly well with the inversion results. The prediction that fin whale calling activity is present in January in the Davis strait, is confirmed by Simon et al. (2010). Whereby the prediction that calling fin whales are located near the Strait of Gibraltar in winter, agrees with observations by Castellote et al. (2004). They found that in winter, some fin whales from the North Atlantic stock migrate through the strait of Gibraltar, into the Mediterranean.

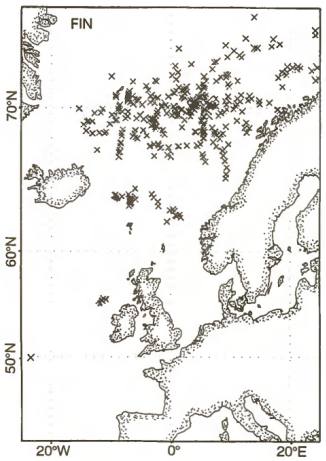

Figure 53: Locations of calling fin whales in winter 1993, from Clark (1995)

Although these inversion results were based on many assumptions (regarding the conversion from fin index to chorus received level), the patterns they indicate matched previous observations surprisingly well. It could be demonstrated that chorus inversion is

possible with a realizable number of recorders, and limited knowledge about the total source pressure. Applying the inversion method to a basin-scale recorder array, could outline the distribution and migration of vocalizing fin whales on an unprecedented scale.

7.3. Application of inversion method

This section discusses how the proposed method could be realized using different recorder technologies. The recorder array should be able to measure ambient noise spectra over long periods of time, synchronously and autonomously at multiple locations.

The simulation of randomly drifting recorders showed that using a drifting recorder array will have the drawback of limited operation time. After a certain period of time, likely a few months, the recorder are too dispersed for successful inversion. However, drifting recorders which are used for a few months only, could provide useful recordings. One of the main advantages of drifting recorders would be the reduction in cost and near real time data availability over satellites. Matsumoto et al. (2013) integrated hydrophone and recorder hardware into oceanographic floats and successfully managed to record marine mammal vocalizations and ambient noise spectra. Using drifting recorders has the additional advantage of reducing noise from mooring rope strumming. On the other hand, depending on the depth of the drifting recorder, the reception of a marine mammal chorus could be negatively affected by sea surface generated noise.

Other interesting data sources for marine mammal chorus inversion could be gliders (Rogers et al., 2004, Van Uffelen et al., 2013, Sagen et al., 2010b). They have the advantage of being able to navigate and send their data in near real-time (over satellites). A disadvantage is their high cost and operational effort. Future international projects involving interdisciplinary use of gliders, could provide valuable datasets for marine mammal chorus inversion.

A common way of recording underwater sound is to use moored recorders (Mellinger et al., 2007, Sagen et al., 2010a). These provide the advantage of long operating times and a fixed sensor location. Given the current progress in underwater recorder technology, it is likely that autonomous recording units will become sufficiently affordable to deploy large hydrophone arrays (Van Opzeeland et al., 2014, Dushaw et al., 2009). However, using moored recorders has the disadvantage of requiring ship time and technical personnel to deploy and recover them. Given the dimension of a recorder array necessary for basin-wide marine mammal chorus inversion, such a project would need to involve multiple vessels or expeditions. Multiple basin-wide mooring arrays already deployed in the world's oceans, mainly measuring temperature, salinity and currents (Sagen et al., 2010b). To create a basin-scale recorder array for fin whale chorus inversion, a useful strategy would be to add autonomous recording units to existing mooring arrays or other observation structures.

Another way to monitor ocean ambient noise and marine mammal choruses, could be to design a hybrid between a mooring and a float, which sends its recorded ambient noise spectra via satellite at the end of its lifetime. Compared to the expensive and sensitive instruments used to monitor salinity, temperature and currents in the ocean, hydrophones

are rather robust and affordable. A possible device to deliver data for marine mammal chorus inversion, could be similar to a lander or an ocean bottom seismometer. The system should be easy to deploy, consisting of a bottom weight, a release mechanism and a recording and data transmission unit. Once activated and deployed, it should run autonomously and record ambient noise spectra in regular intervals. After a preset time, the recording unit should release and rise to the surface to transmit its data. If only ambient noise spectra are sent, a one year dataset would be approximately 10 Mb (assuming 500 samples per spectrum and 4 spectra per day). This is well within the transmission capabilities of modern satellite networks (such as IRIDIUM). Although only usable once, such a system could prove environmentally friendly and cost efficient, since no ship time is required to recover it.

To record the marine mammal chorus in ice covered areas, which could be useful to investigate minke whale distribution (Risch et al., 2014, Menze, 2012), ice tethered platforms can be equipped with hydrophones (Sagen et al., 2010a). However, when measurements are made in ice covered areas, it might be necessary to include the effects of sea ice on transmission loss (Alexander et al., 2013).

In addition to estimating the distribution of vocalizing whales, the inversion method could be used to estimate the distribution of any type of sound sources generating a chorus-like signal. In marine ecosystems, not only marine mammals generate a chorus, but also snapping shrimp (Au, 1998, Versluis et al., 2000) and fish (Locascio and Mann, 2008, 2005). In fish, chorusing behavior has been associated to spawning (Au and Hastings, 2008). Monitoring the distribution of chorusing fish, could help identify spawning locations or migration patterns. Another application of the inversion method could be to monitor the distribution of anthropogenic noise sources, such as shipping or seismic surveys (Erbe et al., 2014).

The current implementation of the inversion algorithm in the Matlab computational environment allows easy manipulation of the code and visualization of the results. However, it is computationally slow compared to a direct implementation in C++ or Fortran. Rewriting the inversion algorithm in C++ could decrease the computational cost and dependency on third party software.

8. Conclusion

This thesis demonstrated that it is possible to estimate the distribution of vocalizing fin whales from a set of ambient noise spectra. Despite the extreme under-determinedness of this inverse problem, the parameter estimation algorithm correctly estimated the sound source distribution of different benchmark scenarios. The benchmark scenarios showed that the accuracy of the inversion method depends strongly on the number and distribution of recorders, and less on prior knowledge of fin whale calling behavior. The most promising results were that the inversion method tolerates high forward model uncertainty and an imperfect transmission loss matrix (that can be approximated using geometrical spreading). The inversion of data based on published fin whale chorus observations indicated realistic distribution patterns.

The main weakness of the inversion method is, that it can only give information on the distribution of vocalizing fin whales. Non-vocalizing whales will not be detected. It cannot replace visual surveys in determining animal abundance. Instead, the inversion method provides a new approach to monitor the distribution and migration of fin whales, complimenting existing visual and acoustic methods.

A. Acknowledgments

I would like to thank my supervisors Corinna Schrum, Hanne Sagen and Halvor Hobæk for their patience and guidance. Furthermore I would like to extent my thanks to everyone involved in the Joint Nordic Master in Marine Ecosystems and Climate. I truly enjoyed the last 2 years and could not have wished for a better study program.

I would not have come this far without the great support from my parents and whole family, thank you for the last 25 years! Keeping with me through thick and thin was Kjersti, who encouraged me to follow my own way. And when I needed a break, Hugo was the best friend to share problems and beers with, thank you both! For many enjoyable lunch breaks and helpful comments, I thank Steffi, Kjersti, Matthias and Hugo.

Much of the inspiration for this thesis has come from working with the ocean acoustics group of the Alfred Wegener Institute. I thank Olaf Boebel and the entire group for introducing me to the field. Understanding inverse problem theory and Bayesian inference would not have been possible for me without the great books and papers of the late Albert Tarantola.

B. Abbreviations

IPI Inter pulse interval

IWC International whaling commission

MCMC Monte Carlo Markov chain

NAMMCO North Atlantic Marine Mammal commission

PSD Power spectral density

RL Received level

RMS Root mean square

SL Source level

SNR Signal to noise ratio

SSE Sum of squared errors

TL Transmission loss

C. References

Alexander, P., Duncan, A., Bose, N., and Smith, D. (2013). Modelling acoustic transmission loss due to sea ice cover. *Acoustics Australia*, 41(1):79–87.

Allmaras, M., Bangerth, W., and Linhart, J. (2013). Estimating Parameters in Physical Models through Bayesian Inversion: A Complete Example. *SIAM Review*, 55(1):149–167.

Amante, C. and Eakins, B. (2009). ETOPO1 1 Arc-Minute Global Relief Model: Procedures, Data Sources and Analysis. *NOAA Technical Memorandum NESDIS NGDC-24*, page 19.

Andrew, R. K., Howe, B. M., and Mercer, J. a. (2011). Long-time trends in ship traffic noise for four sites off the North American West Coast. *The Journal of the Acoustical Society of America*, 129(2):642–51.

Au, W. W. L. (1998). The acoustics of the snapping shrimp Synalpheus parneomeris in Kaneohe Bay. *The Journal of the Acoustical Society of America*, 103(1):41.

Au, W. W. L. and Hastings, M. C. (2008). *Principles of Marine Bioacoustics*. Springer US, New York, NY.

Ballard, M. S. (2012). Modeling three-dimensional propagation in a continental shelf environment. *The Journal of the Acoustical Society of America*, 131(3):1969–77.

Bérubé, M., Aguilar, a., Dendanto, D., Larsen, F., Notarbartolo di Sciara, G., Sears, R., Sigurjónsson, J., Urban-R, J., and Palsbø ll, P. J. (1998). Population genetic structure of North Atlantic, Mediterranean Sea and Sea of Cortez fin whales, Balaenoptera physalus (Linnaeus 1758): analysis of mitochondrial and nuclear loci. *Molecular ecology*, 7(5):585–99.

Borda, M. (2011). *Fundamentals in Information theory and coding*. Springer, Berlin-Heidelberg.

Burtenshaw, J. C., Oleson, E. M., Hildebrand, J. a., McDonald, M. a., Andrew, R. K., Howe, B. M., and Mercer, J. a. (2004). Acoustic and satellite remote sensing of blue whale seasonality and habitat in the Northeast Pacific. *Deep Sea Research Part II: Topical Studies in Oceanography*, 51(10-11):967–986.

Carey, W. M. and Evans, R. B. (2011). *Ocean Ambient Noise*. Springer New York, New York, NY.

Castellote, M., Clark, C. W., and Lammers, M. O. (2004). Population identity and migration movements of fin whales (Balaenoptera physalus) in the Mediterranean Sea and Strait of Gibraltar. *Journal of Cetacean Research and Management*, pages 1–16.

Clark, C. W. (1995). The application of US Navy underwater hydrophone arrays for scientific research on whales. *Forty-Fith report of the International whaling commsion*, 9:210–212.

Corkeron, P. J. and Connor, R. C. (1999). Why do baleen whales migrate? *Marine Mammal Science*, 15(4):1228–1245.

Cressey, D. (2015). World's whaling slaughter tallied. *Nature*, 519:140–141.

Croll, D. A., Clark, C. W., Acevedo, A., Tershy, B., Flores, S., Gedamke, J., and Urban, J. (2002). Only male fin whales sing loud songs. *Nature*, 417(6891):809.

Curtis, K. R., Howe, B. M., and Mercer, J. a. (1999). Low-frequency ambient sound in the North Pacific: Long time series observations. *The Journal of the Acoustical Society of America*, 106(6):3189.

Delarue, J., Todd, S. K., Van Parijs, S. M., and Di Iorio, L. (2009). Geographic variation in Northwest Atlantic fin whale (Balaenoptera physalus) song: implications for stock structure assessment. *The Journal of the Acoustical Society of America*, 125(3):1774–82.

Diachok, O. (1980). Arctic hydroacoustics. *Cold Regions Science and Technology*, 2(1963):186–201.

Donovan, G. P. (1991). A review of IWC stock boundaries. *Rept Int Whal Commn Special*, 1946(13):39–68.

Dorigo, M., Birattari, M., and Stützle, T. (2006). Ant colony optimization. *IEEE Computational Intelligence Magazine*, 1(4):28–39.

Duennebier, F. K., Lukas, R., Nosal, E.-M., Aucan, J., and Weller, R. a. (2012). Wind, waves, and acoustic background levels at Station ALOHA. *Journal of Geophysical Research*, 117(C3):C03017.

Dushaw, B., Au, W., Beszczynska-Möller, A., Brainard, R., Cornuelle, B. D., Gould, J., Howe, B., Jayne, S. R., Johannessen, O. M., Lynch, J. F., Martin, D., Menemenlis, D., Mikhalevsky, P., Miller, J. H., and Wunsch, C. (2009). A global ocean acoustic observing network. In *OceanObs '09*, number 1, page 13.

Dushaw, B. D., Worcester, P. F., Dzieciuch, M. A., and Menemenlis, D. (2013). On the time-mean state of ocean models and the properties of long range acoustic propagation. *Journal of Geophysical Research: Oceans*, 118(9):4346–4362.

Dziak, R. P., Bohnenstiehl, D. R., Stafford, K. M., Matsumoto, H., Park, M., Lee, W. S., Fowler, M. J., Lau, T.-K., Haxel, J. H., and Mellinger, D. K. (2015). Sources and Levels of Ambient Ocean Sound near the Antarctic Peninsula. *Plos One*, 10(4):e0123425.

Erbe, C., Williams, R., Sandilands, D., and Ashe, E. (2014). Identifying modeled ship noise hotspots for marine mammals of Canada's Pacific region. *PloS one*, 9(3):e89820.

Falk-Petersen, S., Pavlov, V., Berge, J. r., Cottier, F., Kovacs, K. M., and Lydersen, C. (2015). At the rainbow's end: high productivity fueled by winter upwelling along an Arctic shelf. *Polar Biology*, 38:5–11.

Francois, R. E. and Garrison, G. R. (1982). Sound absorption based on ocean measurements. Part II: Boric acid contribution and equation for total absorption. *The Journal of the Acoustical Society of America*, 72:1879.

Frisk, G. V. (2012). Noiseonomics: the relationship between ambient noise levels in the sea and global economic trends. *Scientific reports*, 2(1):437.

Gavrilov, A. N., McCauley, R. D., and Gedamke, J. (2012). Steady inter and intra-annual decrease in the vocalization frequency of Antarctic blue whales. *The Journal of the Acoustical Society of America*, 131(6):4476–80.

Gedamke, J., Gales, N., Hildebrand, J., and Wiggins, S. (2007). Seasonal occurrence of low frequency whale vocalisations across eastern Antarctic and southern Australian waters , February 2004 to February 2007. *Rep Int Whal Commn*, SC/59/SH5(February 2004):1–11.

Gervaise, C., Simard, Y., Roy, N., Kinda, B., and Ménard, N. (2012). Shipping noise in whale habitat: characteristics, sources, budget, and impact on belugas in Saguenay-St. Lawrence Marine Park hub. *The Journal of the Acoustical Society of America*, 132(1):76–89.

Goldbogen, J., Pyenson, N., and Shadwick, R. (2007). Big gulps require high drag for fin whale lunge feeding. *Marine Ecology Progress Series*, 349:289–301.

Goldbogen, J. a., Calambokidis, J., Oleson, E., Potvin, J., Pyenson, N. D., Schorr, G., and Shadwick, R. E. (2011). Mechanics, hydrodynamics and energetics of blue whale lunge feeding: efficiency dependence on krill density. *The Journal of experimental biology*, 214(Pt 1):131–46.

Goldbogen, J. a., Stimpert, A. K., Deruiter, S. L., Calambokidis, J., Friedlaender, A. S., Schorr, G. S., Moretti, D. J., Tyack, P. L., and Southall, B. L. (2014). Using accelerometers to determine the calling behavior of tagged baleen whales. *The Journal of experimental biology*, (May).

Granville, V., Krivanek, M., and Rasson, J. P. (1994). Simulated annealing: a proof of convergence. *IEEE Transactions on Pattern Analysis and Machine Intelligence*, 16(6):652–656.

Hammond, P. S., Macleod, K., Gillespie, D., Swift, R., Winship, A., Burt, M. L., Cañadas, A., Vázquez, J. A., Ridoux, V., Certain, G., Van Canneyt, O., Lens, S., Santos, M. B. n., Rogan, E., Uriarte, A., Hernández, C., and Castro, R. (2009). Cetacean Offshore Distribution and Abundance in the European Atlantic (CODA). Technical report.

Heaney, K. D., Campbell, R. L., and Murray, J. J. (2012). Comparison of hybrid three-dimensional modeling with measurements on the continental shelf. *The Journal of the Acoustical Society of America*, 131(2):1680–8.

Heaney, K. D., Campbell, R. L., and Snellen, M. (2013). Long range acoustic measurements of an undersea volcano. *The Journal of the Acoustical Society of America*, 134(4):3299–306.

Helble, T. a., D'Spain, G. L., Campbell, G. S., and Hildebrand, J. a. (2013a). Calibrating passive acoustic monitoring: correcting humpback whale call detections for site-specific and time-dependent environmental characteristics. *The Journal of the Acoustical Society of America*, 134(5):EL400–6.

Helble, T. a., D'Spain, G. L., Hildebrand, J. a., Campbell, G. S., Campbell, R. L., and Heaney, K. D. (2013b). Site specific probability of passive acoustic detection of humpback whale calls from single fixed hydrophones. *The Journal of the Acoustical Society of America*, 134(3):2556–70.

Herman, L. M., Pack, A. a., Spitz, S. S., Herman, E. Y. K., Rose, K., Hakala, S., and Deakos, M. H. (2013). Humpback whale song: who sings? *Behavioral Ecology and Sociobiology*, 67(10):1653–1663.

Hope, G. (2013). Exploring the Microseismicity of the Gakkel Ridge from Arctic Sea Ice. *Master thesis*, (June):154 p.

Hovem, J. and Korakas, A. (2014). Modeling Low-Frequency Anthropogenic Noise in the Oceans: A Comparison of Propagation Models. *Marine Technology Society Journal*, 48(2).

Hovem, J. M. (2013). Ray Trace Modeling of Underwater Sound Propagation. *Modeling and Measurement Methods for Acoutic Waves and for Acoustic Microdevices*.

Ingram, S. N., Walshe, L., Johnston, D., and Rogan, E. (2007). Habitat partitioning and the influence of benthic topography and oceanography on the distribution of fin and minke whales in the Bay of Fundy, Canada. *Journal of the Marine Biological Association of the UK*, 87(01):149.

IWC (2015). Whale Population Estimates - The International Whaling Commission's most recent information on estimated abundance. *https://iwc.int/estimate*, acessed 02.05.2015.

Joiris, C. R., Falck, E., D'Hert, D., Jungblut, S., and Boos, K. (2014). An important late summer aggregation of fin whales Balaenoptera physalus, little auks Alle alle and Brünnich's guillemots Uria lomvia in the eastern Greenland Sea and Fram Strait: influence of hydrographic structures. *Polar Biology*, pages 1645–1657.

Kirkpatrick, S., Gelatt, C. D., and Vecchi, M. P. (1982). Optimization by simulated annealing. *Science*, 220(4598):671–680.

Klinck, H. and Nieukirk, S. (2012). Seasonal presence of cetaceans and ambient noise levels in polar waters of the North Atlantic. *The Journal of the Acoustical Society of America: Express Letters*, 132(3):176–181.

Küsel, E. T., Mellinger, D. K., Thomas, L., Marques, T. a., Moretti, D., and Ward, J. (2011). Cetacean population density estimation from single fixed sensors using passive acoustics. *The Journal of the Acoustical Society of America*, 129(6):3610–22.

Locascio, J. V. and Mann, D. a. (2005). Effects of Hurricane Charley on fish chorusing. *Biology letters*, 1(3):362–365.

Locascio, J. V. and Mann, D. a. (2008). Diel Periodicity of Fish Sound Production in Charlotte Harbor, Florida. *Transactions of the American Fisheries Society*, 137(2):606–615.

Lurton, X. (2002). *An Introduction to Underwater Acoustics: Principles and Applications*. Springer Praxis Books. Springer.

Mann, K. and Lazier, J. (2013). *Dynamics of Marine Ecosystems: Biological-Physical Interactions in the Oceans*. Wiley.

Marques, T. (2009). Distance sampling: Estimating animal density. *Significance*, 6(3):136–137.

Marques, T., Munger, L., Thomas, L., Wiggins, S., and Hildebrand, J. (2011). Estimating North Pacific right whale Eubalaena japonica density using passive acoustic cue counting. *Endangered Species Research*, 13(3):163–172.

Marques, T. a., Thomas, L., Martin, S. W., Mellinger, D. K., Ward, J. a., Moretti, D. J., Harris, D., and Tyack, P. L. (2013). Estimating animal population density using passive acoustics. *Biological reviews of the Cambridge Philosophical Society*, 88(2):287–309.

Martin, S. W., Marques, T. a., Thomas, L., Morrissey, R. P., Jarvis, S., DiMarzio, N., Moretti, D., and Mellinger, D. K. (2013). Estimating minke whale (Balaenoptera acutorostrata) boing sound density using passive acoustic sensors. *Marine Mammal Science*, 29(1):142–158.

Mate, B. R., Ilyashenko, V. Y., Bradford, A. L., Vertyankin, V. V., Tsidulko, G. A., Rozhnov, V. V., and Irvine, L. M. (2015). Critically endangered western gray whales migrate to the eastern North Pacific. *Biology letters*, 11(20150071).

Matsumoto, H., Jones, C., Klinck, H., Mellinger, D. K., Dziak, R. P., and Meinig, C. (2013). Tracking beaked whales with a passive acoustic profiler float. *Journal of the Acoustical Society of America*, 133(2):731–740.

Mauritzen, M., Skaug, H. J., and Øien, N. (2004). Combining line transects, environmental data and GIS: cetacean distributions and habitat and prey selection along the Barents Sea shelf edge. 7:40pp.

McDonald, M. and Fox, C. (1999). Passive acoustic methods applied to fin whale population density estimation. *The Journal of the Acoustical Society of America*, 105(5):2643–2651.

Mellinger, D., Stafford, K., Moore, S., Dziak, R., and Matsumoto, H. (2007). An Overview of Fixed Passive Acoustic Observation Methods for Cetaceans. *Oceanography*, 20(4):36–45.

Menze, S. (2012). Passive acoustic monitoring of ambient noise in the Atlantic sector of the Southern Ocean. *Bachelor thesis at the University of applied Sciences Bremerhaven*, pages 1–87.

Metropolis, N., Rosenbluth, A. W., Rosenbluth, M. N., Teller, A. H., and Teller, E. (1953). Equation of State Calculations by Fast Computing Machines. *The Journal of Chemical Physics*, 21(6):1087–1092.

Mikhalevsky, P. N., Sagen, H., Worcester, P. F., Baggeroer, A. B., Orcutt, J., Moore, S. E., Lee, C. M., Vigness-Raposa, K. J., Freitag, L., Arrott, M., Atakan, K., Beszczynska-Möller, A., Duda, T. F., Dushaw, B. D., Gascard, J. C., Gavrilov, A. N., Keers, H., Morozov, A. K., Munk, W. H., Rixen, M., Sandven, S., Skarsoulis, E., Stafford, K. M., Vernon, F., and Yuen, M. Y. (2015). Multipurpose Acoustic Networks in the Integrated Arctic Ocean Observing System. *ARCTIC*, 68(5):17.

Mizroch, S. a., Rice, D. W., Zwiefelhofer, D., Waite, J., and Perryman, W. L. (2009). Distribution and movements of fin whales in the North Pacific Ocean. *Mammal Review*, 39(3):193–227.

Moore, S. E., Stafford, K. M., Melling, H., Berchok, C., Wiig, O. y., Kovacs, K. M., Lydersen, C., and Richter-Menge, J. (2011). Comparing marine mammal acoustic habitats in Atlantic and Pacific sectors of the High Arctic: year-long records from Fram Strait and the Chukchi Plateau. *Polar Biology*, 35(3):475–480.

Morano, J. L., Salisbury, D. P., Rice, A. N., Conklin, K. L., Falk, K. L., and Clark, C. W. (2012). Seasonal and geographical patterns of fin whale song in the western North Atlantic Ocean. *The Journal of the Acoustical Society of America*, 132(2):1207.

Mosegaard, K. and Sambridge, M. (2002). Monte Carlo analysis of inverse problems. *Inverse Problems*, 18:29–54.

Mosegaard, K. and Vestergaard, P. D. (1991). A simulated annealing approach to seismic model optimization with sparse prior information. *Geophysical Prospecting*, 39:599–611.

NAMMCO (2015). The fin whale - Status of Marine Mammals in the North Atlantic. Technical report.

Newhall, A. E., Lin, Y.-T., Lynch, J. F., Baumgartner, M. F., and Gawarkiewicz, G. G. (2012). Long distance passive localization of vocalizing sei whales using an acoustic normal mode approach. *The Journal of the Acoustical Society of America*, 131(2):1814.

Nichols, R. (2005). Some notable noises: Monsters and machines. *IEEE Journal of Oceanic Engineering*, 30(2):248–256.

Nieukirk, S. L., Mellinger, D. K., Moore, S. E., Klinck, K., Dziak, R. P., and Goslin, J. (2012). Sounds from airguns and fin whales recorded in the mid-Atlantic Ocean, 1999-2009. *The Journal of the Acoustical Society of America*, 131(2):1102–12.

Notarbartolo-di Sciara, G., Zanardelli, M., Jahoda, M., Panigada, S., and Airoldi, S. (2003). The fin whale Balaenoptera physalus (L. 1758) in the Mediterranean Sea. *Mammal Review*, 33(2):105–150.

Øien, N. (2004). Distribution and abundance of large whales in Norwegian and adjacent waters based on ship surveys. *NAMMCO Scientific Publications*, 7:31–48.

Oleson, E. and Calambokidis, J. (2007). Behavioral context of call production by eastern North Pacific blue whales. *Marine Ecology Progress Series*, 330:269–284.

Oleson, E. M., Bayless, A. R., and Hildebrand, J. a. (2014). Seasonal Evolution of Fin Whale Song in the Eastern North Pacific Fin Whale Calls. *PloS one*, 9(12):e115678.

Payne, R. and Webb, D. (1971). Orientation by means of long range signaling in baleen whales. *Annals of the New York Academy of Sciences*, 199:110–141.

Perrin, W. F., Würsig, B. G., and Thewissen, J. G. M. (2009). *Encyclopedia of marine mammals*. Elsevier, 2 edition.

Porter, M. and Liu, Y. (1994). Finite Element Ray Tracing. *Theoretical and computational acoustics*, 2:947–956.

Porter, M. B. and Bucker, H. P. (1987). Gaussian beam tracing for computing ocean acoustic fields. *The Journal of the Acoustical Society of America*, 82(4):1349–1359.

Rettig, S., Boebel, O., Menze, S., Kindermann, L., Thomisch, K., and Van Opzeeland, I. (2013). Local to basin scale arrays for passive acoustic monitoring in the Atlantic sector of the Southern Ocean. In *1st International Conference and Exhibition on Underwater Acoustics*, pages 1669–1674.

Risch, D., Gales, N. J., Gedamke, J., Kindermann, L., Nowacek, D. P., Read, A. J., Siebert, U., Van Opzeeland, I. C., Van Parijs, S. M., and Friedlaender, A. S. (2014). Mysterious bio-duck sound attributed to the Antarctic minke whale (Balaenoptera bonaerensis). *Biology Letters*, 10(4):20140175.

Rocha, Jr., R. C., Clapham, P. J., and Ivashchenko, Y. (2015). Emptying the Oceans: A Summary of Industrial Whaling Catches in the 20th Century. *Marine Fisheries Review*, 76(4):37–48.

Rogers, E., JG, G. J. G., Smith, W., Denny, G., and Farley, P. (2004). Underwater acoustic glider. *IGARSS 2004. 2004 IEEE International Geoscience and Remote Sensing Symposium*, 3(c):2241–2244.

Sagen, H., Sandven, S., Beszczynska-Moeller, A., Boebel, O., Duda, T. F., Gascard, J. C., Gavrilov, A. N., Lee, C. M., Mellinger, D. K., Peter, N., Moore, S. E., Morozov, A. K., Rixen, M., Skarsoulis, E., Stafford, M., Tveit, E., and Worcester, P. F. (2010a). Acoustic technologies for observing the interior of the arctic ocean. In *Ocean Obs´09: Sustained Ocean Observations and Information for Society Conference (Annex)*, number 1.

Sagen, H., Sandven, S., Worcester, P., Beszczynska-moller, A., and Morozov, A. (2010b). The Fram Strait acoustic system for tomography, navigation and passive listening. In *Proceedings of the "Ocean Obs09: Sustained Ocean Observations and Information for Society" Conference*.

Sagen, H., Sandven, S., Worcester, P., Dzieciuch, M., and Skarsoulis, E. (2008). The Fram Strait acoustic tomography system. In *Acoustics08 Conference*.

Shannon, C. E. (1948). A mathematical theory of communication. *The Bell System Technical Journal*, 27:379–423.

Silva, M. a., Prieto, R., Cascão, I., Seabra, M. I., Machete, M., Baumgartner, M. F., and Santos, R. S. (2014). Spatial and temporal distribution of cetaceans in the mid-Atlantic waters around the Azores. *Marine Biology Research*, 10(2):123–137.

Silva, M. a., Prieto, R., Jonsen, I., Baumgartner, M. F., and Santos, R. S. (2013). North Atlantic blue and fin whales suspend their spring migration to forage in middle latitudes: building up energy reserves for the journey? *PloS one*, 8(10):e76507.

Simon, M., Stafford, K. M., Beedholm, K., Lee, C. M., and Madsen, P. T. (2010). Singing behavior of fin whales in the Davis Strait with implications for mating, migration and foraging. *The Journal of the Acoustical Society of America*, 128(5):3200–3210.

Sirović, A., Hildebrand, J. A., and Wiggins, S. M. (2007). Blue and fin whale call source levels and propagation range in the Southern Ocean. *The Journal of the Acoustical Society of America*, 122(2):1208–1215.

Smith, S. (2003). *Digital signal processing: a practical guide for engineers and scientists*. Newnes.

Snieder, R. and Trampert, J. (1999). Inverse Problems in Geophysics. In *Wavefield inversion*, pages 119–190. Springer New York.

Sturm, F., Ivansson, S., Jiang, Y.-M., and Chapman, N. R. (2008). Numerical investigation of out-of-plane sound propagation in a shallow water experiment. *The Journal of the Acoustical Society of America*, 124(6):341–346.

Tarantola, A. (2004). *Inverse Problem Theory and Methods for Model Parameter Estimation*. SIAM.

Tarantola, A. (2006). Popper, Bayes and the inverse problem. *Nature Physics*, 2:492–494.

Teanby, N. A. (2006). An icosahedron-based method for even binning of globally distributed remote sensing data. *Computers and Geosciences*, 32:1442–1450.

Thomas, L., Buckland, S. T., Burnham, K. P., Anderson, D. R., Laake, J. L., Borchers, D. L., and Strindberg, S. (2006). Distance sampling. In *Encyclopedia of Environmetrics*, volume 1, pages 544–552.

Towsey, M., Wimmer, J., Williamson, I., and Roe, P. (2013). The use of acoustic indices to determine avian species richness in audio-recordings of the environment. *Ecological Informatics*, 21(100):110–119.

Urick, R. J. (1983). *Principles of underwater sound*. McGraw-Hill.

Valtierra, R. D., Glynn Holt, R., Cholewiak, D., and Van Parijs, S. M. (2013). Calling depths of baleen whales from single sensor data: development of an autocorrelation method using multipath localization. *The Journal of the Acoustical Society of America*, 134(3):2571–81.

Van Der Schaar, M., Ainslie, M. a., Robinson, S. P., Prior, M. K., and André, M. (2014). Changes in 63Hz third-octave band sound levels over 42 months recorded at four deep-ocean observatories. *Journal of Marine Systems*, 130:4–11.

Van Opzeeland, I., Samaran, F., Stafford, K., Findlay, K., Gedamke, J., Harris, D., and Miller, B. (2014). Towards collective circum-Antarctic passive acoustic monitoring: The Southern Ocean Hydrophone Network (SOHN). *Polarforschung*, 83(2):47–61.

Van Opzeeland, I. V. (2010). Acoustic ecology of marine mammals in polar oceans. *Berichte zur Polar-und Meeresforschung*, 619.

Van Parijs, S., Clark, C., Sousa-Lima, R., Parks, S., Rankin, S., Risch, D., and Van Opzeeland, I. (2009). Management and research applications of real-time and archival passive acoustic sensors over varying temporal and spatial scales. *Marine Ecology Progress Series*, 395:21–36.

Van Uffelen, L. J., Nosal, E.-M., Howe, B. M., Carter, G. S., Worcester, P. F., Dzieciuch, M. a., Heaney, K. D., Campbell, R. L., and Cross, P. S. (2013). Estimating uncertainty in subsurface glider position using transmissions from fixed acoustic tomography sources. *The Journal of the Acoustical Society of America*, 134(4):3260–71.

Versluis, M., Schmitz, B., von der Heydt, A., and Lohse, D. (2000). How snapping shrimp snap: through cavitating bubbles. *Science*, 289(5487):2114–2117.

Víkingsson, G. a., Pike, D. G., Desportes, G., Ø ien, N., Gunnlaugsson, T., and Bloch, D. (2013). Distribution and abundance of fin whales (Balaenoptera physalus) in the Northeast and Central Atlantic as inferred from the North Atlantic Sightings Surveys 1987-2001. *NAMMCO Scientific Publications*, 7:49–72.

Širović, A., Hildebrand, J. a., Wiggins, S. M., McDonald, M. a., Moore, S. E., and Thiele, D. (2004). Seasonality of blue and fin whale calls and the influence of sea ice in the Western Antarctic Peninsula. *Deep Sea Research Part II: Topical Studies in Oceanography*, 51(17-19):2327–2344.

Ward, J. a., Thomas, L., Jarvis, S., DiMarzio, N., Moretti, D., Marques, T. a., Dunn, C., Claridge, D., Hartvig, E., and Tyack, P. (2012). Passive acoustic density estimation of sperm whales in the Tongue of the Ocean, Bahamas. *Marine Mammal Science*, 28(4):E444–E455.

Waring, G. T., Nø ttestad, L., Olsen, E., Skov, H., and Vikingsson, G. (2008). Distribution and density estimates of cetaceans along the mid-Atlantic Ridge during summer 2004. *Journal of Cetacean Research and Management*, 10(2):137–146.

Watkins, W., Daher, M. A., Reppucci, G., George, J., Martin, D., DiMarzio, N., and Gannon, D. (2000). Seasonality and Distribution of Whale Calls in the North Pacific. *Oceanography*, 13(1):62–67.

Watkins, W. A., Tyack, P., Moore, K. E., and Bird, J. E. (1987). The 20-Hz signals of finback whales (Balaenoptera physalus). *Journal of the Acoustical Society of America*, 82(6):1901–1912.

Weirathmueller, M. J., Wilcock, W. S. D., and Soule, D. C. (2013). Source levels of fin whale 20 Hz pulses measured in the Northeast Pacific Ocean. *The Journal of the Acoustical Society of America*, 133(2):741–9.

Welch, P. (1967). The use of fast Fourier transform for the estimation of power spectra: a method based on time averaging over short, modified periodograms. *IEEE Transactions on audio and electroacoustics*, (2):70–73.

Wenz, G. M. (1962). Acoustic Ambient Noise in the Ocean: Spectra and Sources. *The Journal of the Acoustical Society of America*, 34(12):1936–1956.

Wilcock, W. S. D. (2012). Tracking fin whales in the northeast Pacific Ocean with a seafloor seismic network. *The Journal of the Acoustical Society of America*, 132(4):2408–2419.

D. List of Figures

E. List of Tables

F. Matlab code

Listing 1: Simulated annealing parameter estimation function

```
function sa_parameter_estimation(n_iterations,n_solutions,t_exponent,p_min,
    p_max,sim_source_location,recorder_location,true_rl_file,TL_db,sigma_db,
    target_file)

% SIMULATED ANNEALING PARAMETER ESTIMATION FUNCETION
% by Sebastian Menze, 2015
% used to invert fin whale chorus received level observations
% to most likely source grid pattern
%
% inputs:
%   number of iterations, number of solutions, cooling exponent,
%   minimum total pressure, maxiumim total pressure, pathto soiulated source
%   grid file, path to recorder location file, path to received level file,
%   transmission loss matrix, forward model standard deviation, name of
%   outpit fie
%
% outputs:
%   solutions matrix in uPa [columns: number of solution , rows: number of
    source grid nodes]
%   solutions matrix in dB re 1 uPa [columns: number of solution , rows: number
     of source grid nodes]
%   vector from 1 : number of iterations
%   misfit matrix [columns: number of solutions, rows: number of iterations]
%   likelihood matrix [columns: number of solutions, rows: number of iterations
    ]

% read source grid node locations
[sim_source_id,sim_source_lat,sim_source_lon] = import_loc_file(
    sim_source_location) ;
n_sim_whale=sim_source_id(end);
n_source_locations=sim_source_id(end);
```

```
% read recorder positions
% recorder_location='recorder_location_files/recorders_geodesic_47.loc';
[recorders_id,recorders_lat,recorders_lon] = import_loc_file(recorder_location)
    ;

% read true rl
% true_rl_file='true_source_files/tl_cylindrical_ts_gauss_r47.rl';
[true_rl_id,true_rl_p,true_rl_db] = import_true_rl(true_rl_file) ;

% place one simulated source on each node and generate homogenous a priori
   source
% grids between the minimum and maximum total pressure
sim_whale_location_old_all=repmat(sim_source_id',n_solutions,1) ;
if p_min<0
    p_min=0;
end
p_sim_whale=linspace(p_min,p_max,n_solutions);
p_sim_whale=p_sim_whale/n_sim_whale;

%%% use simulated annealing
t_start=1;

for i_iteration=1:n_iterations

    tic
    % update temperature
    temp= t_start*(1-(i_iteration)./n_iterations).^t_exponent;
    mu=temp;

    sim_whale_location_old_all_new=[];
    p_sim_whale_par=[];
        p_sim_whale_par_all=[];

    parfor i_solution=1:n_solutions


  %%% move random sim_whale to random new loation
  ix_selected_sim_whale=randi(n_sim_whale);
  new_location=randi(n_source_locations);

   sim_whale_location_old=sim_whale_location_old_all(i_solution,1:n_sim_whale);

%  clear sim_whale_location_new
  sim_whale_location_new=sim_whale_location_old;
  sim_whale_location_new(ix_selected_sim_whale)=new_location;

  %%% calculate new pressure
p_sim_whale_par=p_sim_whale(i_solution);
[pressure_new]=parfor_pressure_helper(n_source_locations,sim_whale_location_new
    ,p_sim_whale_par)
[pressure_old]=parfor_pressure_helper(n_source_locations,sim_whale_location_old
    ,p_sim_whale_par)

% new misfit and likelihood
[p_received,db_received]=received_pressure(pressure_new,TL_db) ;
 sse_new = 0.5 * sum(  ((db_received' - true_rl_db).^2) ./ (sigma_db^2)   );
likelihood_new= exp( - sse_new ) ;
```

```
 % old misfit and likelihood
[p_received,db_received]=received_pressure(pressure_old,TL_db)
 sse_old = 0.5 * sum(  ((db_received' - true_rl_db).^2) ./ (sigma_db^2)   );
likelihood_old= exp( - sse_old ) ;

if likelihood_new==0
   if sse_new <=  sse_old
% move sim_whale
       sim_whale_location_old(ix_selected_sim_whale)=new_location;
   else
       if  random('exp',mu)>1
       sim_whale_location_old(ix_selected_sim_whale)=new_location;
       end
   end
else
   if likelihood_old <= likelihood_new
% move sim_whale
       sim_whale_location_old(ix_selected_sim_whale)=new_location;
   else
       if  random('exp',mu)>1
       sim_whale_location_old(ix_selected_sim_whale)=new_location;
       end
   end
end

     % update simulates source locations and likelihood values due to
     % parfor constraints
     performance_sse(i_iteration,i_solution)=sse_old;
     performance_likelihood(i_iteration,i_solution)=likelihood_old;
     sim_whale_location_old_all_new= [sim_whale_location_old_all_new;
         sim_whale_location_old ];
     p_sim_whale_par_all=[p_sim_whale_par_all,p_sim_whale_par];

    end

    p_sim_whale=p_sim_whale_par_all;
    sim_whale_location_old_all=sim_whale_location_old_all_new;
    performance_iteration(i_iteration)=i_iteration;


disp(['done: ',num2str(i_iteration/n_iterations*100),'% and mean L(m): ',
    num2str((mean(performance_likelihood(i_iteration,:)))),' mean S(m): ',
    num2str((mean(performance_sse(i_iteration,:)))),' dB'])
toc

end

% calculate source grid based on the source locations obtained from
% simulated annealing
    for i_solution=1:n_solutions
for i_hexagonal_source=1:n_source_locations
solutions_p(i_solution,i_hexagonal_source)=sum(sim_whale_location_old_all(
    i_solution,:)==i_hexagonal_source)*p_sim_whale(i_solution) ;
end
end

 solutions_db=20.*log10((solutions_p));
 solutions_db(solutions_db<0)=0;
```

```
 % save results as mat file
 save(target_file,'solutions_p','solutions_db','performance_iteration','
     performance_likelihood','performance_sse','p_sim_whale')

end
```

Listing 2: Function to calculate the source pressure of a grid node

```
function [pressure]=parfor_pressure_helper(n_source_locations,
    sim_whale_location,p_sim_whale)
%
% function to calculate the pressure at each grid node based on how many
    siumatled
% source reside on it
%
% by Sebastian Menze, 2015
%
for i_hexagonal_source=1:n_source_locations
pressure(i_hexagonal_source)=sum(sim_whale_location==i_hexagonal_source)*
    p_sim_whale ;
end
end
```

Listing 3: Function to calculate received level from a source pressure vector and a TL matrix

```
function [p_received,db_received]=received_pressure(p_vector,TL_matrix)

% function to calculate the received pressure at a set of recorders
% by Sebastian Menze, 2015
%
% inputs: source pressure vector and the transmission loss matrix connecting
% sources and receivers
%
% outpus: received pressure in uPa dB and received level in dB re 1 uPa

for i_receiver=1:size(TL_matrix,2)

    for i_source=1:size(TL_matrix,1)

        single_source_RL= 20*log10(p_vector(i_source)) + TL_matrix(i_source,
            i_receiver) ;
        if single_source_RL < 0
             received_db(i_source)=0 ;
        else
             received_db(i_source)=single_source_RL ;
        end
            clear single_source_RL
    end

      p_received(i_receiver)=sum(10.^(received_db/20));
      db_received(i_receiver)=  20*log10(p_received(i_receiver));
     clear received_db
end
```

```
end
```

Listing 4: Location file import function

```
function [ID,latitude,longitude,depth] = import_loc_file(filename, startRow
    , endRow)
%IMPORTFILE Import numeric data from a text file as column vectors.
%   [ID,LATITUDE,LONGITUDE,DEPTH] = IMPORTFILE(FILENAME) Reads data from
%   text file FILENAME for the default selection.
%
%   [ID,LATITUDE,LONGITUDE,DEPTH] = IMPORTFILE(FILENAME, STARTROW, ENDROW)
%   Reads data from rows STARTROW through ENDROW of text file FILENAME.
%
% Example:
%   [ID,latitude,longitude,depth] =
%   importfile('recorders_geodesic_3.loc',2, 4);
%
%    See also TEXTSCAN.

% Auto-generated by MATLAB on 2015/02/17 16:35:39

%% Initialize variables.
delimiter = ' ';
if nargin<=2
    startRow = 2;
    endRow = inf;
end

%% Format string for each line of text:
%   column1: double (%f)
%   column2: double (%f)
%   column3: double (%f)
%   column4: double (%f)
% For more information, see the TEXTSCAN documentation.
formatSpec = '%f%f%f%f%[^\n\r]';

%% Open the text file.
fileID = fopen(filename,'r');

%% Read columns of data according to format string.
% This call is based on the structure of the file used to generate this
% code. If an error occurs for a different file, try regenerating the code
% from the Import Tool.
dataArray = textscan(fileID, formatSpec, endRow(1)-startRow(1)+1, 'Delimiter',
    delimiter, 'MultipleDelimsAsOne', true, 'HeaderLines', startRow(1)-1, '
    ReturnOnError', false);
for block=2:length(startRow)
    frewind(fileID);
    dataArrayBlock = textscan(fileID, formatSpec, endRow(block)-startRow(block)
        +1, 'Delimiter', delimiter, 'MultipleDelimsAsOne', true, 'HeaderLines',
         startRow(block)-1, 'ReturnOnError', false);
    for col=1:length(dataArray)
        dataArray{col} = [dataArray{col};dataArrayBlock{col}];
    end
end
```

```
%% Close the text file.
fclose(fileID);

%% Post processing for unimportable data.
% No unimportable data rules were applied during the import, so no post
% processing code is included. To generate code which works for
% unimportable data, select unimportable cells in a file and regenerate the
% script.

%% Allocate imported array to column variable names
ID = dataArray{:, 1};
latitude = dataArray{:, 2};
longitude = dataArray{:, 3};
depth = dataArray{:, 4};
```

Listing 5: Received level file import function

```
function [true_rl_id,true_rl_p,true_rl_db] = import_true_rl(filename, startRow
    , endRow)
%IMPORTFILE Import numeric data from a text file as column vectors.
%   [ID,RL_P,RL_DB] = IMPORTFILE(FILENAME) Reads data from text file
%   FILENAME for the default selection.
%
%   [ID,RL_P,RL_DB] = IMPORTFILE(FILENAME, STARTROW, ENDROW) Reads data
%   from rows STARTROW through ENDROW of text file FILENAME.
%
% Example:
%   [ID,RL_p,RL_db] = importfile('true.rl',2, 35);
%
%    See also TEXTSCAN.

% Auto-generated by MATLAB on 2015/02/15 13:23:36

%% Initialize variables.
delimiter = ' ';
if nargin<=2
    startRow = 2;
    endRow = inf;
end

%% Format string for each line of text:
%   column1: double (%f)
%   column2: double (%f)
%   column3: double (%f)
% For more information, see the TEXTSCAN documentation.
formatSpec = '%f%f%f%[^\n\r]';

%% Open the text file.
fileID = fopen(filename,'r');

%% Read columns of data according to format string.
% This call is based on the structure of the file used to generate this
% code. If an error occurs for a different file, try regenerating the code
% from the Import Tool.
dataArray = textscan(fileID, formatSpec, endRow(1)-startRow(1)+1, 'Delimiter',
    delimiter, 'MultipleDelimsAsOne', true, 'HeaderLines', startRow(1)-1, '
    ReturnOnError', false);
```

```
for block=2:length(startRow)
    frewind(fileID);
    dataArrayBlock = textscan(fileID, formatSpec, endRow(block)-startRow(block)
        +1, 'Delimiter', delimiter, 'MultipleDelimsAsOne', true, 'HeaderLines',
         startRow(block)-1, 'ReturnOnError', false);
    for col=1:length(dataArray)
        dataArray{col} = [dataArray{col};dataArrayBlock{col}];
    end
end

%% Close the text file.
fclose(fileID);

%% Post processing for unimportable data.
% No unimportable data rules were applied during the import, so no post
% processing code is included. To generate code which works for
% unimportable data, select unimportable cells in a file and regenerate the
% script.

%% Allocate imported array to column variable names
true_rl_id = dataArray{:, 1};
true_rl_p = dataArray{:, 2};
true_rl_db = dataArray{:, 3};
```

Listing 6: Function to plot the results of an inversion: Misfit and likelihood over the iterations and maps of the likely source pressure grids

```
function plot_posterior_source_grid(image_id,inv_file,sim_source_file,latlim,
    lonlim,imagefolder,percentile_better,n_contour)

% function to plot the results of an inversion
% by Sebastian Menze, 2015
%
% inputs:
%   ID to add to the filename under wich the images as stored, path to
%   inversion file, path to simulated source grid file, minimum and
%   maximum latitude to show in map, minimum and maximum longitude to show
%   in map, folder to store images in, likelihood percentile threshold for
%   averaging
%   the maximum of the posterior distribution, number of contourlines

% output:
%   plots the misfit and likelihood for each generated solution over each
%   interations to show hoe well the parameter estimation algorithm has
%   performed


if exist(imagefolder)==0
    mkdir(imagefolder)
end

%% read in locactions

delimiter = ' ';
    startRow = 2;
    endRow = inf;
```

```
formatSpec = '%f%f%f%f%[^\n\r]';
fileID = fopen(sim_source_file,'r');
dataArray = textscan(fileID, formatSpec, endRow(1)-startRow(1)+1, 'Delimiter',
    delimiter, 'MultipleDelimsAsOne', true, 'HeaderLines', startRow(1)-1, '
    ReturnOnError', false);
for block=2:length(startRow)
    frewind(fileID);
    dataArrayBlock = textscan(fileID, formatSpec, endRow(block)-startRow(block)
        +1, 'Delimiter', delimiter, 'MultipleDelimsAsOne', true, 'HeaderLines',
         startRow(block)-1, 'ReturnOnError', false);
    for col=1:length(dataArray)
        dataArray{col} = [dataArray{col};dataArrayBlock{col}];
    end
end
fclose(fileID);

sim_sources.id = dataArray{:, 1};
sim_sources.lat = dataArray{:, 2};
sim_sources.lon = dataArray{:, 3};
sim_sources.depth  = dataArray{:, 4};

%% read in inversion results
load(inv_file)

%% make plot that shows misfit and likelihood of solutions over time

%latlim=[65 80];
%lonlim=[-30 25];

 [l_best,ix_best]=max(performance_likelihood(end,:));

f1=figure(1)
clf
% set(gcf,'color','w','position',[ 243   175   560   420])
set(gcf,'color','w')

subplot(211)
hold on
 set(gca,'yscale','log')
 for i_solution=1:size(performance_likelihood,2)
  plot( performance_iteration, performance_likelihood(:,i_solution) ,'-k')
 end
  p1=plot( performance_iteration, performance_likelihood(:,1) ,'-r')
    p2=plot( performance_iteration, performance_likelihood(:,ix_best) ,'-g')
   p3= plot( performance_iteration, performance_likelihood(:,end) ,'-b')
 ylabel('L(m)')
 xlabel('Iterations')
  title('Likelihood')
 grid on
 box on
 legend([p1,p2,p3],['p min: ' num2str(p_sim_whale(1),'%10.0e')],['p best: '
     num2str(p_sim_whale(ix_best),'%10.0e')], ['p max: ' num2str(p_sim_whale
     (end),'%10.0e')] ,'location','southeast')


subplot(212)
hold on
 set(gca,'yscale','log')
```

```
 for i_solution=1:size(performance_sse,2)
 %plot( performance_iteration,performance_sse(:,i_solution),'-k')
  plot( performance_iteration, performance_sse(:,i_solution) ,'-k')
 end
  plot( performance_iteration, performance_sse(:,1) ,'-r')
      p2=plot( performance_iteration, performance_sse(:,ix_best) ,'-g')
    plot( performance_iteration, performance_sse(:,end) ,'-b')
 ylabel('SSE in dB re 1 \mu Pa')
 xlabel('Iterations')
 title('Misfit')
 grid on
 box on
drawnow

  set(f1,'PaperPositionMode','auto')
  print(f1,'-dpng',[imagefolder,'/performance_',image_id,'.png'],'-r300')
%% show median and maxium of source pressure grid posterior distribution

sl_median=median(solutions_p);
sl_iqr=iqr(solutions_p);

ix_certain_all=sl_median>=sl_iqr;
sum(ix_certain_all)

recgrid_lat_vec=linspace(latlim(1),latlim(2),500);
recgrid_lon_vec=linspace(lonlim(1),lonlim(2),500);
[recgrid_lat,recgrid_lon] = meshgrid(recgrid_lat_vec,recgrid_lon_vec);

%%%

F = scatteredInterpolant(sim_sources.lat, sim_sources.lon,sl_median','natural',
    'none') ;
recgrid_median_p=F(recgrid_lat,recgrid_lon);
clear F

F = scatteredInterpolant(sim_sources.lat, sim_sources.lon,sl_iqr','natural','
    none') ;
recgrid_iqr_p=F(recgrid_lat,recgrid_lon);
clear F

f2=figure(2)
clf
% set(gcf,'color','w','position',[692    49   667   636])
set(gcf,'color','w')

subplot(121)
hold on
worldmap(latlim,lonlim)
% setm(gca,'MLabelLocation',10)
setm(gca,'MLabelLocation',20)

contourfm(recgrid_lat,recgrid_lon,recgrid_median_p,n_contour,  'LineStyle', '
    none');

 cb=contourcbar
 ylabel(cb,'Pressure in \mu Pa')
 colormap('gray')
 colormap(flipud(colormap))
```

```
 geoshow('landareas.shp', 'FaceColor', 'w', ...
   'EdgeColor', 'black');
 title({'Source pressure:','Median of \sigma(m)'})
 reddots= plotm(sim_sources.lat(ix_certain_all),sim_sources.lon(ix_certain_all)
     ,'.r')
legend(reddots,sprintf( '%s\n%s', 'Grid nodes with', 'low uncertainty' ),'
    location','best')

%%%%%%%%%%%%%
%likelihood boxplot
%boxplotaxes = axes('Position', [0.1784    0.7547    0.0435    0.1840]);
%boxplot(performance_likelihood(end,:),'plotstyle','compact','colors','k','
    labels',' ')
%set(boxplotaxes,'ylim',[0 1])
%title(boxplotaxes,'\sigma(m)')
%grid on
%get(legend,'position')
%%%%%%%%%%%%%


 perc_75=prctile( performance_likelihood(end,:) ,percentile_better );
 ix_best= performance_likelihood(end,:) > perc_75;

  sl_best_median_p=median(solutions_p(ix_best,:));
  sl_best_iqr_p=iqr(solutions_p(ix_best,:));

ix_certain_best=sl_median>=sl_iqr;

%%%
F = scatteredInterpolant(sim_sources.lat(ix_certain_best), sim_sources.lon(
    ix_certain_best),sl_best_median_p(ix_certain_best)','natural','none') ;
recgrid_best_certain=F(recgrid_lat,recgrid_lon);
clear F


%  subplot(212)
 subplot(122)

hold on
worldmap(latlim,lonlim)
contourfm(recgrid_lat,recgrid_lon,recgrid_best_certain,n_contour,  'LineStyle',
     'none');

 cb=contourcbar
 ylabel(cb,'Pressure in \mu Pa')
 colormap('gray')
 colormap(flipud(colormap))
 geoshow('landareas.shp', 'FaceColor', 'w', ...
   'EdgeColor', 'black');
 title({'Source pressure:','Approximated maximum of \sigma(m)'})
  plotm(sim_sources.lat(ix_certain_best),sim_sources.lon(ix_certain_best),'.r')
% setm(gca,'MLabelLocation',10)
setm(gca,'MLabelLocation',20)


  set(f2,'PaperPositionMode','auto')
  print(f2,'-dpng',[imagefolder,'/source_pressure_grid_',image_id,'.png'],'-
      r300')
```

```
end
```

Listing 7: Function to generate a geodesic grid in the North Atlantic

```
function  [sim_sources]=geodetic_grid_north_atlantic(resolution,latlim,lonlim)

% generate geodetic grid of source locations and cut of sources at land and
% above lat and lon limits
% by Sebastian Menze

% example
% [sim_sources]=generate_geodetic_grid_location(60000,[65 80],[-30 30])

[sim_sources.lat,sim_sources.lon] = GridSphere(resolution) ;

% delete grid points ouside study area
ix_inside=sim_sources.lat>latlim(1) & sim_sources.lat<latlim(2) & sim_sources.
    lon>lonlim(1) & sim_sources.lon<lonlim(2) ;
sim_sources.lat(~ix_inside)=[];
sim_sources.lon(~ix_inside)=[];

% delete grid points on land
[coast]=load('coast');
[Z, R] = vec2mtx(coast.lat, coast.long, ...
    5, [-90 90], [-90 270], 'filled');

val = ltln2val(Z, R, sim_sources.lat,sim_sources.lon);
isOcean = val == 2;

sim_sources.lat(~isOcean)=[];
sim_sources.lon(~isOcean)=[];

% delete estuaries
north_atlantic=[,...
72.81607371,    -31.9921875;...
83.44032649,    -31.6406250;...
80.23850054,    21.09375000;...
78.63000556,    49.21875000;...
70.25945200,    51.32812500;...
68.52823492,    37.61718750;...
69.03714171,    22.50000000;...
61.10078883,    9.140625000;...
58.81374171,    1.757812500;...
57.70414723,    -7.03125000;...
51.83577752,    -10.8984375;...
48.45835188,    -3.51562500;...
43.58039085,    1.054687500;...
38.54816542,    -7.73437499;...
32.54681317,    -7.73437499;...
23.24134610,    -5.62500000;...
7.362466865,    18.28125000;...
-20.6327842,    25.66406250;...
-20.6327842,    -52.3828125;...
```

```
9.102096738, -68.2031250;...
18.97902595,    -73.8281250;...
31.95216223,    -82.6171875;...
45.82879925,    -68.5546875;...
45.08903556,    -60.1171875;...
48.22467264,    -58.3593749;...
47.75409797,    -54.1406250;...
52.26815737,    -56.2500000;...
58.63121664,    -66.0937500;...
62.10388252,    -66.0937500;...
65.65827451,    -64.3359375;...
66.51326044,    -52.7343750;...
71.07405646,    -34.8046874];
in = inpolygon(sim_sources.lat,sim_sources.lon,north_atlantic(:,1),
    north_atlantic(:,2)) ;
sim_sources.lat(~in)=[];
sim_sources.lon(~in)=[];

%
% figure(1)
% clf
% set(gcf,'color','w')
% hold on
% worldmap('world')
% [coast]=load('coast');
% plotm(coast.lat,coast.long,'-k')
% plotm(sim_sources.lat,sim_sources.lon,'ok')

sim_sources.id=1:numel(sim_sources.lat);
sim_sources.id=sim_sources.id';

end
```

Listing 8: Function to calculate the transmission loss matrix using cyclindrical spreading

```
function tl_matrix_cylindrical_spreading(sim_source_location,recorder_location,
    target_filename,f_khz,waterdepth)

% function to calculate TL matrix using the cylindrical spreading law
% by Sebastian Menze, 2015
%
% input:
% path to simulated source grid file, path to recorder location
% file, file name under wich TL matrix will be stored, frequency in kHz,
% range until spherical spreading is assumed (average water depth)
%
% output:
% TL matrix in dB re 1 upa as .mat file
%
% example:
% tl_cylindrical_spreading('sim_source_location_files/sim_sources_geodesic_195.
    loc','recorder_location_files/recorders_geodesic_47.loc','ss195_r47.mat
    ',0.2,100)

% waterdepth=4000
% f=0.2;
absorption_factor = sound_abs(2,35,10,f_khz,7.5);
```

```
% absorption_factor=10^-3
% db_uncertainty=2

% read source positions
% sim_source_location='sim_sources.loc';
[sim_source_id,sim_source_lat,sim_source_lon] = import_loc_file(
    sim_source_location) ;

% read recorder positions
% recorder_location='recorders.loc';
[recorders_id,recorders_lat,recorders_lon] = import_loc_file(recorder_location)
     ;


for i_source=1:numel(sim_source_lat)

for i_receiver=1:numel(recorders_lat)

distance_in_km(i_source,i_receiver)=deg2km(distance(sim_source_lat(i_source),
    sim_source_lon(i_source),recorders_lat(i_receiver),recorders_lon(i_receiver
    ))) ;

if distance_in_km(i_source,i_receiver) > 0

    if distance_in_km(i_source,i_receiver)*1000 < waterdepth

   % spherical loss until water depth
TL_spreading=20*log10( distance_in_km(i_source,i_receiver) *1000 ) ;
tl_db(i_source,i_receiver)= absorption_factor * distance_in_km(i_source,
    i_receiver) + TL_spreading ;

    else
  % spherical nd cylindrical loss u
TL_spreading= 20*log10(waterdepth) +  10*log10( distance_in_km(i_source,
    i_receiver)*1000 /waterdepth  ) ;
tl_db(i_source,i_receiver)= absorption_factor * distance_in_km(i_source,
    i_receiver) + TL_spreading ;

    end

else
 tl_db(i_source,i_receiver)= 0;

end
clear TL_spreading

end
end
tl_db=-tl_db;
save(target_filename,'tl_db')
```

Listing 9: Function to calculate the transmission loss in 360 degree slices around the source locations using the raytracing model BELLHOP

```
function tl_bellhop_slices(source_file,etopo_location,ssp_file,bellhop_location
    ,scenario_name,frequency,latlim,lonlim,rec_depth)
```

```
% function to model the transmission loss using the raytracing model
% BELLHOP, it generates slices covering 360 degrees around each source
% until the longitude and latitude limits are reached
% by Sebastian Menze

% example:
% tl_bellhop_slices('sim_source_location_files/sim_sources_geodesic_195.loc','
    tl_model/etopo1_ice_c_i2/etopo1_ice_c_i2.bin','tl_model/
    woa_annual_mean_global_ssp.mat','tl_model/BELLHOP_UNIX/bin/bellhop.exe','
    scenario_1',20,[65 80],[-30 25],100)

% scenario_name='ss195'
% rec_depth=100;
%% calculate TL slices

 S = referenceSphere('earth');
% latlim=[65 80];
% lonlim=[-30 25];
% addpath('BELLHOP_UNIX/Matlab/ReadWrite')
% frequency=20

% load source file
% source_file='source_distribution_files/gaussian_source_distribution_100.sl'
if strcmp(source_file(end-2:end),'.sl')
[source_ID,source_lat,source_lon,source_depth,source_sl_db] = import_sl_file(
    source_file);
n_sources=source_ID(end);
else
    % source_file='sim_source_location_files/sim_sources_geodesic_195.loc'
[source_ID,source_lat,source_lon,source_depth] = import_loc_file(source_file);
n_sources=source_ID(end);
end

% read World Ocean Atlas
% ssp_file='tl_model/woa_annual_mean_global_ssp.mat';
load(ssp_file);

if exist(scenario_name,'dir')==0
  mkdir(scenario_name)
end

for i_source=1:n_sources



    write_folder=[scenario_name,'/raytracing_source_',num2str(i_source)];


    % check if raytrace has been done previously
    if  exist([scenario_name,'/slices_source_',num2str(i_source),'.mat'])==0

    % find maximum range
   dist=distance(source_lat(i_source),source_lon(i_source),latlim(1),lonlim(1))
       ;
   dist_source_rec_km(1)=deg2km(dist);
   clear dist
   dist=distance(source_lat(i_source),source_lon(i_source),latlim(1),lonlim(2))
```

```
      ;
   dist_source_rec_km(2)=deg2km(dist);
   clear dist
   dist=distance(source_lat(i_source),source_lon(i_source),latlim(2),lonlim(1))
      ;
   dist_source_rec_km(3)=deg2km(dist);
   clear dist
   dist=distance(source_lat(i_source),source_lon(i_source),latlim(2),lonlim(2))
      ;
   dist_source_rec_km(4)=deg2km(dist);
   clear dist

[max_dist,ix_max_dist]=max(dist_source_rec_km);

    % generate env files for 360deg slices
    angle_vector=0:5:360;
    for i_angle=1:numel(angle_vector)
    [circle_lat(i_angle),circle_lon(i_angle)] = reckon(source_lat(i_source),
        source_lon(i_source),km2deg(max_dist+100),angle_vector(i_angle))    ;
    end

% read ETOPO
% etopo_location='etopo1_ice_c_i2/etopo1_ice_c_i2.bin'
[Z_etopo, R_etopo] = etopo(etopo_location,1, [min(circle_lat),max(circle_lat)],
     [min(circle_lon),max(circle_lon)]);
 Z_etopo(Z_etopo>0)=0;


%%
for i_angle=1:numel(angle_vector)
s_lat=source_lat(i_source);
s_lon=source_lon(i_source);
r_lat=circle_lat(i_angle);
r_lon=circle_lon(i_angle);

%%%%% write bty file

clear zi ri profile_lat profile_lon
[zi,ri,~,~] = mapprofile(Z_etopo,R_etopo,[s_lat,r_lat],[s_lon,r_lon],'km');
is_nana=isnan(zi);
ri(is_nana)=[];
zi(is_nana)=[];
clear is_nana

bty_name=['slice_',num2str(i_angle),'.bty'];

if exist(write_folder,'dir')
else
    system(['mkdir ' write_folder]);
end

% Open file for writing
file_identifier = fopen([write_folder,'/',bty_name], 'w');

fprintf(file_identifier,'''L''\n');
fprintf(file_identifier,'%d\n',numel(ri));
for i=1:numel(ri)
    fprintf(file_identifier,'%6.1f %6.1f\n',ri(i),abs(zi(i)));
```

```
end
fclose(file_identifier);
clear file_identifier bty_name

deepest_point(i_angle)=abs(min(zi));

%%%%% write ssp file
clear ssp_section
for i_depth=1:numel(global_ssp_depth)
[ssp_section.ssp(i_depth,:),ssp_section.range,~,~] = mapprofile(global_ssp(
    i_depth,1).z,global_ssp(i_depth,1).r,[s_lat,r_lat],[s_lon,r_lon],'km');
end



ssp_name=['slice_',num2str(i_angle),'.ssp'];

% Open file for wiriting
file_identifier = fopen([write_folder,'/',ssp_name], 'w');

fprintf(file_identifier,'%d\n',numel(ssp_section.range));
  row_string=[repmat('%6.2f ',1,numel(ssp_section.range)),'\n'];
    fprintf(file_identifier,row_string,ssp_section.range);
for i_depth=1:numel(global_ssp_depth)
     fprintf(file_identifier,row_string,ssp_section.ssp(i_depth,:));
   ssp_depth(i_angle,i_depth)=global_ssp_depth(i_depth);
   ssp_env(i_angle,i_depth)=ssp_section.ssp(i_depth,1)  ;
end
fclose(file_identifier);
clear file_identifier ssp_name

end

clear Z_etopo R_etopo
% replace woa end depth with deepest point
ix_bty_below_ssp=ssp_depth(:,end)<deepest_point';
ssp_depth(ix_bty_below_ssp,end)=deepest_point(ix_bty_below_ssp);
clear deepest_point

%% run bellhop for 360deg slices

 parfor i_angle=1:numel(angle_vector)

s_lat=source_lat(i_source);
s_lon=source_lon(i_source);
r_lat=circle_lat(i_angle);
r_lon=circle_lon(i_angle);

env_file=[write_folder,'/slice_',num2str(i_angle),'.env']
   disp(['run BELLHOP for: ' env_file])

% Open file for writing
% frequency=20
file_identifier = fopen(env_file, 'w');

fprintf(file_identifier,'''%s''\n','Matlab generated env file'); % fclose(xfid)
fprintf(file_identifier,'%d ! FREQ(Hz)\n',frequency);
fprintf(file_identifier,'%d ! NMEDIA\n',1);
```

```
fprintf(file_identifier,'''%s'' \n','QVWT'); % for range dependent ssp
fprintf(file_identifier,'%d %6.1f %6.1f \n',[0,0,ssp_depth(i_angle,end)]);
for i_depth=1:numel(ssp_depth(i_angle,:))
fprintf(file_identifier,'%6.1f %6.1f /\n',[ssp_depth(i_angle,i_depth),ssp_env(
    i_angle,i_depth)]);
end
fprintf(file_identifier,'''A*'' 0.0\n');
fprintf(file_identifier,'%6.1f %6.1f %6.1f %6.1f %6.1f %6.1f\n',[ssp_depth(
    i_angle,end),1800.0,0.0,2.0,0.1,0.0]);
fprintf(file_identifier,'%d \n',1);
fprintf(file_identifier,'%6.1f /\n',source_depth(i_source)) ;
fprintf(file_identifier,'%d \n',1) ;
fprintf(file_identifier,'%6.1f /\n',rec_depth) ;
fprintf(file_identifier,'%d \n',500) ;
fprintf(file_identifier,'0 %6.1f /\n', deg2km(distance(s_lat,s_lon,r_lat,r_lon)
    ) ) ;
fprintf(file_identifier,'''IB''\n');
fprintf(file_identifier,'%d 0 \n',1000); % n rays choose by beelhop
fprintf(file_identifier,'%d %d /\n',[-45,45]); % angle
fprintf(file_identifier,'0.0 %6.1f %6.1f \n',[ssp_depth(i_angle,end), deg2km(
    distance(s_lat,s_lon,r_lat,r_lon))]);
fprintf(file_identifier,' \n');

fclose(file_identifier);

% RUN BELLHOP RAYTRACING MODEL
system([ bellhop_location,' ',env_file(1:end-4)]);

 % get lat and lon of each of the 500 slice points
[slice_lat(i_angle,:),slice_lon(i_angle,:)] = track2(s_lat,s_lon,r_lat,r_lon,S,
    'degrees',500);

[ PlotTitle, ~, freq, ~, Pos, pressure ] = read_shd( [env_file(1:end-4),'.shd']
     );
slice_pressure(i_angle,:)=squeeze(pressure);

 end
  save([scenario_name,'/slices_source_',num2str(i_source),'.mat'],'slice_lat','
      slice_lon','slice_pressure')
    else

    end
   clear slice_lat slice_lon slice_pressure slice_tl_db circle_lat circle_lon
end

end
```

Listing 10: Function to calculate the transmission loss matrix from the slices generated by the raytracing model BELLHOP

```
function raytracing_slices_2_tl_matrix(source_file,scenario_name,
    recorder_folder,latlim,lonlim)

% function to interpolate from the raytracing slices generated by the
% BELLHOP model to a TL matrix connecting each source and receiver
% by Sebastian Menze, 2015
%
```

```
% example:
% slices2tlmatrix('sim_source_location_files/sim_sources_geodesic_195.loc','
    scenario_1','recorder_location_files',[65 80],[-30 25])

% load source file
% source_file='source_distribution_files/gaussian_source_distribution_100.sl'
if strcmp(source_file(end-2:end),'.sl')
[source_ID,source_lat,source_lon,source_depth,source_sl_db] = import_sl_file(
    source_file);
n_sources=source_ID(end);
else
    % source_file='sim_source_location_files/sim_sources_geodesic_195.loc'
[source_ID,source_lat,source_lon,source_depth] = import_loc_file(source_file);
n_sources=source_ID(end);
end

% loop through recorder files
% recorder_folder='recorder_location_files'
rec_ls=dir([recorder_folder,'/*.loc']);

%% interpolate TL for all receiver files in folder

for i_source=1:n_sources

  load([scenario_name,'/slices_source_',num2str(i_source),'.mat'],'slice_lat','
      slice_lon','slice_pressure')

  % interpolate

recgrid_lat_vec=linspace(latlim(1),latlim(2),500);
recgrid_lon_vec=linspace(lonlim(1),lonlim(2),500);
[recgrid_lat,recgrid_lon] = meshgrid(recgrid_lat_vec,recgrid_lon_vec);

ix_valid=(slice_pressure(:)~=0);

F = scatteredInterpolant(slice_lat(ix_valid),slice_lon(ix_valid),slice_pressure
    (ix_valid),'natural','nearest') ;
recgrid_tl_p=F(recgrid_lat,recgrid_lon);
recgrid_tl_db=real(20*log10(recgrid_tl_p));
recgrid_tl_db(recgrid_tl_db==-Inf)=NaN;
save([scenario_name,'/recgrid_source_',num2str(i_source),'.mat'],'recgrid_lat',
    'recgrid_lon','recgrid_tl_p','recgrid_tl_db');


for i_recorder_file=1:size(rec_ls,1)
 % load receiver file
 recorder_file=[recorder_folder,'/',rec_ls(i_recorder_file).name] ;
[recorder_ID,recorder_lat,recorder_lon,recorder_depth] = import_loc_file(
    recorder_file);

% interpolate
recorders_tl_p=F(recorder_lat,recorder_lon);
recorders_tl_db=real(20*log10(recorders_tl_p));

 recorder_string=rec_ls(i_recorder_file).name(1:end-4);

eval(['tl_p_' ,recorder_string,'(i_source,:)=recorders_tl_p;'])
eval(['tl_db_' ,recorder_string,'(i_source,:)=recorders_tl_db;'])
```

```
end

clear F

% optinal figure:

%   figure(1)
% clf
% set(gcf,'color','w')
% scrsz = get(0,'ScreenSize');
% set(gcf,'Position',[scrsz(1) scrsz(2) scrsz(3) scrsz(4)])
%
% subplot(121)
%  hold on
%  scatter(slice_lon(:),slice_lat(:),10,slice_tl_db(:),'fill')
%  [coast]=load('coast');
% plot(coast.long,coast.lat,'-k')
% plot(recorder_lon,recorder_lat,'ok')
%   colorbar
%  colormap('jet')
%  set(gca,'clim',[-150 -80],'ylim',latlim,'xlim',lonlim)
%  title(['Source ',num2str(i_source)])
%
% subplot(222)
% hold on
% worldmap(latlim,lonlim)
% [coast]=load('coast');
% plotm(coast.lat,coast.long,'-k')
% geoshow(recgrid_lat,recgrid_lon,recgrid_tl_db,'DisplayType','surface')
%  colorbar
%  colormap('jet')
% set(gca,'clim',[-150 -80])
%
% subplot(224)
% hold on
% worldmap(latlim,lonlim)
% [coast]=load('coast');
% plotm(coast.lat,coast.long,'-k')
% plot_value=recorders_tl_db;
% plot_bins=100;
%   plot_range=[-150 -80];
%   set(gca,'clim',[-150 -80])
% colormap('jet')
% jet_cmap=jet(plot_bins);
% [~,ind] = histc(plot_value,linspace(plot_range(1),plot_range(2),plot_bins));
% ind(ind==0)=1;
% for i_point=1:numel(plot_value)
%   plot_cmap=jet_cmap(ind(i_point),:);
% plotm(recorder_lat(i_point), recorder_lon(i_point),'marker','o','markersize
    ',6,'MarkerFaceColor',plot_cmap,'color',plot_cmap,'linestyle','none');
% end
% colorbar
%
%  set(gcf,'PaperPositionMode','auto')
%  print(gcf,'-dpng',['Raytracing_transmission_loss_source_ ',num2str(i_source)
    ,'.png'],'-r300')
```

```
end

for i_recorder_file=1:size(rec_ls,1)

recorder_string=rec_ls(i_recorder_file).name(1:end-4);

 % save tl matrix
save([scenario_name,'/tl_bellhop_',recorder_string,'.mat'],['tl_p_' ,
    recorder_string],['tl_db_' ,recorder_string])

end


end
```

Listing 11: Example script demonstrating the inversion method based on published fin index measurements.

```
%% inversion of published fin index values
%
% fin whale chorus received level dataset averaged as composite dataset
% from Nieukirk et al 2012 and Nierkirk and Klink 2012
%
% averged fin index take s as chorus signal to noise ratio,
% values taken from the 1. of January
%
% by Sebastian Menze, 2015

%% generate composite fin whale chorus received level dataset

base=90;

% from nieurkirk et al. 2012

fin_rl.lat(1)=50;
fin_rl.lon(1)=-34;
fin_rl.db(1)=base+10;

fin_rl.lat(2)=50;
fin_rl.lon(2)=-24;
fin_rl.db(2)=base+9;

fin_rl.lat(3)=42;
fin_rl.lon(3)=-34;
fin_rl.db(3)=base+9.5;

fin_rl.lat(4)=42;
fin_rl.lon(4)=-26;
fin_rl.db(4)=base+5;

fin_rl.lat(5)=39;
fin_rl.lon(5)=-34;
fin_rl.db(5)=base+7;

fin_rl.lat(6)=37;
fin_rl.lon(6)=-29;
fin_rl.db(6)=base+6;
```

```
ix=7;
fin_rl.lat(ix)=32;
fin_rl.lon(ix)=-43;
fin_rl.db(ix)=base+5;

ix=8;
fin_rl.lat(ix)=32;
fin_rl.lon(ix)=-35;
fin_rl.db(ix)=base+4;

ix=9;
fin_rl.lat(ix)=26;
fin_rl.lon(ix)=-50;
fin_rl.db(ix)=base+4;

ix=10;
fin_rl.lat(ix)=26;
fin_rl.lon(ix)=-40;
fin_rl.db(ix)=base+3;

ix=11;
fin_rl.lat(ix)=16;
fin_rl.lon(ix)=-49;
fin_rl.db(ix)=base+2;

ix=12;
fin_rl.lat(ix)=16;
fin_rl.lon(ix)=-43;
fin_rl.db(ix)=base+2;

% from klinck and nieurkirk 2012

fin_rl.lat(13)=78+(50/60);
fin_rl.lon(13)=05+(29/60);
fin_rl.db(13)=base+1.5;

fin_rl.lat(14)=74+(56/60);
fin_rl.lon(14)=-04+(37/60);
fin_rl.db(14)=base+2;


%% generate sim_source distribution scenarios

% geodesic distribution
addpath('GridSphere')
folder=['inversion_from_literature_6'];
mkdir(folder)

latlim=[10 85];
lonlim=[-80 20];

source_depth=10;

 resolution_factor=4
resolution= 2 + ( 10 * (4 ^ resolution_factor) )

[sim_sources]=geodetic_grid_north_atlantic(resolution,latlim,lonlim);
```

```
n_sim_source=sim_sources.id(end)


% write simulated sources file
fid=fopen([folder,'/sim_sources.loc'],'w');
fprintf(fid,'ID latitude longitude depth\n');
for i_element=1:numel(sim_sources.id)
fprintf(fid,'%d %f %f %d\n',[sim_sources.id(i_element),sim_sources.lat(
    i_element),sim_sources.lon(i_element),source_depth]);
end
fclose(fid);

%% prepare RL data

fin_rl.p=10.^(fin_rl.db/20)
fin_rl.id=1:numel(fin_rl.p)

  figure(1)
clf
set(gcf,'color','w')
hold on
worldmap(latlim,lonlim)
[coast]=load('coast');
plotm(coast.lat,coast.long,'-k')
plotm(sim_sources.lat,sim_sources.lon,'ok')

plot_value= fin_rl.db;
plot_bins=100;

plot_range=[min(plot_value),max(plot_value)];

jet_cmap=jet(plot_bins);
[~,ind] = histc(plot_value,linspace(plot_range(1),plot_range(2),plot_bins));
ind(ind==0)=plot_bins;
for i_point=1:numel(plot_value)
  plot_cmap=jet_cmap(ind(i_point),:);
plotm(fin_rl.lat(i_point), fin_rl.lon(i_point),'marker','o','markersize',10,'
    MarkerFaceColor',plot_cmap,'color',plot_cmap,'linestyle','none')
end
set(gca,'clim',[plot_range(1),plot_range(2)])
cb=colorbar;
ylabel(cb,'RL in dB re 1 \muPa')
colormap('jet')
drawnow


  set(gcf,'PaperPositionMode','auto')
  print(gcf,'-dpng',[folder,'/input_data.png'],'-r300')


%% write recover location and received level file

rec_depth=4000;
n_recorder=6;

% write recorder and rl file
fid=fopen([folder,'/recorders.loc'],'w');
fprintf(fid,'ID latitude longitude depth\n');
```

```
for i_element=1:numel(fin_rl.id)
fprintf(fid,'%d %f %f %d\n',[fin_rl.id(i_element),fin_rl.lat(i_element),fin_rl.
    lon(i_element),rec_depth]);
end
fclose(fid);

% write true reveived level file
fid=fopen([folder,'/recorders.rl'],'w');
fprintf(fid,'ID RL_p RL_db\n');
for i_element=1:numel(fin_rl.id)
fprintf(fid,'%d %f %f\n',[fin_rl.id(i_element),fin_rl.p(i_element),fin_rl.db(
    i_element)]);
end
fclose(fid);

 %% calculate tl matrix with cylindrical spreading

tl_matrix_cylindrical_spreading([folder,'/sim_sources.loc'],[folder,'/recorders
    .loc'],[folder,'/tl_cylindrical.mat'],0.02,4000)

 %% run inversion

load([folder,'/tl_cylindrical.mat'])

%%% estimate sum of energy from all calling fin whales

n_males_max = 40000 /2;

fin_sl_mean_db=189;
fin_sl_mean_p=10^(fin_sl_mean_db/20);

inter_call_interval= 12;
call_duration=1;

call_rate= call_duration/(call_duration+inter_call_interval);

p_min= 1 * fin_sl_mean_p  *call_rate
p_max= n_males_max * fin_sl_mean_p*  call_rate

sa_parameter_estimation(5000,50,4,p_min,p_max,[folder,'/sim_sources.loc'],[
    folder,'/recorders.loc'],[folder,'/recorders.rl'],tl_db,6,[folder,'/
    inversion.mat'])

plot_posterior_source_grid(['inv_result'],[folder,'/inversion.mat'],[folder,'/
    sim_sources.loc'],latlim,lonlim,folder,90,50)
```